Micromechanical modeling of ferroelectric thin films and bulk ceramics in a multi-scale approach

Vorgelegt von

Olena Anand geb. Vedmedenko

aus Lugansk (Ukraine)

Contents

Zusammenfassung

Raffiniertes Design von piezoelektrischen und insbesondere ferroelektrischen keramischen Werkstoffen eröffnet hoch effiziente Möglichkeiten, elektrische Energie in mechanische Bewegung zu konvertieren, und umgekehrt, die Verformung in elektrisches Signal umzuwandeln. Prominente Vertreter der Ferroelektrika sind Bariumtitanat $BaTiO_3$ (BTO), Bleititanat $PbTiO_3$ (PTO) und Bleizirkonattitanat $PbZr_xTi_{1-x}O_3$ (PZT). In Einspritzventilen von Dieselmotoren, hochauflösenden Rastertunnelmikroskopen oder in Stellungsreglern für pneumatische Antriebe agieren keramische Bauteile als Aktuatoren. In diesen Anwendungen formen sie elektrische Spannung in präzise Verfahrwege im Mikrometer- bzw. Nanometerbereich um. In Applikationen zur Energierückgewinnung sowie in Drucksensoren wandeln piezokeramischen Werkstoffe Kräfte bzw. Verformungen in elektrische Spannung bzw. Ladung um. In den oben genannten Anwendungen werden überwiegend polykristalline Bulkkeramiken verwendet. Eine neue Klasse von keramischen Bauteilen mit wenigen hundert Nanometern Dicke, die sogenannten ferroelektrischen Dünnschichten, wurde in den letzten Jahrzehnten entwickelt. Diese Systeme fungieren als Mikroaktoren, nichtflüchtige Speichermedien (Ferroelectric Random Access Memory) oder Sensoren für Biomoleküle im medizinischen Bereich. Allgemein eröffnen ferroelektrische Dünnschichten vielfältige Möglichkeiten der Bauteilminiaturisierung und -integration, zuallererst auf Basis der Siliziumtechnologie.

Die Vorteile von piezoelektrischen Aktoren und Messumformern liegen in der hohen dielektrischen Permittivität, hohen piezoelektrischen und pyroelektrischen Kopplungskoeffizienten, kurzen Ansprechzeiten sowie in geringen Energieverlusten. Ein weiterer Vorteil besteht in den geringen Bauteilgrößen verglichen mit elektrostatischen, elektromagnetischen oder elektrothermischen Alternativen. Zu den Nachteilen zählen hohe Entwicklungs- und Fertigungskosten. Diese hängen mit komplexen Struktur-Eigenschaftsbeziehungen der Ferroelektrika, die noch nicht vollständig erforscht und verstanden sind, zusammen. Die physikalischen Parameter von polykristallinen Keramiken und ferroelektrischen Dünnschichten variieren stark mit der stöchiometrischen Zusammensetzung und hängen in erheblichem Maß von der Anisotropie und den extrinsischen Beiträgen aufgrund von Domänenwandbewegungen ab. Darüber hinaus führt die Abscheidung der keramischen Dünnschichten auf einem Substrat zu Eigenschaften, die sich signifikant von denen der Bulkkeramiken unterscheiden. Eine systematische und skalenübergreifende physikalische Modellierung und numerische Simulation könnte sich als kostengünstige

und effektive Methode zur Untersuchung und Optimierung der komplexen Eigenschaften von ferroelektrischen Keramiken erweisen.

Die mikromechanische Modellierung zählt zu den meist verbreiteten theoretischen Methoden zur Untersuchung der makroskopischen Materialeigenschaften in Abhängigkeit von der heterogenen Mikrostruktur [Böhm 1998]. Die Mehrzahl der bisher publizierten mikromechanischen Modelle beschäftigt sich mit der Berechnung von linearen piezoelektrischen, dielektrischen und elastischen Materialkonstanten in Abhängigkeit vom Polungsgrad der Keramik [Pertsev 1998], [Fröhlich 2001], [Jayachandran 2009]. Die verwendeten Methoden sind allerdings zumeist nicht in der Lage, die Konfiguration der mikroskopischen Polarisationen und daraus den remanenten Zustand und die wesentlich davon abhängigen effektiven Materialkonstanten vorherzusagen. Die genannten Parameter sind aber essentiell für das Design aktorischer und sensorischer Komponenten. Die Konfiguration der mikroskopischen Polarisationen, kurz die Domänenkonfiguration des Polykristalls wird durch die Lasthistorie erheblich beeinflusst. Vordergründig wird also nach Modellierungsansätzen gesucht, die die Reaktion der Domänenkonfiguration auf beliebige Laständerung in geeigneter und effektiver Weise beschreibt.

Eine Vorschrift zur Polarisationsumorientierung in einem ferroelektrischen Polykristall, der einer elektrischen und/oder einer mechanischen Last ausgesetzt ist, bietet das Modell von Huber und Fleck [Huber 1999], [Huber 2001]. Das konstitutive Gesetz wurde mit Hilfe der Finite-Elemente(FE)-Methode in 2D [Kamlah 2005] und in 3D [Pathak 2008] implementiert. Dabei wurden allerdings nur qualitative Untersuchungen von hypothetischen Bulkferroelektrika durchgeführt. Nichtlineare Eigenschaften von realen Keramiken und Dünnschichten wurden nicht diskutiert. Darüber hinaus wurden einzelne Körner des Polykristalls durch reguläre (kubische) finite Elemente beschrieben, was von der Realität bedeutend abweicht. In der vorliegenden Arbeit wird eine 3D-Implementierung des Huber-Fleck-Modells zur Berechnung der ferroelektrischen Eigenschaften von realen Dünnschichten und Bulkkeramiken verwendet. Neben idealisierten (kubischen) Körnern kommen zum ersten Mal realitätsnahe polyederförmige Körner mit 5 bis 40 Elementen pro Korn zum Einsatz.

Polyederförmige Strukturen werden typischerweise mit stochastischen Methoden der Raumzerlegung, wie etwa Voronoi- oder Laguerre-Mosaiken, erzeugt. Frühere Untersuchungen [Fröhlich 2001] haben gezeigt, dass die genannten Verfahren schon bei zweidimensionalen Modellen mit wenigen Dutzend Körnern zu Schwierigkeiten bei der anschließenden Vernetzung mit finiten

Elementen führen. In der vorliegenden Arbeit wird eine neue Methode vorgestellt, die zuverlässig vernetzbare Kornstrukturen mit bis zu tausend Einzelkörnern generiert. Ein weiterer Nachteil der Voronoi-Zerlegung betrifft die Verteilung der Kornvolumina. Laut Literatur erfüllt die Verteilung bei realen polykristallinen Keramiken und Metallen eine Lognormalfunktion [Nettleship 2002], [Fan 2004]. Die Voronoi-Zerlegung weist dagegen die Gammaverteilung auf. In der Arbeit werden existierende Verfahren zur Generierung realistischer Kornmodelle diskutiert, und es wird eine neue Methode vorgestellt, die dreidimensionale periodisch fortsetzbare Kornstrukturen mit einer vorgegebenen lognormalen Verteilung der Korngrößen und periodisch fortsetzbare Finite-Elemente-Netze realisiert. Diese Art von Vernetzung ermöglicht Simulationen mit periodischen Randbedingungen, die eine realistische Beschreibung von Materialien darstellen.

Entscheidende Inputparameter jedes mikromechanischen Modells sind die piezoelektrischen, dielektrischen und elastischen Materialkonstanten des Einkristalls, die die Eigenschaften der einzelnen Körner beschreiben. Üblicherweise werden in mikromechanischen Berechnungen experimentelle Einkristallkoeffizienten verwendet. Das Verfahren wird allerdings äußerst ineffektiv, wenn zur Untersuchung neuartiger Materialien im ersten Schritt entsprechende Einkristalle synthetisiert und experimentell charakterisiert werden müssen. Für einige keramische Werkstoffe, z.B. für PZT, konnten bislang keine Einkristalle hergestellt werden und die notwendigen Inputparameter sind nicht verfügbar. Eine vielversprechende Technik, die das beschriebene Problem umgehen lässt, heißt Multiskalenmodellierung. Nach dieser Methode werden die erforderlichen Inputkonstanten anhand von Modellen, die das Werkstoffverhalten auf anderen Längen- oder Zeitskalen beschreiben, ermittelt.

Im Projekt COMFEM[1], das einen Rahmen für die vorliegende Arbeit darstellt, werden i) Ab-initio-Dichtefunktionalsimulationen und Berechnungen mit dem Shell-Modell, die Ferroelektrika auf der Nanoskala der Elektronen und Atomen beschreiben, ii) Phasenfeldmodellierung, die auf der mesoskopischen Ebene der ferroelektrischen Domänen fungiert, sowie iii) mikromechanische Berechnungsmethoden, die die Heterogenität der Polykristallkörner auf der Mikroskala erfassen, in einer Simulationskette kombiniert. Die Multiskalenmodellierung wurde zu unserer Kenntnis bisher nicht für Bulkkeramiken und insbesondere Dünnschichten vorgenommen. Sie

---

erlaubt eine wissensbasierte Beschreibung der Materialeigenschaften, frei von experimentellen Inputparametern. Die mikromechanische Simulation der Ferroelektrika und die Verknüpfung mit Modellen auf den Meso- und Nanoskalen ist eines der zentralen Themen der vorliegenden Arbeit. Es werden systematische Untersuchungen von BTO, PTO und PZT Bulk- und Schichtsystemen mit mehreren multi- und einskaligen Methoden vorgestellt. Dabei wird die Vorhersagekraft der verschiedenen Modelle anhand der Vergleiche von berechneten Materialparametern mit experimentellen Werten diskutiert. Insbesondere Simulationen von Bleizirkonattitanat (PZT) sind in der Literatur recht selten, da die Einkristallkonstanten bisher nicht gemessen werden konnten. Weiterhin sind nach aktuellem Kenntnisstand bislang keine Untersuchungen des Einflusses von Materialklemmung durch das Substrat auf die ferroelektrischen Parameter publiziert worden.

Die mit dem Huber-Fleck-Modell für verschiedene Materialsysteme berechneten Kennwerte zeigen eine gute Übereinstimmung mit experimentellen Werten unter der Bedingung, dass die im Versuch ermittelten Einkristallkonstanten oder die im Zuge der Phasenfeldsimulationen ermittelten Domänenwandbeiträge kombiniert mit Einkristallkonstanten aus DFT und Shell-Modell verwendet werden. Darüber hinaus erlauben die errechneten Polarisationskonfigurationen im remanenten Zustand einige bisher nicht gut verstandene Eigenschaften der Ferroelektrika, wie beispielsweise den sehr niedrigen dielektrischen Koeffizienten von PTO-Keramik im Vergleich zu PTO-Dünnschicht und BTO-Keramik, zu erklären. Weiterhin ermöglicht simulierte remanente Polarisation Ermittlung von Materialkonstanten aus anderen theoretischen Publikationen, die keine konkreten Werte sondern lediglich deren Abhängigkeiten vom Polungsgrad angegeben haben, wie etwa [Pertsev 1998]. So ermittelte Werkstoffparameter zeigen ebenfalls eine gute Übereinstimmung mit den entsprechenden experimentellen Werten.

Es kann zusammengefasst werden, dass das Huber-Fleck-Modell sowie die vorgeschlagene Multiskalenmodellierung eine hohe Vorhersagekraft besitzen. Ihre Anwendung auf strukturell ähnliche Materialsysteme sollte zu ähnlich guten Ergebnissen führen und damit auch zur Entwicklung und Optimierung neuer keramischer Werkstoffe beitragen.

1 Introduction

Sophisticated design of piezoelectric and especially ferroelectric ceramics offers highly efficient ways to convert electrical energy into motion and inversely to transmit deformation into electrical signal. Prominent examples of ferroelectrica are barium titanate $BaTiO_3$ (BTO), lead titanate $PbTiO_3$ (PTO) and lead zirconate titanate $PbZr_xTi_{1-x}O_3$ (PZT). In facilities converting electrical energy into mechanical work a ferroelectric material operates as an actuator. Typical industrial examples of such applications are given by fuel injectors of high-performance common rail diesel engines, scanning tunneling microscopes of highest resolution or by positioners for pneumatic drives. Apart from the implementation as an actuator the piezoelectric materials are used in numerous sensoric applications, in which the mechanical deformation is converted into an electrical signal. This type of the energy transmission is realized in piezoelectric energy harvesters. In the active vibration damping systems bulk piezoelectric ceramics works in both regimes: as a sensor as well as an actuator. In the applications mentioned above the bulk polycrystalline ferroelectric ceramics is usually used. In the past decade, a new class of applications based on thin ceramic films of several hundred nanometers thickness has been developed [Hoffmann 2003]. Among the thin-film based devices are the microactuators as well as the non-volatile Ferroelectric Random Access Memory cells. Other areas of utilization of ferroelectric thin films are medical and biological devices for resonant detecting of single molecules. Generally, the piezoelectric thin films offer a way of device miniaturization and their integration into the silicon technology. They add functionality to integrated circuits and enable invention of new applications.

The advantages of using piezoelectric transducers are their high dielectric permittivity, high piezoelectric and pyroelectric coupling coefficients causing low energy losses and fast response. Another incontestable advantage of piezoelectric converters is smaller area consumption as compared to their electrostatic, electromagnetic or electrothermic analogues. The main drawbacks are the high costs for the device development and manufacturing caused by the complex physical properties of ferroelectrics, which are still not completely understood.

The physical properties of polycrystalline ceramics and ferroelectric thin films are strongly influenced by the stoichiometric constitution, anisotropy and extrinsic contributions from the domain wall displacements. These criteria are usually responsible for the frequency and field dependence of the material parameters. In addition, the setup of thin ceramic films on a substrate

9

often leads to very different, in comparison to bulk materials, properties, which must be taken into account when modeling devices. A promising experimental way to accelerate development of ferroelectric devices and to screen vast material spaces are the High Throughput techniques, which include statistical design of experiment, automated sample synthesis and characterization, data mining tools and "smart searching" strategies [Schröter 2007]. However, such methods may be cost intensive. Furthermore, the understanding and proving of physical mechanisms at the micro- and meso-scales is rarely possible in the framework of those methods. An alternative procedure enabling a fast and cheap access to the properties of hypothetic ferroelectrica is their computational simulation.

For theoretical investigations of macroscopic material behavior in dependence on the heterogeneous microstructure the micromechanical methods are usually applied [Böhm 1998]. The most part of so far utilized models report on linear properties (piezoelectric, dielectric and elastic coefficients) of BTO and PTO in dependence of the misorientation angle [Pertsev 1998], [Fröhlich 2001], [Jayachandran 2009]. The utilized methods, however, are usually not able to predict configuration of microscopic polarizations, the total polarization and strain and so, the effective material constants in the remanent state, which are essential for the design of applications. In the last decade a constitutive model for polarization switching in polycrystalline ferroelectric systems has been developed [Huber 1999], [Huber 2001]. It was realized as 2D and 3D finite element implementations ([Kamlah 2005] and [Pathak 2008]). However, only qualitative investigations of hypothetic bulk ferroelectric materials have been performed. Non-linear ferroelectric features of real bulk and thin film materials have not been calculated. Furthermore, each single grain has been modeled by a regular (cubic) finite element, which is not quite realistic.

The key input parameters of each micromechanical model are single-crystal piezoelectric, dielectric and elastic material constants. Typically, experimental single-crystal data are used as input parameters in the calculations. Such a procedure is, however, very inefficient on the purpose of designing new materials as before a simulation can be started single crystals of a new material have to be synthesized and experimentally characterized. Moreover, for some ceramics, e.g. PZT, single crystals could not been produced so far and the corresponding material constants are not available. A promising method to overcome this lack of data is multi-scale material modeling. In this approach the required input parameters are obtained from the models describing material on other length or time scales.

In the project COMFEM[2] first-principles-density-functional and shell-model simulations acting on the nano-scale of electrons and atoms, phase-field simulations acting on the meso-scale of ferroelectric domains and the micromechanical Huber-Fleck model governing on the micro-scale of ceramic grains have been envisaged in order to give a knowledge based description of macroscopic properties of ferroelectrics free of experimental input parameters. The micromechanical simulations and their connection to the models on the nano- and meso-scales of the described above combination scheme is one of the main topics of the present thesis. To our knowledge such a procedure has not been utilized for theoretical treatment of ferroelectric ceramic materials (in particular thin films) so far. We perform systematic calculations with different multi-scale coupling techniques and one-scale modeling procedures and discuss the results aiming at the prediction of macroscopic linear and non-linear properties of BTO, PTO and PZT thin films and bulk ceramics. Particularly, simulations of PZT ferroelectrics are very rare because of missing single-crystal coefficients. Investigations of the influence of the substrate clamping on the ferroelectric behavior of thin films were not published to our knowledge so far. It is demonstrated that the results of simulations allow the understanding of several previously non-conceivable experimental findings, such as an extremely low dielectric coefficient of PTO ceramics in comparison to the PTO thin film and BTO bulk ceramics. Furthermore, the scheme elaborated in this thesis has been shown to possess a high predictability under certain conditions. It might be therefore useful for simulation of further classes of ferroelectrics and for development of new ceramics, for which the experimental data are not yet available.

The basis for our micromechanical Huber-Fleck simulations are three-dimensional finite-element models with realistic and idealistic grain shapes. Particularly, non-linear calculations with three-dimensional realistic grain shapes have been quite rare so far. For the generation of realistic polycrystalline models stochastic methods of space tessellation (e.g. Voronoi or Laguerre mosaics) are commonly used. Previous investigations have outlined that even in the case of small two-dimensional models with several dozen cells only, these methods lead to problems in the subsequent meshing with finite elements [Fröhlich 2001]. In the present work a procedure is proposed, which generates meshable three-dimensional polycrystalline models with up to thousand grains. Another problem arising while using common Voronoi methods is that the log-normal distribution function of grain sizes, which is reported to be typical for the real polycrys-

---

talline ceramic materials, cannot be reproduced. In the present work we discuss existing approaches realizing realistic grain models and propose a new procedure generating 3D periodic extendable grain structures with a given lognormal grain size distribution and periodic extendable finite-element meshes. By means of the models produced with the proposed scheme FE simulations with periodic boundary conditions, giving a more realistic description of bulk material than the calculations without periodic boundary conditions, can be performed. Up to forty finite elements per grain in our models assure a higher precision of FE-results than the previous Huber-Fleck simulations with one finite element per grain only. The possibility of a big number of grains in the model is a further step towards realistic description of polycrystals. Finally, models with realistic grain shapes allow the study of structure-property-relationships.

The thesis is structured as follows: the background information on ferroelectric bulk and thin film ceramics is given in chapter 2; in chapter 3 the geometrical modeling of grain structures and finite-element meshes is discussed; physical models implemented on different size scales and their coupling possibilities are described in chapter 4; the following chapter 5 contains simulation results, their evaluation and discussion; the summary given in chapter 6 concludes this thesis.

2 Basics of the piezoelectric ceramics

This chapter describes phenomena of piezoelectricity, ferroelectricity and specific aspects of piezoelectric polycrystalline ceramics and thin films from the theoretical as well as from the experimental point of view.

2.1 The piezoelectric effect

When an ordinary solid is deformed by a tension T, a proportional strain S, related to T via a stiffness tensor s^E,

$$S = s^E \cdot T \tag{2.1}$$

is built up in the sample. In piezoelectric material, additionally to the strain an electric charge Q and, hence, the dielectric displacement D (since $Q = \oint_A D \cdot dA$) are created:

$$D = d \cdot T . \tag{2.2}$$

The direct piezoelectric effect describes the linear relation between the dielectric displacement and tension. The inverse piezoelectric effect characterizes the strain S occurring under an action of the electric field E:

$$S = d \cdot E . \tag{2.3}$$

Hereby, $\mathbf{E} = \left(E_i \right)_{i=1,2,3} = \begin{pmatrix} E_1 \\ E_2 \\ E_3 \end{pmatrix}$ and $\mathbf{D} = \left(D_i \right)_{i=1,2,3} = \begin{pmatrix} D_1 \\ D_2 \\ D_3 \end{pmatrix}$ are the first-order tensors,

$\mathbf{T} = \left(T_{ij} \right)_{i,j=1,2,3} = \begin{pmatrix} T_{11} & T_{12} & T_{13} \\ T_{21} & T_{22} & T_{23} \\ T_{31} & T_{32} & T_{33} \end{pmatrix}$ and $\mathbf{S} = \left(S_{ij} \right)_{i,j=1,2,3} = \begin{pmatrix} S_{11} & S_{12} & S_{13} \\ S_{21} & S_{22} & S_{23} \\ S_{31} & S_{32} & S_{33} \end{pmatrix}$ the second-order

tensors. $\mathbf{d} = \left(d_{ijk} \right)_{i,j,k=1,2,3}$ is a third-order piezoelectric tensor, which couples mechanical and electric fields. The latter tensor is defined as partial derivative of D_i with respect to T_{jk} evaluated at a constant electric field (subscript E) or as partial derivative of S_{ij} with respect to E_k at a constant stress (subscript T) [Jaffe 1956] :

$$d_{ijk} = \left(\frac{\partial D_i}{\partial T_{jk}} \right)_E = \left(\frac{\partial S_{ij}}{\partial E_k} \right)_T . \tag{2.4}$$

A further often utilized piezoelectric tensor is defined as

$$e_{ijk} = \left(\frac{\partial D_i}{\partial S_{jk}} \right)_T = \left(\frac{\partial T_{ij}}{\partial E_k} \right)_S \qquad (2.5)$$

Both piezoelectric tensors are correlated via elasticity tensor $c^E = \left(c_{ijkl}^E \right)_{i,j,k,l=1,2,3}$ of fourth order

$$c_{ijkl}^E = \left(\frac{\partial T_{ij}}{\partial S_{kl}} \right)_E \qquad (2.6)$$

$$e_{ijk} = c_{ijlm}^E d_{lmk} \qquad (2.7)$$

The stiffness of a material is characterized by a tensor of fourth order $s^E = \left(s_{ijkl}^E \right)_{i,j,k,l=1,2,3} = \left(c^E \right)^{-1}$ with

$$s_{ijkl}^E = \left(\frac{\partial S_{ij}}{\partial T_{kl}} \right)_E . \qquad (2.8)$$

The dielectric displacement D is directly correlated with polarization P as

$$D = \varepsilon_0 E + P \qquad (2.9)$$

Since in linear piezoelectric materials $D = \varepsilon \varepsilon_0 E \gg \varepsilon_0 E$ an approximation can be assumed

$$D \approx P . \qquad (2.10)$$

Under combined mechanical and electrical excitation the strain and electric displacement resulting from piezoelectric response can be written as follows:

$$\begin{aligned} S_{ij} &= s_{ijkl}^E T_{kl} + d_{kij} E_k \\ D_i &= d_{ikl} T_{kl} + \varepsilon_{ik}^T E_k \end{aligned} . \qquad (2.11)$$

$\varepsilon = \left(\varepsilon_{ik}^T \right)_{i,k=1,2,3}$ is the dielectric tensor of second order with

$$\varepsilon_{ik}^T = \left(\frac{\partial D_i}{\partial E_k} \right)_T . \qquad (2.12)$$

The described material tensors define deformation and electrical response in a loaded piezoelectric material. In order to obtain the corresponding displacement $u = \begin{pmatrix} u_1 \\ u_2 \\ u_3 \end{pmatrix}$ and electrical potential φ field equations

$$\begin{aligned} \nabla \cdot T &= 0 \\ \nabla \cdot D &= 0 \end{aligned} \qquad (2.13)$$

using (2.11) and

14

$$S = \frac{1}{2}\left(\nabla \boldsymbol{u} + \left(\nabla \boldsymbol{u}\right)^T\right)$$
$$\boldsymbol{E} = -\nabla \varphi$$

<div align="right">(2.14)</div>

have to be solved.

The equations (2.11) describe solely the linear response of the piezoelectric material to small perturbations. In practice, however, the piezoelectric materials typically show significant non-linear contributions to the response functions and, therefore, it is important to indicate, at which external field the coefficients ε_{ik}^T, d_{ijk} and s_{ijkl}^E have been measured. In the literature, the so-called "small signal" response at very small (sub-switching) external fields is often published. This is not identical to the "large signal" answer of a piezoelectric material to fields of high amplitude, which is relevant for actuator purposes. Nevertheless, the small and the large signal measurements are in most cases correlated. That is, the materials with high response to small fields are likely to show strong effects under the application of large fields as well. In the present work the effective material coefficients corresponding to the "small signal" excitations are calculated and compared with experimental values. However, the "large signal" coefficients can be obtained from our calculations as well. As it is common, the "large signal" evaluation of the polarization configuration and strain is presented in the results chapter.

2.2 The Perovskite structure

Pure piezoelectric materials (e.g. quartz) do not possess any electric dipoles if no external fields are applied. A ferroelectric material, in contrast, offers spontaneous strain and spontaneous polarization even at zero-field. The existence of spontaneous electric dipoles originates from the crystal structure.

Many ferroelectric materials crystallize in the so-called perovskite structure with the general formula ABO_3. This class of materials has got its name due to the German mineralogist Gustav Rose after his Russian colleague Lev Perovski. Above the critical temperature called Curie point the unit cell of a perovskite is cubic with the lattice constant a_0. Hereby, the large cations A are placed at the corners of the cubic cell of this ionic crystal, the smaller cation B in the cell's center, while the oxygen anions O at the centers of the facets (see Figure 2.1 a). The perovskite structure allows substituting of a vast variety of cations in its A-site (e.g. Ba, Pb, Ca, Na, Fe, Ce, Sr) and B-site (e.g. Ti, Nb, Zr, Ta). This opens a wide compositional space of materials. The centers of masses of negative and positive charges in the unit cell of a crystal coincide in the high

temperature phase of perovskites. The charges are mutually compensated and, hence, no permanent dipoles exist. Moreover, the symmetry operations applied to a B-site transform the crystal into itself. Therefore, the perovskite materials are neither piezoelectric nor ferroelectric above the Curie temperature. The high temperature phase is paraelectric.
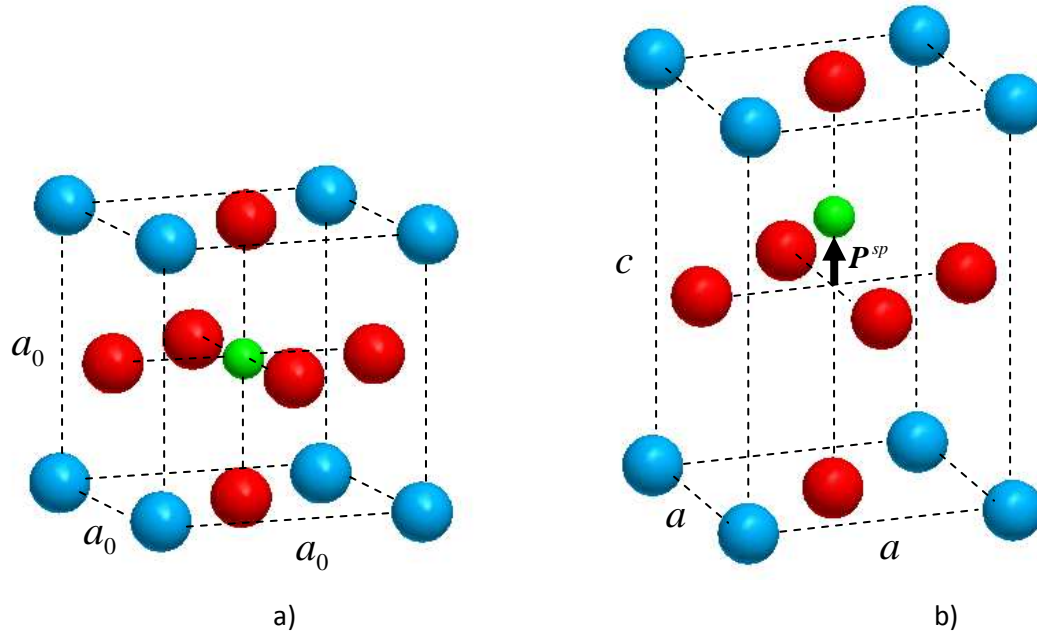
Figure 2.1: Perovskite structure with blue spheres as A-cations, small green sphere as B-cation and red spheres as oxygen-anions: a) cubic above the Curie temperature; b) tetragonal below the Curie temperature.

At the Curie point the perovskite materials undergo a lattice distortion. When the distortion occurs along the [100] direction of the crystal, the structure becomes tetragonal with the lattice constants a and c (see Figure 2.1 b). An orthorhombic or monocline structure is observed when the distortion occurs along the [110] direction. A rhombohedral structure is equivalent to a distortion along the [111] diagonal of the cubic lattice. In the distorted crystals the centers of positive and negative charges do not coincide anymore. Hence, the spontaneous polarization P^{sp} arises (see Figure 2.1 b).

The Curie point for $BaTiO_3$ (BTO) lies at 130°C. At this temperature the crystallographic ordering of the material transforms from the cubic to the tetragonal phase. At 0°C the tetragonal structure transits to the monoclinic one, and finally, at -90°C it becomes rhombohedral [Jaffe 1956]. The high-temperature cubic phase of $PbTiO_3$ (PTO) transforms into the tetragonal one similarly to BTO. However, the Curie temperature of 500°C is significantly higher than that of BTO. The tetragonal distortion and the spontaneous polarization of the tetragonal PTO widely exceed the

corresponding values for BTO (see Table 2.1) as well. The dielectric constants of PTO single crystal are, in contrast, significantly smaller than those of BTO (see Table 2.1).

|	BTO	PTO	PZT
$s^{sp} = \dfrac{c-a}{a}$	0.01	0.05	-
P^{sp} (C/m^2)	0.25	0.75	-
ε_{33}^{S} (-)	1910 [Pertsev 1998]	110 [Pertsev 1998]	-
d_{333} (pC/N)	110 [Pertsev 1998]	160 [Pertsev 1998]	-

Table 2.1: Spontaneous strain, spontaneous polarization and „small signal" ε_{33}^{S} and d_{333} material constants for BTO and PTO single crystals found in the literature.

In the most commonly industrially utilized ferroelectric material PbZr$_x$Ti$_{1-x}$O$_3$ (PZT) the Ti-cations are partially substituted by the Zr-cations. The cubic phase of Ti-rich PZT ($x < 0.5$) transforms at the Curie point into the tetragonal one, similarly to the transitions of the BTO and the PTO. In Zr-rich PZT ($x > 0.5$), instead, the cubic-rhombohedral transition occurs [Jaffe 1956]. At the morphotropic phase boundary ($x \approx 0.5$) both tetragonal and rhombohedral phases coexist at temperatures below the Curie point. In the simulations of PZT the emphasis on the tetragonal phase has been made due to the purpose of simplification and to the temporal limitation of the project. The tetragonal unit cell is depicted in Figure 2.1 b. The position of the B-cation is distorted along the c-axes in the direction of the upper oxygen-anion. In a similar way it could be displaced in the direction of any of five other oxygen-ions. Hence, the tetragonal perovskite provides six equivalent polarization directions and so six different types of ferroelectric domains. Under mechanical, electrical or thermic loading the polarization may switch by 90° or by 180° between these distinguished polarization directions. For orthorhombic distortions, twelve possible polarization directions exist, while for rhombohedral distortions eight directions of polarization within the unit cell are possible.

2.3 Piezoelectric ceramics

In many applications, ceramic polycrystalline materials are used because of their easier processing and molding compared to single crystals. Generally, ceramic is a polycrystalline system; i.e. a crystalline order exists only within individual crystallites or grains. Different grains originating from high temperature sintering of compressed ceramic powder (see Figure 2.2) are usually randomly oriented. Due to the absence of globally preferred orientations, no piezoelectricity can

be observed in an unpoled sample as the piezoelectric responses of the single crystallites cancel each other on average. However, this symmetry in ferroelectric materials can be broken by applying of an external electric or mechanical field. Such a poled or strained ceramic shows piezoelectricity or even ferroelectricity and can be incorporated in a wide range of applications. Nevertheless, the total polarization of a ceramic sample in the saturated state is usually significantly lower than the spontaneous polarization of a single crystal because of the randomly oriented grains and limited number of possible polarization directions (six for tetragonal phase). In order to overcome this restriction different techniques allowing a more unique orientation of crystal lattices of the grains have been developed recently [Soller 2010]. A ceramic can be imposed to such an orientation (texture) procedure during the tape casting by use of plate-like seeds. The structural texturing makes a high degree of polarization possible as the orientation of certain crystallographic directions within each grain can be aligned with the direction of an external electric field (see Figure 2.3). Tetragonal samples, in which the (100) crystal directions are parallel one to another in all grains, are called a-textured. The ceramic with global alignment of the (001) axes is known as the c-textured one.
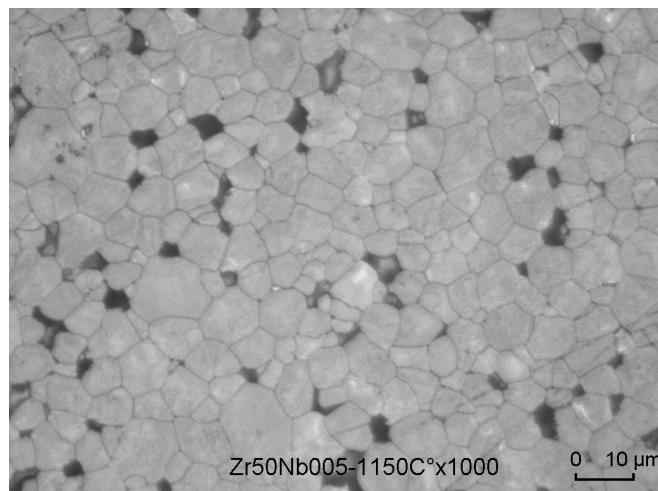

Figure 2.2: Polished section of a Nb-doped PZT bulk grain structure (courtesy of CeramTec).
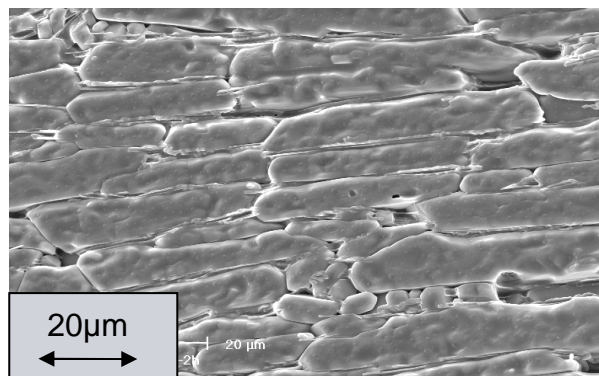

Figure 2.3: Polished section of a textured Al$_2$O$_3$-ceramics manufactured by the templated grain growth with Al$_2$O$_3$-seeds (courtesy of T. Soller, Siemens AG).

Due to the complex set of elastic and electric boundary conditions at each grain, ferroelectric crystals in a ceramic are always split into many domains with different polarization orientations (see Figure 2.4). The application of an external electric or mechanical field cannot change the crystallographic orientation of grains, but can reorient domains within individual grains in the directions next to the field. Many of the reoriented domains in ferroelectric materials do not vanish if the external field is removed. The sample possesses a so-called remanent polarization P^{rem} (see Figure 2.5) and so the remanent strain. In order to depolarize a previously poled ceramic sample a so-called coercive field E_c in the direction opposite to the present remanent polarization has to be applied (see Figure 2.5). With increasing electric field the ferroelectric domains aligned with the field grow, while those misaligned with the field shrink. This process leads to the movement of domain walls. Further, it gives rise of the ferroelectric (see Figure 2.5) and ferroelastic hysteresis, which are macroscopic property and can be measured experimentally. Hence, the macroscopic properties of the piezoelectric ceramics result from the properties of each domain and their interactions.
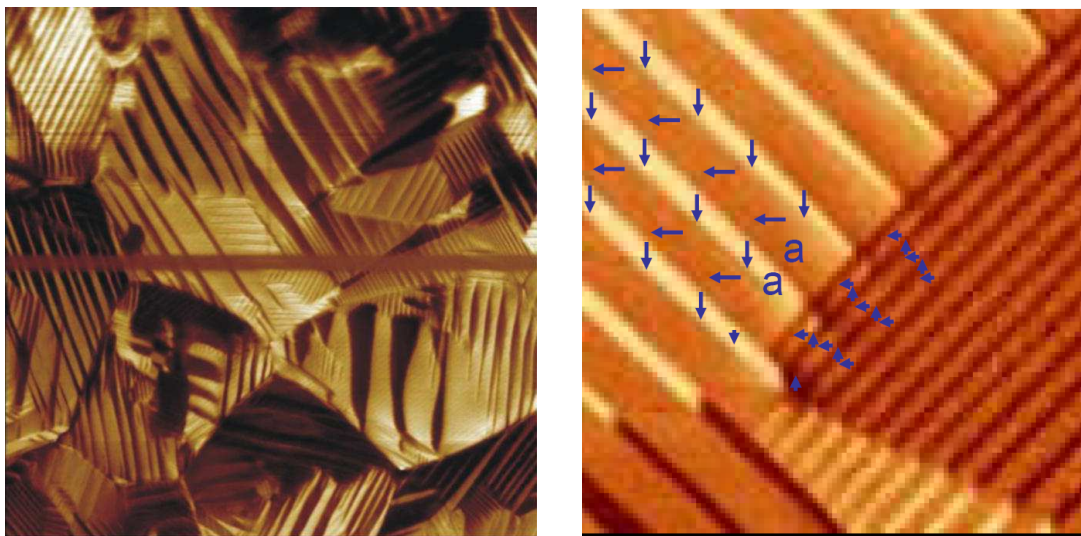
Figure 2.4: Piezoresponse Force Microscopy images of domain structure of single PZT grain with 90° and 180° domain walls (courtesy of G. Schneider, TU Hamburg).
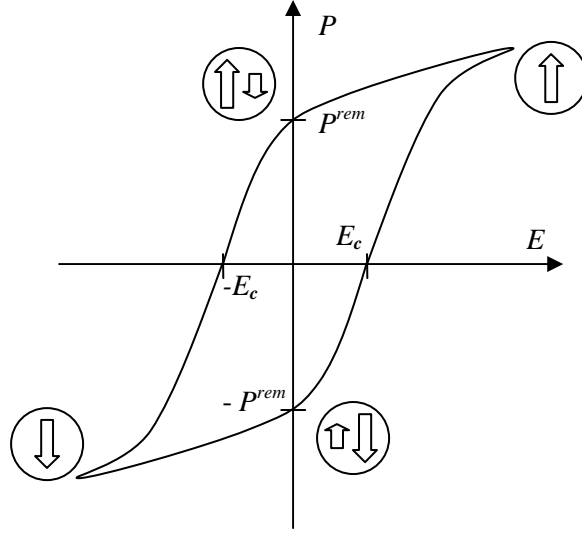
Figure 2.5: Sketch of a ferroelectric hysteresis. P is the magnitude of the polarization, E is the magnitude of the electric field, while the indices "rem" and "c" correspond to the notions "remanent" and "coercive" respectively.

One of the main goals of the present work is to compare simulation results on macroscopic properties of a ceramic with corresponding experimental data. In order to obtain a reasonable comparison, evaluation procedures in both cases should be congruent. Thus, in the following a standard experimental determination of "small signal" dielectric and piezoelectric constants is described. The theoretical calculation procedure of the constants is presented in section 4.5.

According to the ANSI IEEE standard 176 (1987) the dielectric constants of a ceramic can be evaluated from measurements of the capacitance of material plates provided with electrodes covering the surfaces. The AC voltage is used to measure the capacitance. Simultaneously, the DC bias field is used to pole the sample. The dielectric coefficient ε_{ij} and the polarization P_i can be derived directly from the measured capacitance C (or from the measured charge Q) and the bias voltage U_i, if the geometry of the sample is known. For a brick sample with the thickness d and the surface area A

$$\varepsilon_{ij}^* = \frac{D_i}{E_j} = \frac{Q \cdot d}{U_j \cdot A} = \frac{C \cdot d}{A}$$

$$P_i = \frac{Q}{A} - U_i \cdot d = \frac{C \cdot U_i}{A} - U_i \cdot d.$$

(2.15)

In order to obtain the dielectric permittivity ε_{ij}^* for constant stress the measurements have to be made at frequencies much lower than the lowest resonance frequency of the ceramic plate.

For the measurement of the piezoelectric coefficient a uniform electric field E (static or alternating with frequency much less than the fundamental resonance frequency) is usually applied. Under condition of constant (or better zero) stress, the strain S is measured by means of strain gauges or with interferrometric techniques. d_{ijk}^* is then obtained as

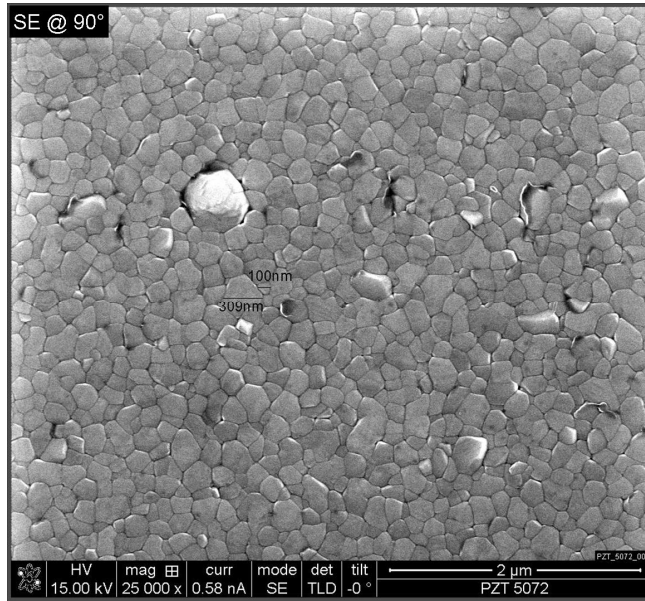$$d_{ijk}^* = \frac{S_{ij}}{E_k}.$$

(2.16)

Experimental results on effective dielectric and piezoelectric coefficients of bulk BTO and PTO ceramics are summarized in Table 2.2. The piezoelectric coefficient of BTO ceramic significantly exceeds the corresponding single-crystal value (see Table 2.1), while the d_{333}^* of PTO ceramic is much smaller than its single-crystal d_{333}. These discrepancies can be understood with help of simulation results obtained in the present work. Corresponding discussion is provided in section 5.3.1.

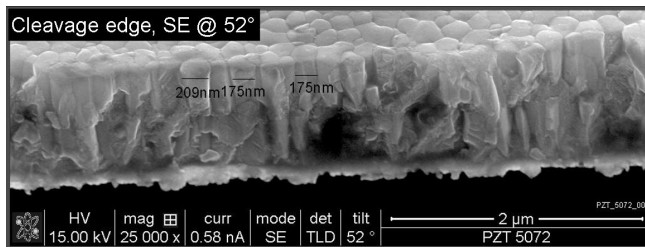|	BTO	PTO	PZT
ε_{33}^* (-)	1400 [Jaffe 1956]	50 [Shirane 1951]	585 [Landolt 2001]
d_{333}^* (pC/N)	190 [Jaffe 1956]	50 [Ikegami 1971]	173 [Landolt 2001]

Table 2.2: Effective dielectric and piezoelectric constants of bulk BTO und PTO ceramics found in the literature.

2.4 Piezoelectric thin films

In the investigations addressing the ferroelectric films several issues, which are not present or may be neglected in bulk ceramics, have to be clarified. The most important differences concern the grain shape and size, the film-substrate coupling as well as the magnitude of the coercive field. The thickness of ceramic thin films typically ranges between 100 nm and several micrometers. The prominent deposition methods are sputtering (or epitaxial growth) and the sol-gel technique. Depending on deposition technique, thin films have either columnar (see Figure 2.6 b and Figure 2.7) or equiaxial "bulk-like" structure. Furthermore, the choice of the deposition procedure in combination with the crystal structure of the substrate often yields preferred grain orientations in the thin film. For instance, the PZT-samples grown on the Si-substrate in the scope of the COMFEM project exhibit a (111) fiber texture, that means most of the [111] crystal directions are parallel to the substrate normal direction. As-grown PZT films usually exhibit non-zero polarization. To some extent this puzzling observation can be explained in the framework of our simulations as discussed in section 5.4.2.2.

SE @ 90°

100nm
309nm

HV 15.00 kV | mag ⊞ 25 000 x | curr 0.58 nA | mode SE | det TLD | tilt -0 ° | 2 µm | PZT 5072

PZT_5072_005

a)

Cleavage edge, SE @ 52°

209nm 175nm   175nm

HV 15.00 kV | mag ⊞ 25 000 x | curr 0.58 nA | mode SE | det TLD | tilt 52 ° | 2 µm | PZT 5072

PZT_5072_007

b)

Figure 2.6: REM-images of the sputter deposited PZT thin films: a) top view, b) side view.

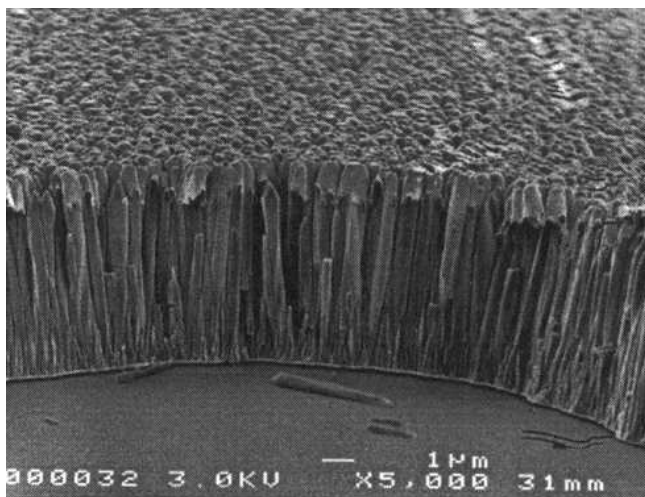000032   3.0KV   X5,000   31mm   1 µm

Figure 2.7: Sputter deposited ZnO thin films with columnar grains [Damjanovic 1998].

The grain and domain sizes of sputter deposited PZT thin films have been identified by means of Piezoresponse Force Microscopy (PFM) and Transmission Electron Microscopy (TEM) (see Figure

22

2.8) in the scope of the COMFEM project. The grain sizes have been found to range between 100 nm and 300 nm, the domain sizes – between 10 and 50 nm.

a)   b)
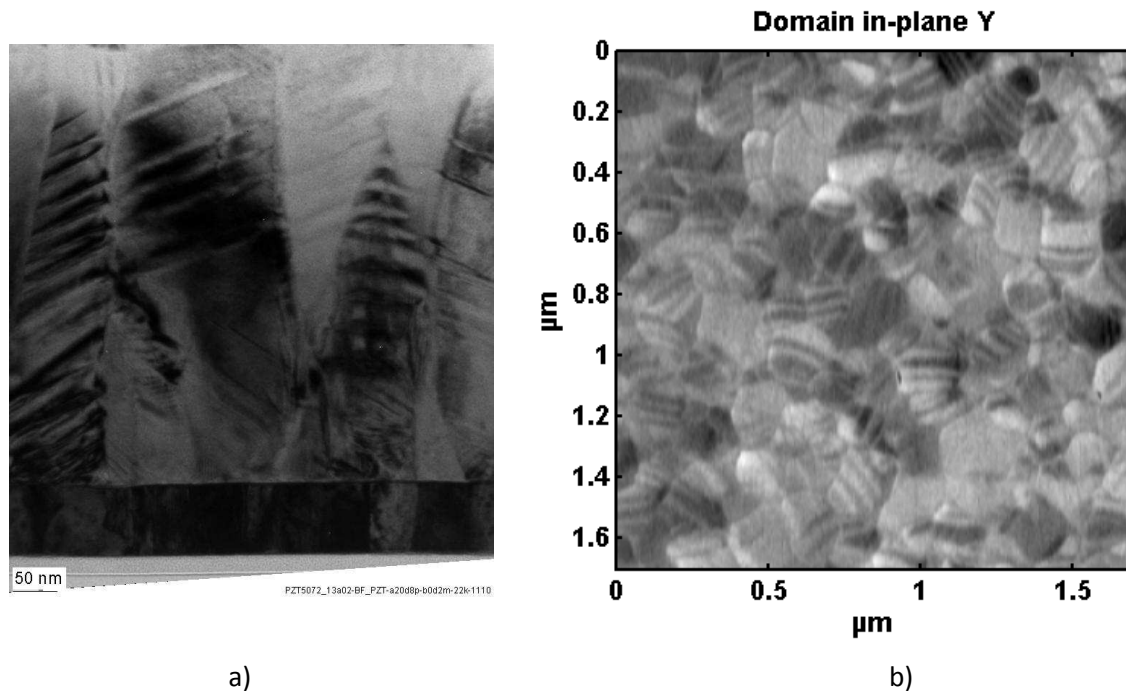
Figure 2.8: Transmission electron microscopy image of a (111)-textured PZT thin film: a) side view (TEM); b) top view (PFM).

Domain configurations of bulk PZT ceramics differ considerably from those of PZT thin films. The bulk samples reveal complex domain structures with all six domain types and 90°- and 180°- domain walls (see Figure 2.4) within one grain. The PZT thin films, in contrast, contain only two domain types with 90° domain walls in between (see Figure 2.8). The orientation of the domain walls arising between neighboring domains has been derived in [Romanov 1999] from the conditions of mechanical and charge compatibility: the domain walls are {101} boundaries, which is in agreement with TEM measurements performed within the COMFEM project (see Figure 2.8 a). The described domain configuration has been taken as the input data for the phase-field model of thin films. The results of these simulations have been subsequently used for derivation of the input parameters for the micromechanical simulations. The procedure is presented in detail in section 4.6.2.
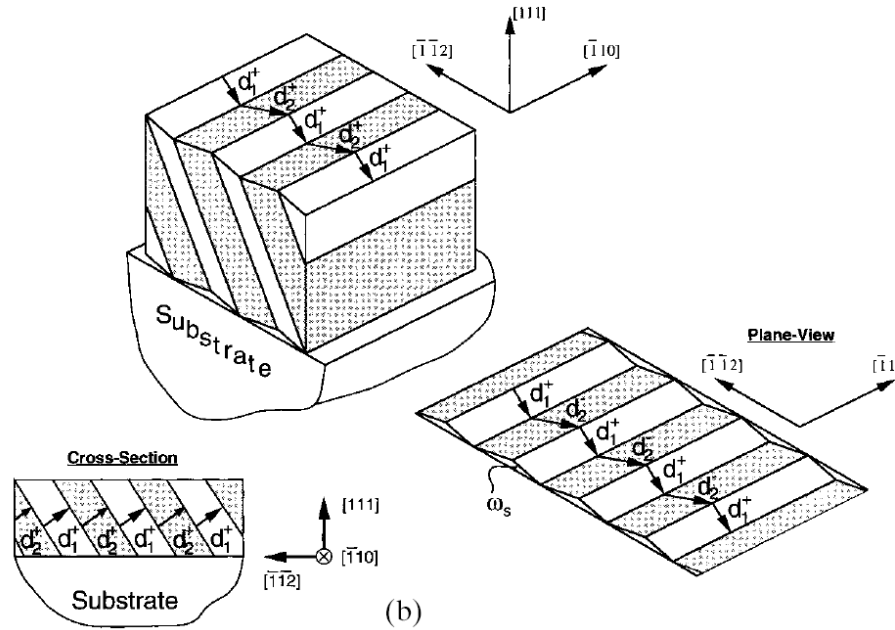
Figure 2.9: **Geometry of possible multidomain patterns in (111)-textured epitaxial PZT thin films [Romanov 1999].**

In order to motivate the theoretical model for thin films used in the present work the experimental setup for the determination of the effective dielectric and piezoelectric coefficients of thin films is described in the following in some detail. The experimental method differs to some extent from the procedure for bulk materials. Here, the bottom electrode is deposited on the substrate and the thin film is grown on the electrode. Hence, the thin film sample is constrained at the interface to the electrode. Because of the infinitesimal thickness of the thin films the strain gauges technique is inapplicable in this case. Instead, the Piezoresponse Force Microscopy (PFM) can be used. Beyond the determination of piezoelectric coefficients, PFM allows characterization of the domain configurations (see Figure 2.4 and Figure 2.8) of bulk ceramic samples and thin films. The PFM technique uses a conductive tip as a top electrode. The ferroelectric sample is grounded to the bottom electrode. When an AC voltage is applied to the electrodes, the inverse piezoelectric effect induces a local deformation of the sample under the tip simultaneously to the applied voltage. The local deformation causes deflections of the cantilever with the conducting tip. The direction of the deflection depends on the orientations of the electric field and the domain polarization. The movement of cantilever is sensed by the photodetector as movement of the laser spot (see Figure 2.10). The signal is then acquired using lock-in techniques. Since the excitation of the sample is rather local than global, this measurement procedure does not satisfy the IEEE standard described in the last section. Hence, the results on d_{33}^*

for thin films available in the literature are to some extent subjective. In the experimental data on the dielectric constant ε_{33}^* large differences exist as well (see Table 2.3).

	BTO	PTO	PZT
ε_{33}^* (-)	1500 [Desu 1993], 700 [Kamalasnan 1993], 385 [Tanaka 2004]	110 [Bao 2002]	800 [Bruchhaus 1998]
d_{333}^* (pC/N)	15 [Tanaka 2004]	-	60 [Bruchhaus 1998]

Table 2.3: Effective dielectric and piezoelectric constants of BTO, PTO and PZT thin films found in the literature.

Covering the piezoelectric thin film with a top electrode the effective dielectric material constant can be obtained in a similar way as in bulk sample (see section 2.3) by means of the capacitance measurement. Special attention must be directed to the fact that the thin films are not stress free during measurement. Nevertheless, the piezoelectric and dielectric coefficients are usually obtained using equations (2.15) and (2.16) as these measures are essential for the applications.
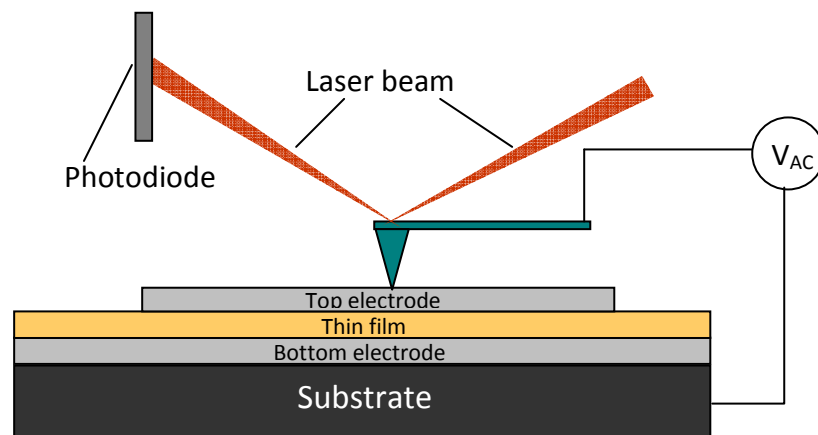
Figure 2.10: Experimental setup for electromechanical characterization of thin films by means of Piezoresponse Force Microscopy.

One of the most striking differences between bulk and thin film ferroelectrics is the coercive field strength, which may be an order of magnitude higher in films than in bulk materials of the same composition. The coercive electric field strength decreases with increasing of the film thickness. This effect can be qualitatively explained by the formation of the so-called depletion layer. This layer of up to few hundred nanometers thickness is an interface region nearby the metal electrodes. Within these regions, charge carriers are depleted and as a consequence, a so-

called built-in field evolves. At the interfaces, the dipoles are oriented according to the built-in field, when no external field is applied. To switch the oppositely oriented dipoles the external field has to overcome the bulk coercive field plus the built-in field.

In Figure 2.11 experimentally determined hysteresis loops of PZT films with different thicknesses are compared. The loop of the thinner film is more tilted. Until now this tilt was explained by the presence of a dielectric layer on the top of the ferroelectric, which is possibly a consequence of the production process. It has been supposed that the dielectric layer separates the bound charges, arising due to the ferroelectric polarization, from the compensating charges at the electrode and, thus, gives rise to the depolarizing field. In section 5.7.2., it will be shown that some other mechanisms like clamping by the substrate (or electrode) might also provide a tilt of the hysteresis curve. In order to differ between these several mechanisms corresponding simulations can be provided. The effects of depletion and dielectric layers have not been taken into account in the simulations performed so far. However, they can be easily incorporated into the proposed model.
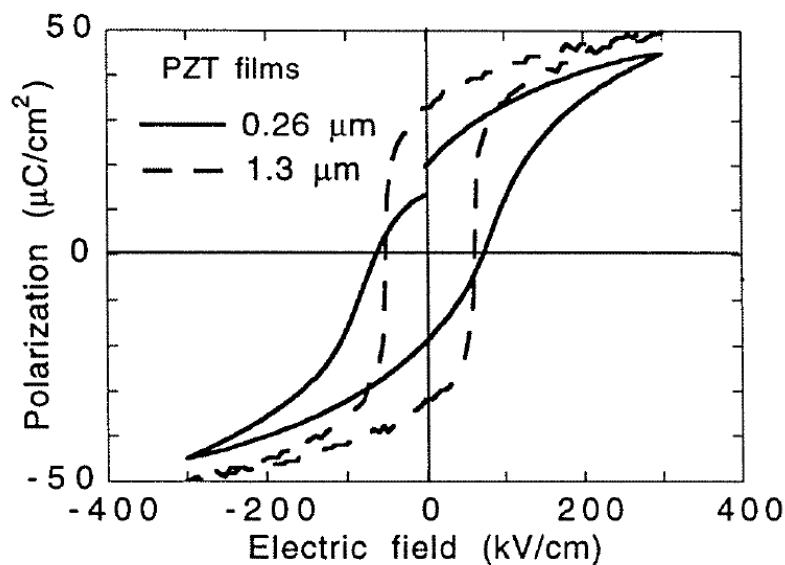
Figure 2.11: Ferroelectric hysteresis loops for two (111)-textured PZT films with different thicknesses [Damjanovic 1998].

Due to the connection of the film to the substrate or to an electrode, the ferroelectric thin film material is clamped in the in-plane direction. Additionally, due to the different coefficients of thermal expansion of substrate/electrode and thin film materials the latter underlies a tensile stress. Because of these effects the measured d_{33}^* and ε_{33}^* coefficients of a thin film sample are typically lower than in unclamped materials. In PZT ceramics, the clamping results in a reduction

of a macroscopically measured piezoelectric coefficient to approximately half the bulk value. In contrast, in PTO thin films the effective dielectric constant ε_{33}^{*} is significantly higher than the corresponding bulk value. Our simulations reveal the reasons for this exception as described in section 5.6.2.

3 Geometrical modeling of polycrystalline materials

A geometric model of a polycrystal is an important component for many types of mechanical, electrical, thermal etc. simulations of the grained materials on the micro-scale. In many cases idealistic models representing grains by cubes or tetrahedrons (see Figure 3.1) have been used for the micromechanical simulations of piezoelectric materials [Pathak 2008, Huber 2001]. As it will be shown in chapter 5 such a description is totally sufficient for certain problems and modeling procedures, e.g. for the calculation of effective material coefficients. In contrast, models including a separate description of the grain boundaries [Müller 2010] or a study of the influence of local loading conditions and local material properties require a more realistic geometric model of a polycrystal [Raether 2006].
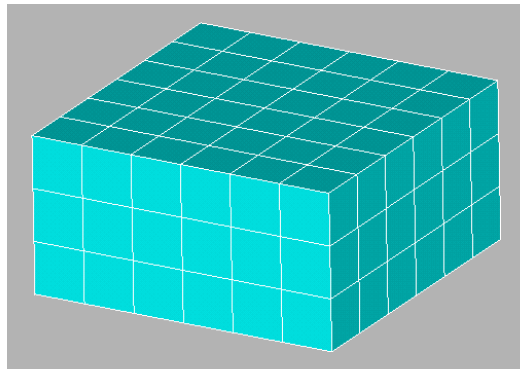
Figure 3.1: Idealistic model of a polycrystal. Polycrystal grains are represented by cubes.

One possible procedure to obtain such a realistic model of the grain structure is a digital reconstruction of a 2D image of a polished cross-section trough the bulk ceramic (see [Anteboth 2006]). However, such an approach delivers a 2D model with open, non-periodic boundaries, whereas a 3D periodically extendable structure is required. Moreover, the FE-meshing of the models reconstructed from polished cross-sections of ceramics often makes a huge number of elements necessary. It is therefore very expensive for numerical simulations.

In order to avoid the drawbacks mentioned above we use methods of stochastic geometry, such as random space tessellations, for modeling of a realistic 3D polycrystalline structure. In the present chapter several common methods of spatial tessellations, like Voronoi or Laguerre tessellation are introduced. In order to meet the characteristics of the real polycrystal structures, e.g. volume distribution of crystallites or distribution of the number of crystallite facets, several upgrades of the Voronoi und Laguerre processes have been developed. Among these advanced methods are rearrangement and thinning processes, which will also be described in the present

chapter. Subsequently, a novel thinning method for creation of 3D periodic extendable struc-
tures with lognormal grain size distribution will be presented.

A common problem of 2D as well as 3D grain generators consists in the fact that the produced
polyhedron structures cannot be meshed or the quality of the FE-mesh is very poor [Fröhlich
2001]. In the last section a method is presented which assures that the produced 3D grain
structures are meshable with a very high reliability.

3.1 Voronoi tessellations

In this chapter the benefits and deficiencies of different kinds of Voronoi tessellations are dis-
cussed.

3.1.1 General procedure

In general, a tessellation or a tiling of the metric space S is a collection of cells C_i, $i \in N$,
$N = \{1...n, \ n \in \mathbb{N}\}$ with no overlaps and no gaps:

$$S = \bigcup_{i \in N} C_i, \ C_i \bigcap_{\substack{i,j \in N \\ i \neq j}} C_j = \varnothing. \tag{3.1}$$

Each Voronoi tessellation is based on a set of generating points $P = \{\boldsymbol{p_1}, \boldsymbol{p_2}, ...\} \subset S$. These
points are usually randomly distributed within S. Each point $\boldsymbol{p_i}$ defines one Voronoi cell
$V(\boldsymbol{p_i})$. This Voronoi cell contains all the points $\boldsymbol{v} \in S$, whose distance to $\boldsymbol{p_i}$ is smaller than that
to other generating points $\boldsymbol{p_j}(j \neq i) \in P$:

$$V(\boldsymbol{p_i}) = \bigcap_{\boldsymbol{p_j} \in P \setminus \{\boldsymbol{p_i}\}} \{\boldsymbol{v} \in S \ | \ \|\boldsymbol{v} - \boldsymbol{p_i}\| \leq \|\boldsymbol{v} - \boldsymbol{p_j}\|\}. \tag{3.2}$$

The Voronoi cells are closed and convex. In the present work $\| \ \|$ is an Euclidian metric
$\|x\| = \sqrt{x_1^2 + x_2^2 + x_3^2}$ and S is a closed subset of $\mathbb{R}^3$ for the geometric models of equiaxial
polycrystals, e.g. $S = \{(x, y, z) \in \mathbb{R}^3 \ | \ |x| \leq 0.5, |y| \leq 0.5, |z| \leq 0.5\}$. For the columnar structures
(see section 2.4) S is a closed subset of $\mathbb{R}^2$ as shown in Figure 3.2.
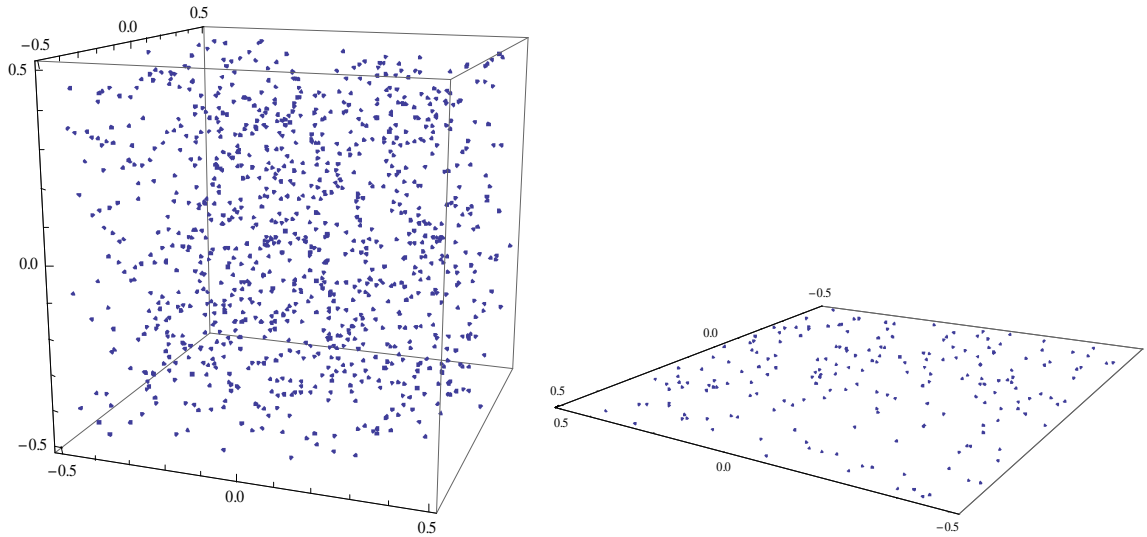
Figure 3.2: Generating points for equiaxial (left) and columnar (right) structures.

For determination of the boundaries of the Voronoi cells, firstly each generating point is connected with its next neighbours via the Delaunay triangulation, see Figure 3.3 (right). By means of Delaunay triangulation triangles (tetrahedrons in 3D) are generated with the property that no further generating points lie within the circumscribed circle (sphere in 3D) , see Figure 3.3 (right).
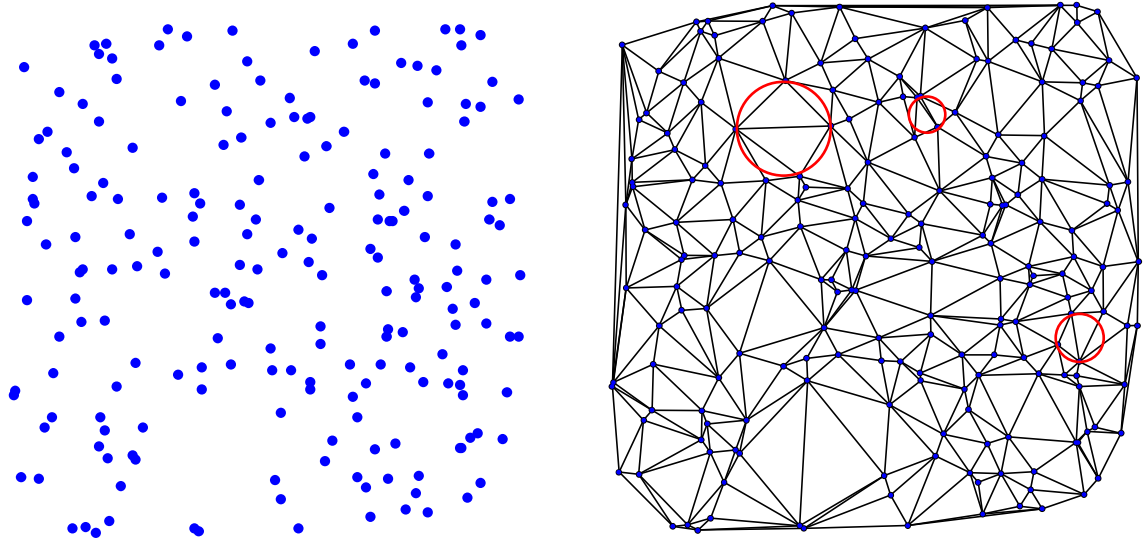
Figure 3.3: Generating points (left) and the corresponding Delaunay triangulation (right) in 2D.

The perpendicular bisectors of the Delaunay mesh enclose the Voronoi cells (red shaded region in Figure 3.4). In the 3D case perpendicular bisectors are not lines but planes. A result of a 3D Voronoi tessellation is shown in Figure 3.5 a. It is often called the Voronoi diagram. It can be shown that the Delaunay triangulation is a dual graph of the Voronoi diagram. This means that

the Voronoi tessellation of a Voronoi diagram is the Delaunay triangulation. The Voronoi tessellations are produced by means of the free software PyXL [PyXL] in the present work.
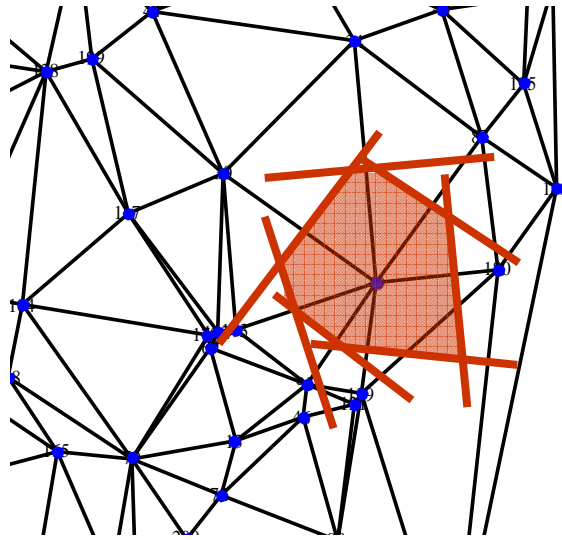
Figure 3.4: Construction of a Voronoi cell by means of the perpendicular bisectors of the Delaunay sides.

3.1.2   Poisson-Voronoi diagram

The set of generating points should be chosen in such a way that the corresponding Voronoi diagram accurately describes the polycrystalline microstructure. An important requirement for the set of generating points (see section 3.1.1) is therefore its homogeneity and isotropy. This means that the number of generating points per unit area n has to follow a distribution function which is translation- and rotation-invariant. An example of such a distribution is the Poisson distribution function

$$P(n) = \frac{e^{-\lambda} \lambda^n}{n!}$$

with the mean point density λ. The corresponding Voronoi tessellation is called Poisson-Voronoi (PV) diagram.
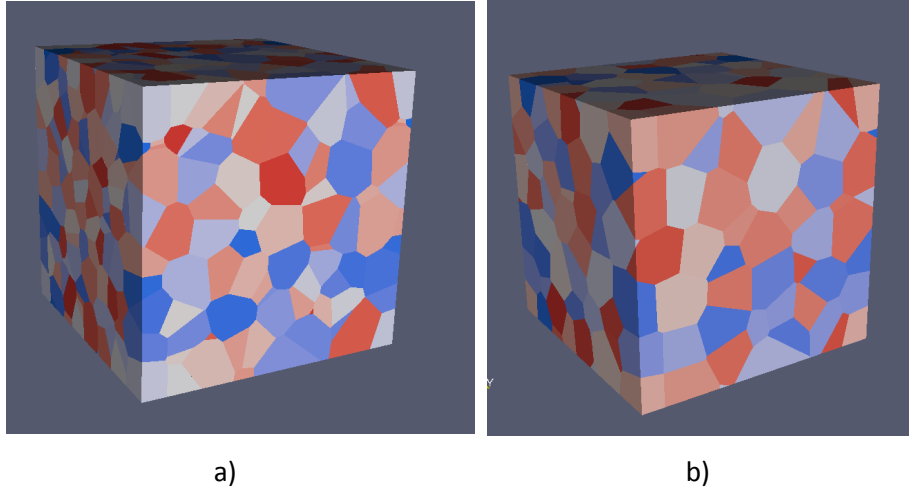
Figure 3.5: An example of a polycrystalline model obtained via 3D Poisson-Voronoi diagram (a) and 3D Hard-Core-Voronoi diagram (b).

Numerous properties of PV tessellations, e.g. distribution of volumes, number of facets per cell or edge length, have been derived analytically or by means of simulations [Ohser 2000, Okabe 1992, and Muche 1992]. Within the PV procedure a vertex is shared by four edges and an edge - by three facets, which is consistent with observations in real materials. However, some inadequate features of the PV diagram do exist in representation of realistic polycrystals.

Firstly, the PV cells do not look as globular and regular as ceramic grains. A second inadequate feature concerns grain size distribution. The PV cells are assumed to obey the gamma distribution [Kumar 1992], whereas ceramic grains are found to follow a lognormal distribution [Nettleship 2002, Rhines 1982, Okazaki 1972]. Both distributions are fairly similar, as it can be seen in section 3.3.1 or in [Vaz 1988, Nettleship 2002]. Nevertheless, the goodness of the gamma fit was systematically better than the goodness of the lognormal fit for PV cells, which is on contrary to the real material.

Another drawback of the PV tiling concerns the coefficient of variance cv of the grain volumes, which is defined as standard deviation of the grain volumes σ_V divided by the mean grain volume $\bar{V}$:

$$cv = \frac{\sigma_V}{\bar{V}} \, . \tag{3.3}$$

The corresponding definition for the coefficient of variation of grain size d reads:

$$cv_d = \frac{\sigma_d}{\bar{d}} \, . \tag{3.4}$$

Hereby, $\overline{d}$ and σ_d are the mean and the standard deviation of grain diameters . The *cv*-value of a PV partition is invariant and equal 0.424 [Kumar 1992], whereas in real polycrystalline metals *cv* ranges from 1.1 to 2.1 [Rhines 1982]. The *cv*-values for the grain sizes of alumina ceramics vary between 2 and 3 [Nettleship 2002].

3.1.3   Hard-core-Voronoi diagram

One method, which can help to overcome the lack of regularity and globularity of the PV partition, is Hard-core Voronoi (HCV) tessellation. In this approach a minimum distance $2r$ between two generating points is defined. A geometrical interpretation of this procedure is as follows: each generating point is a center of a sphere with a core of radius r. Within this core no other generating points may exist (hard core). The cell centers (generating points) which do not fulfill this constraint are deleted and thus the original point set becomes thinned. For that reason the Hard-core approach is a special case of the so called thinning processes. A 3D Hard-core-Voronoi diagram is shown in Figure 3.5 b). The Voronoi cells are more globular and regular than PV cells of Figure 3.5 a). However, it was found that the HCV cell volumes as well as these of the PV process follow the gamma distribution function [Reis 2006]. Moreover, the *cv*-value is even smaller than that of the PV partition (0.424), which exhibits an even larger deviation from experimental values presented in section 3.1.2, see also Table 3.1.

3.1.4   Cluster-Voronoi diagram

A Cluster-Voronoi (CV) partition is typically produced from a point field, where the density of the generating points strongly varies within the space to be tessellated. One possibility to do so is to systematically define the spatial elements (e.g. slices or cubes) with different point densities. An alternative procedure would be to identify such spatial elements (e.g. spheres) around the generating points of some space tessellation (e. g. PV tessellation). Two examples of a CV tiling are presented in Figure 3.6.
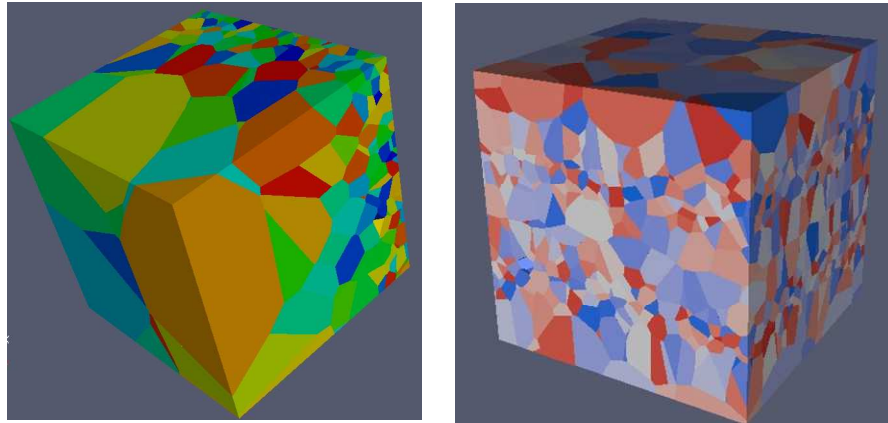
Figure 3.6: Cluster-Voronoi tessellations.

In CV diagrams the coefficient of variation is arbitrary adjustable, but the globularity and the lognormal distribution of grain sizes are missed.

3.1.5 Constrained Voronoi diagram

Xu and Li have proposed a rearrangement procedure for generating points from a PV mosaic with the intent to produce 3D Voronoi diagrams with lognormal distribution of grains [Xu 2009]. In this approach the generating points are rearranged by means of the Monte Carlo Method until the penalty distribution function is fulfilled with a certain tolerance. However, the goodnesses of the different fit functions, e.g. lognormal, gamma or Gauß, were not compared for a certain adjustment procedure, so it was not proven that the adjusted function is the best fit. Moreover, the *cv*-values for the constrained Voronoi diagram range from 0.1 to 0.445, which is beyond the intervals typical for real metallic polycrystals (see Table 3.1).

3.1.6 Summary and discussion

The geometric features of different Voronoi tilings discussed in the last sections are summarized in Table 3.1. All presented space tessellations have drawbacks in the description of the geometric properties of real polycrystalline materials. Therefore, in section 3.2 the method of Laguerre tessellations is considered and in section 3.3 a proposal for a novel constrained thinning Voronoi procedure is given. It will be shown that both approaches are superior in the description of real polycrystals.

Type of tiling	Globularity	Lognormal grain size distribution	Coefficient of variation cv
Poisson-Voronoi	no	no	0.424 [Kumar 1992]
Hard-core-Voronoi	yes	no	0.0…0.424
Cluster-Voronoi	no	no	arbitrary
Constrained Voronoi	unknown	Comparison with gamma is missed	0.1…0.445
Real material	yes	yes	1…3 [Rhines 1982], [Nettleship 2002]

Table 3.1: Comparison of the characteristics and structure parameters of different Voronoi tessellations and real materials.
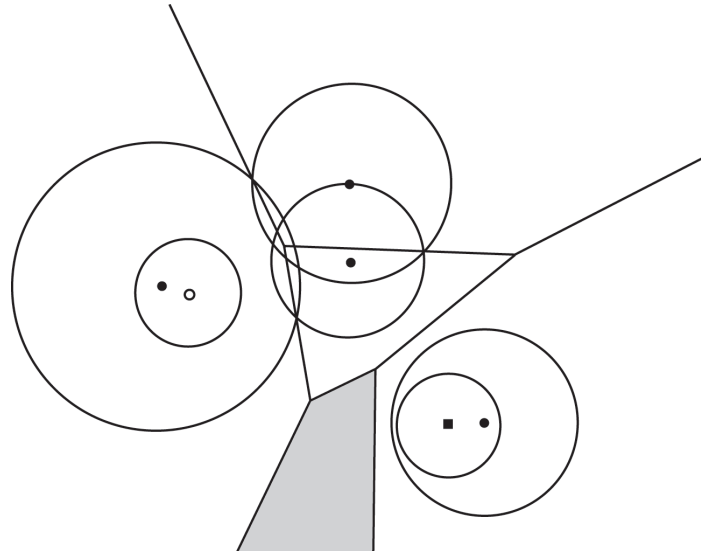
3.2 Laguerre tessellation

Laguerre tessellation can be considered as a weighted Voronoi diagram. In this procedure a weight $w_i \in \mathbb{R}$ is assigned to each generating point p_i of a set P. By that means a weight set $w = \{w_1, w_2, ..., w_n\}$ is formed. Similarly to the Voronoi tessellation a cell of the Laguerre tiling corresponding to the generating point p_i is defined as

$$L(p_i) = \bigcap_{p_j \in P \backslash \{p_i\}} \{v \in S \ | \ \|v - p_i\| \leq \|v - p_j\|\}. \tag{3.5}$$

However, the distance between p_i and any other point v in Laguerre geometry is measured as

$$\|v - p_i\| = \sqrt{|v - p_i|^2 - w_i^2} \ . \tag{3.6}$$

The Laguerre cells are space-filling convex polyhedrons without overlapping similarly to the Voronoi cells. However, in a general case not every point $p_i \in P$ generates a tessellation cell or lies within the generated cell. An example of a Laguerre diagram based on six generating points, published in [Lautensack 2007], is presented in Figure 3.7. The circle radii characterize the assigned weights. Here, the point o does not generate a cell. The point ▪ generates the shaded region but does not lie within this cell.

Figure 3.7: The Laguerre diagram of six generating points in $\mathbb{R}^2$ [Lautensack 2007]. The circle radii characterize the assigned weights. The point ○ does not generate a cell. The point ▪ generates the shaded cell.

The cells of the Laguerre tessellation are interconnected in a topological manner in the same way as the grains of polycrystalline materials. In contrast to the Voronoi tessellation, grain boundaries are not obligatorily located in the middle of the Delaunay bond (see section 3.1.1) due to the different weights of generating points. Therefore, the coefficient of variation of cell sizes is not a fixed value as in PV diagram and can be varied in a broad range.

For an accurate description of polycrystalline materials and their properties (see Table 3.1) Fan et al. have proposed a Laguerre tessellation based on random closed packing of spheres (LRCPS) [Fan 2004]. The procedure was investigated in more detail in [Redenbach 2009]. In the LRCPS model the generating points are centers and the weights are equal to the sphere radii of a closed packing with lognormal distributed sphere volumes, see Figure 3.8. The random dense packing can be simulated using various algorithms based on, e.g. sequential generation, collective rearrangement, molecular dynamics or gravitation. In [Fan 2004] and [Redenbach 2009] modified collective rearrangement procedures were utilized. The distribution function of spheres is shown to be strongly inherited by the cells of the Laguerre tiling. In this type of Laguerre partition every generating point produces a cell and the point lies within this cell.
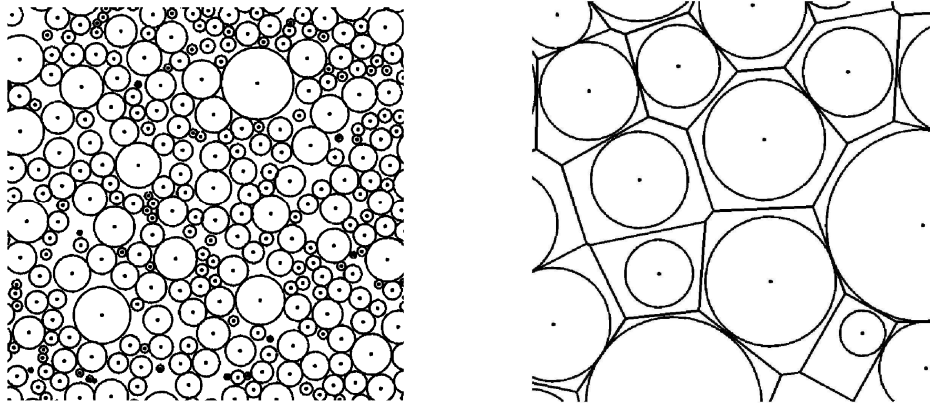
Figure 3.8: Cross-section of a closed packing of spheres and its Laguerre tessellation [Fan 2004].

The LRCPS diagram was shown to be superior to the PV tessellation in the description of realistic polycrystals because of its advantageous geometric properties.

Voronoi and Laguerre tessellations are special cases of the Johnson-Mehl tessellation. In the general case the generating points are nucleated in a time-dependent manner with a constant frequency. The cells around the nucleated points grow with a constant velocity in all directions [Pineda 2004]. The described model is physically motivated. It is therefore well suitable for the description of growth processes. However, the cell boundaries are non-planar in this computational procedure (see Figure 3.9). Therefore, they cannot be treated numerically as effectively as Voronoi and Laguerre cell facets.
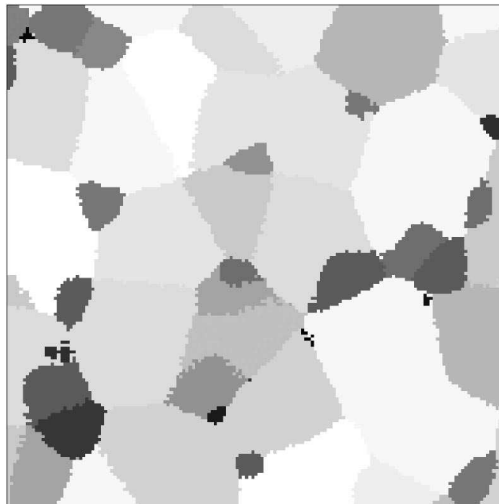

Figure 3.9: A two-dimensional Johnson-Mehl tessellation. Different grey intensities correspond to crystals with different birth times [Pineda 2004].

3.3 A novel constrained hard-core thinning process

In the present section a novel thinning process is proposed, evaluated and discussed.

3.3.1 Procedure and results

The approach is similar to the Hard-core Voronoi (HCV) method (see section 3.1.3). The difference concerns the hard-core radius, which is not constant but is calculated as

$$r_{HC} = \left(\frac{3V_{HC}}{4\pi}\right)^{\frac{1}{3}}$$

(3.7)

from the hard-core volumes V_{HC} following the lognormal distribution function:

$$f(V_{HC}) = \frac{1}{\sqrt{2\pi}\sigma V_{HC}} e^{-\frac{(\ln V_{HC} - \mu)^2}{2\sigma^2}} .$$

(3.8)

In (3.8) μ is the mean and σ the standard deviation of $\ln V_{HC}$.

From the equations (3.7) and (3.8) it follows that the distribution function for the Hard-core radii is not exactly lognormal but very similar:

$$f(r_{HC}) = \frac{1}{\sqrt{2\pi}\sigma\left(\frac{4}{3}\pi r_{HC}^3\right)} e^{-\frac{\left(\ln\left(\frac{4}{3}\pi r_{HC}^3\right) - \mu\right)^2}{2\sigma^2}} = \frac{1}{\sqrt{2\pi}\frac{\sigma}{3}\left(4\pi r_{HC}^3\right)} e^{-\frac{\left(\ln r_{HC} - \frac{1}{3}\left(\mu - +\ln\frac{4}{3}\pi\right)\right)^2}{2\left(\frac{\sigma}{3}\right)^2}} .$$

(3.9)

According to the Hard-core procedure generating points having the distance less than $2r_{HC}$ to the center of the Hard-core are eliminated. Subsequently, the Voronoi tessellation of the thinned point field is performed. In the following it will be shown that by means of the described Constrained Hard-core Voronoi (CHCV) procedure a grain ensemble with lognormal volume and diameter distributions as well as an arbitrary variation of grain sizes can be created.

The CHC process with different distributions of the Hard-core sphere volumes was applied to sets of about 25 000 generating points. Equiaxial and columnar structures with 5000 to 20 000 grains were produced on the basis of CHC point fields. In Figure 3.10 two examples of columnar structures with different σ-values are shown. Corresponding distributions of the equivalent grain diameters are presented in Figure 3.11. The fit functions were calculated by the method of least squares. For the left structure the cv_d-value was obtained according to the definition (3.4) as 0.1, while for the grain ensemble on the right it is 1.2. Obviously, within our method the coefficient of variation can be adjusted by the σ-value of distribution function of the hard-core set. In Figure 3.12 an equiaxial grain structure with about 7500 grains and cv-value of 1.1 is plotted. For the evaluation of the grain sizes the cut off edge grains were eliminated.
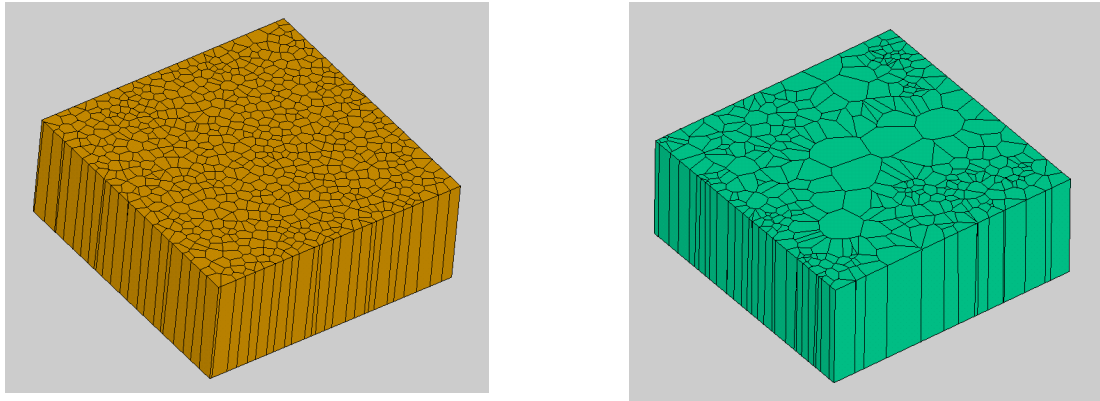
a) $\sigma = 0.06$ b) $\sigma = 0.29$

Figure 3.10: Two cuttings of columnar structures with different coefficients of variance.
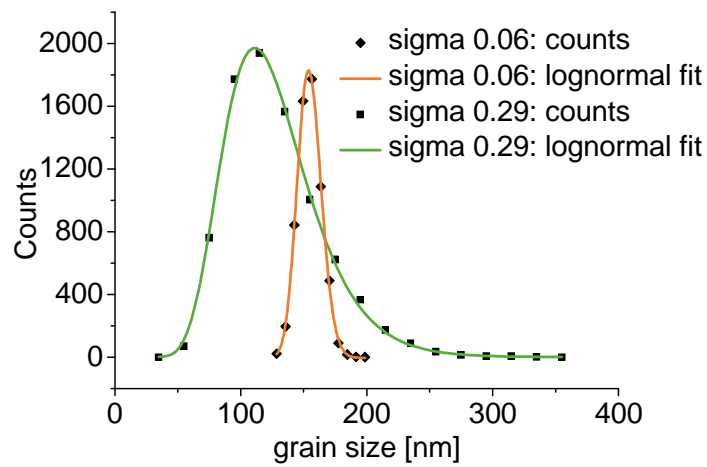

Figure 3.11: Distribution of equivalent grain diameters for the columnar structures from Figure 3.10.
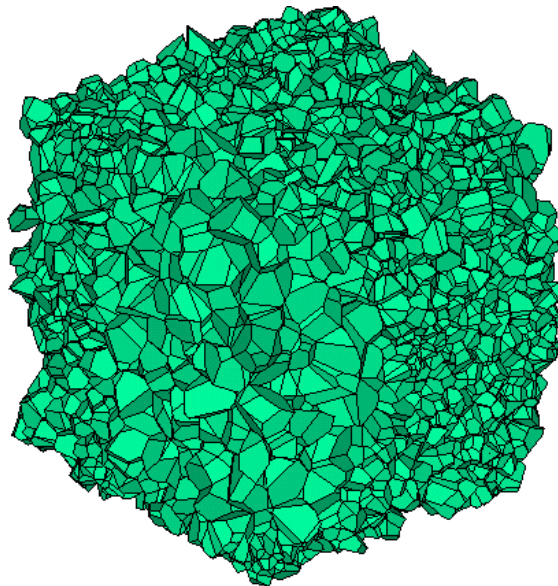
Figure 3.12: Equiaxial grain structure with lognormal distribution of the grain volumes and coefficient of variation of 1.1.

In Figure 3.13 distributions of the CHC spheres volumes and corresponding Voronoi cells are compared. The cell volumes of the Voronoi tessellation are significantly larger than these of the CHC spheres. This effect is due to the CHC spheres, which are non-space-filling and which are not rearranged to form a closed packing, whereas the resulting Voronoi cells are space-filling. However, if the volumes of CHC spheres follow the lognormal distribution, the volumes of the corresponding CHCV cells can be expected to obey the same type of distribution. The validity of this statement is demonstrated in Figure 3.14 - Figure 3.19.
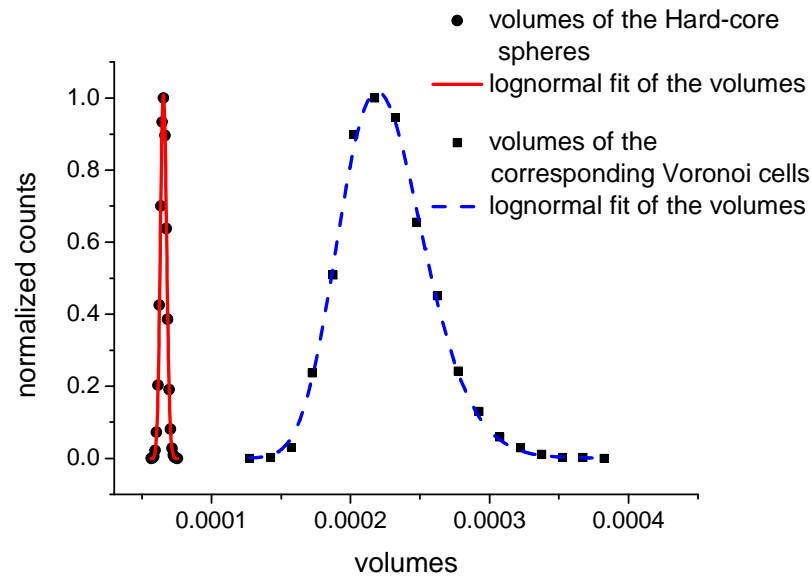
a) $cv = 0.1$
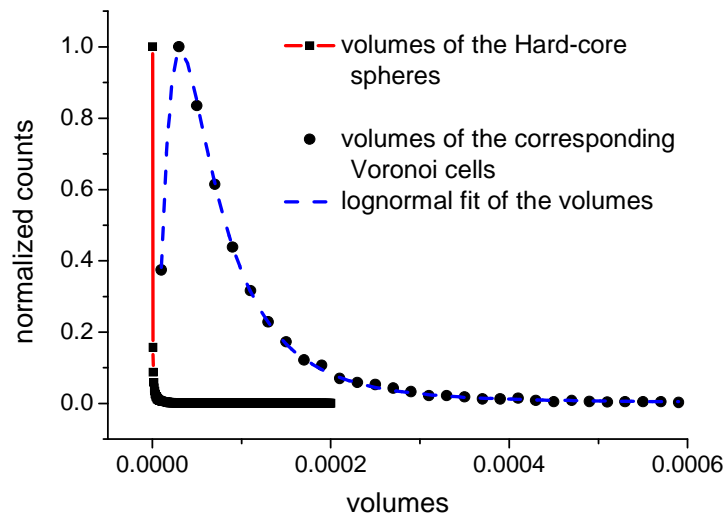
b) $cv = 1.1$

Figure 3.13: Distributions of the CHC sphere volumes and the corresponding CHCV tessellation: a) grain structure with 19 266 cells and $cv = 0.1$; b) grain structure with 16 075 cells and $cv = 1.1$.
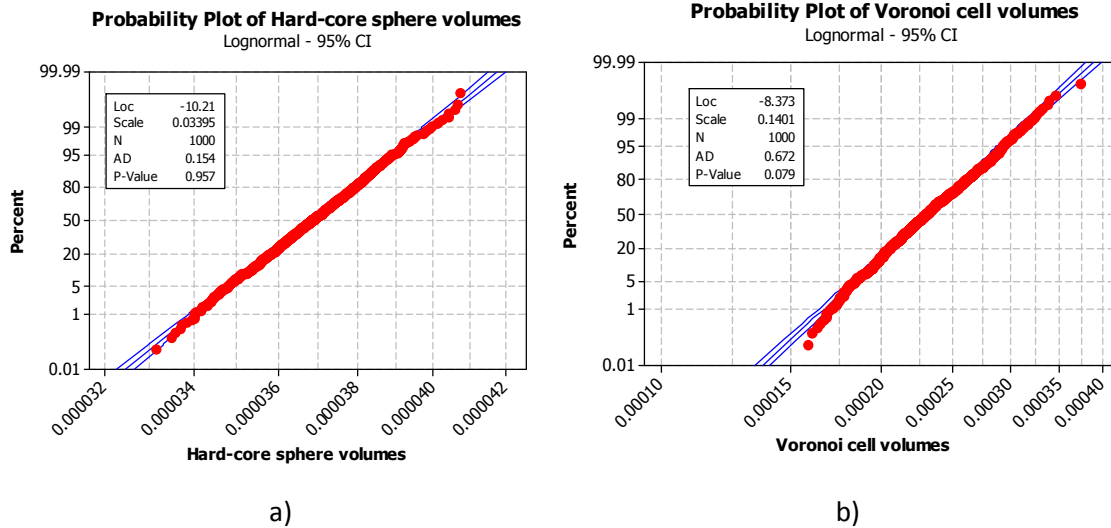
Figure 3.14: **Lognormal probability plots of the CHC sphere volumes (a) and the CHCV grain volumes (b) for a 1000 cell subset of a 19 266 grain structure with *cv* = 0.1.**
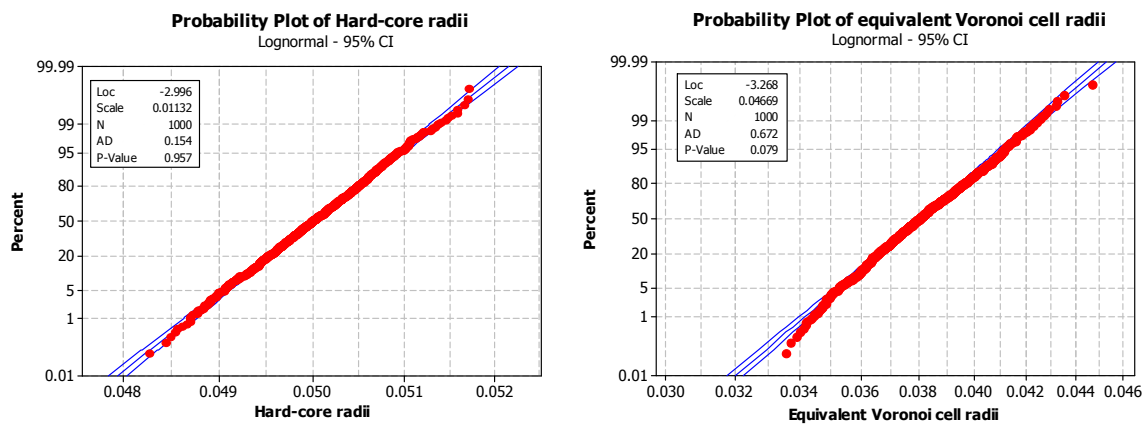
Figure 3.15: **Lognormal probability plots of the CHC radii (a) and the CHCV equivalent grain radii (b) for a 1000 cell subset of a 19266 grain structure with *cv* = 0.1.**

For the determination of the goodness of the distribution fit the Anderson-Darling (AD) test has been chosen as it was found to be one of the best statistics for detecting most departures from the normality [Stephens 1974]. In particular, the AD test was found to be more sensitive than the prominent χ^2-Test utilized in [Fan 2004] or the Kolmogorov-Smirnov statistic performed in [Nettleship 2002]. One of the most important characteristics of the AD test is the A^2 value, which measures a squared distance between the hypothesized distribution F (e.g. lognormal, gamma or Gauss) and the empirical sample cumulative distribution function F_n. In the first step, the empirical data $\{V_1 < V_2 < ... < V_N\}$ will be rearranged in ascending order. Then, the AD statistic is calculated as

$$A^2 = -N - \frac{1}{N} \sum_{i=1}^{N} (2i-1) \left[\ln F(V_i) + \ln \left(1 - F(V_{n+1-i}) \right) \right]. \qquad (3.10)$$

The AD test makes use of the fact that, when the sample data does arise from the supposed distribution, the data can be transformed to a uniform distribution and tested for uniformity with a distance test. The cumulative function of a uniform distribution is linear ascending (middle blue line in Figure 3.14). It can be, therefore, easily compared with the transformed sample data (red points in Figure 3.14).

Another quantitative measure of the AD test is the so-called p-value, which represents a probability that the rejecting of a supposed distribution function is a mistake. The calculation procedure for the p-value is variegated. It will be determined from the A^2 statistic and the table given in [D'Agostino 1986]. In the following, the fit distribution function and the characteristic A^2 and p values were calculated by means of the software Minitab.

In Figure 3.14 a) almost all points of the cumulative frequency of the CHC sphere volumes lie within the confidence interval of the supposed distribution function (boundary blue lines). Values "Loc" and "Scale" in the diagram legend symbolize parameters σ and μ of the fit function (3.8). The measure "AD" represents the AD statistics A^2.

The hypothesis that the CHC sphere volumes obey the lognormal distribution at the significance level 0.05 is accepted as the p-value is much larger than 0.05. In Figure 3.14 b) the cumulative frequency in the area of the small Voronoi cell volumes (red) is slightly below the confidence interval (blue). The detailed discussion of reasons for this effect will be given in section 3.3.2. It should be noted that the hypothesis of the lognormal distribution of the grain volumes is accepted since the p-value 0.079 is larger than 0.050. In contrast, the assumption that the CHCV cell volumes follow gamma or Gauss distribution is rejected since the corresponding p-values are smaller than 0.05 (see Figure 3.16). Furthermore, as the AD value of the lognormal fit is smaller than that of the gamma and Gauss fits the lognormal distribution function is identified to be the most suitable.

Interestingly, the hypothesis of the lognormal distribution is accepted for the Hard-core radii and for the equivalent Voronoi cell radii as well. The p- and the AD values are equivalent with those for the corresponding volumes, although the fit parameters are different (compare Figure 3.14 and Figure 3.15).

Figure 3.16: Gamma (left) and Gauss (right) probability plots for a 1000 cell subset of a 19266 grains structure with *cv* = 0.1.

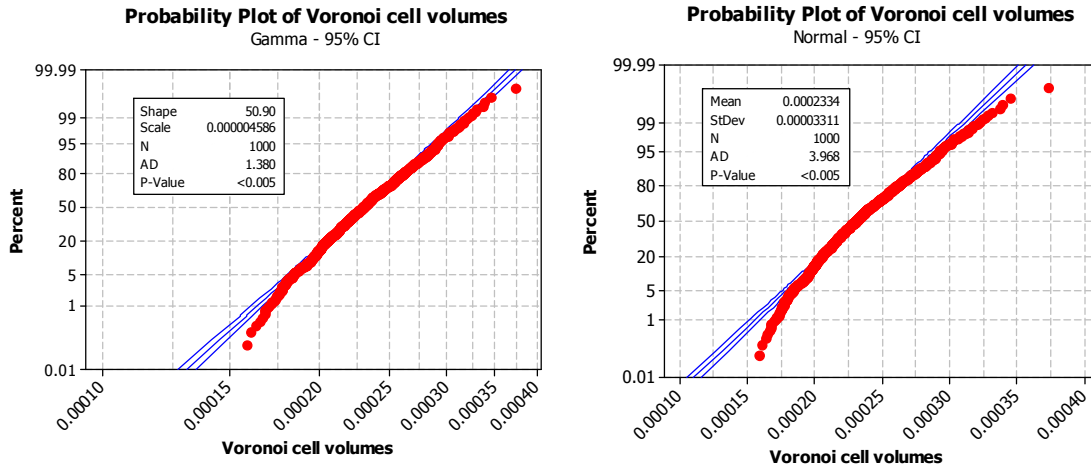The AD statistics depends nonlinearly on the size of the data set. To take this feature into account, subsets of the same size (1000 cells) have been investigated for all structures. For each structure multiple samples have been analyzed until the convergency of the mean AD value is reached (see Figure 3.17).

a) *cv* = 0.1   b) *cv* = 2.3
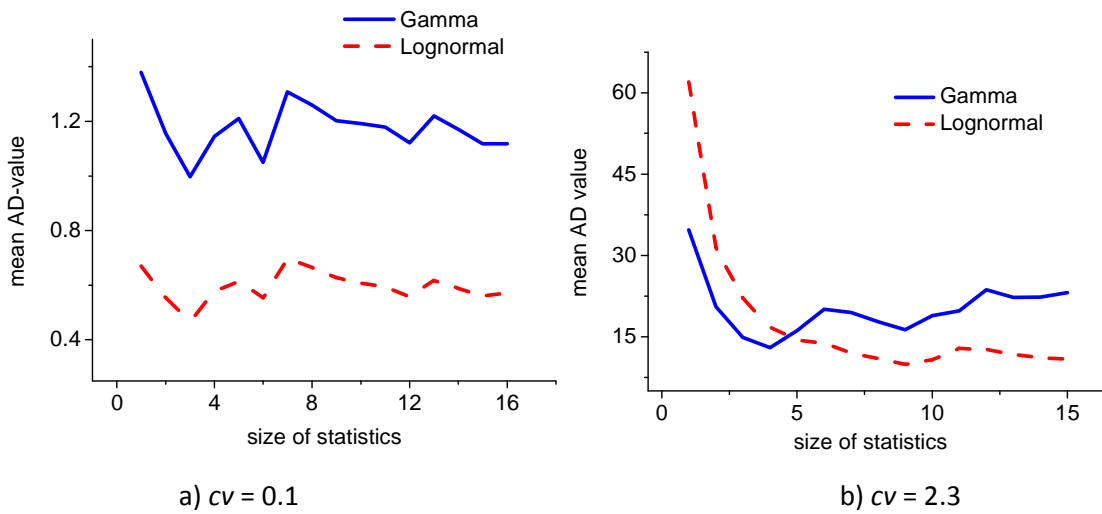
Figure 3.17: Convergency of the mean AD-values for two different structures.

In Figure 3.18 and Figure 3.19 the probability plots for the 16 075 grain structure with *cv* = 1.1 are shown. Deviations from the confidence interval are here larger than those in the case of the structure with *cv* = 0.1. For that reason the hypothesis of the lognormal distribution of the CHCV cells is here rejected. Nevertheless, the AD value of the lognormal fit is significantly smaller than that of the gamma and Gauss fits. Hence, the lognormal distribution is concluded as the best approximation. Different fit functions are compared in Figure 3.20.
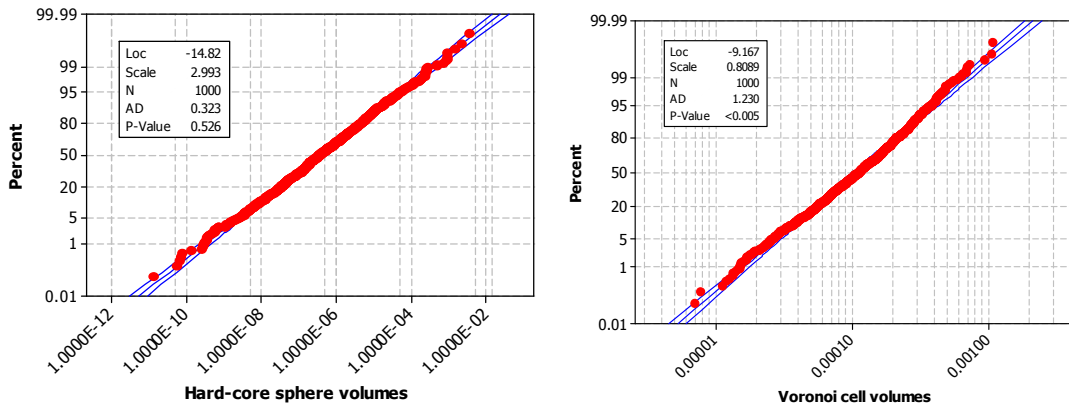
Figure 3.18: Lognormal probability plots of the CHC sphere volumes (left) and the CHCV grain volumes (right) for a subset of 1000 cells of a structure with 16 075 grains and *cv* = 1.1.
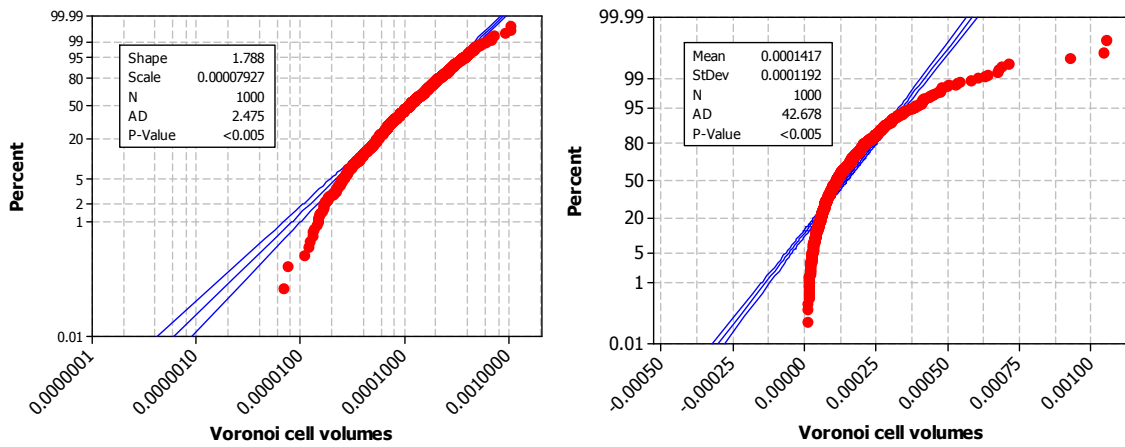
Figure 3.19: Gamma (left) and Gauss (right) probability plots for a subset of 1000 cells of a 16075 grains structure with *cv* = 1.1.
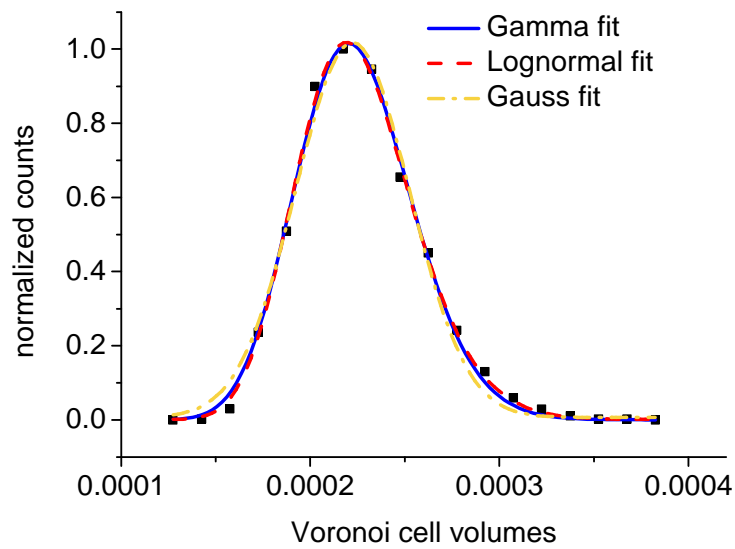
a) *cv* = 0.1
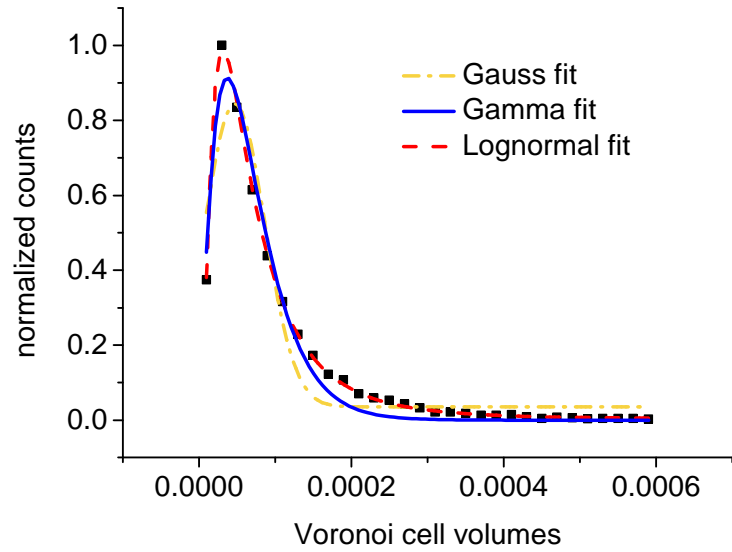
b) *cv* = 1.1
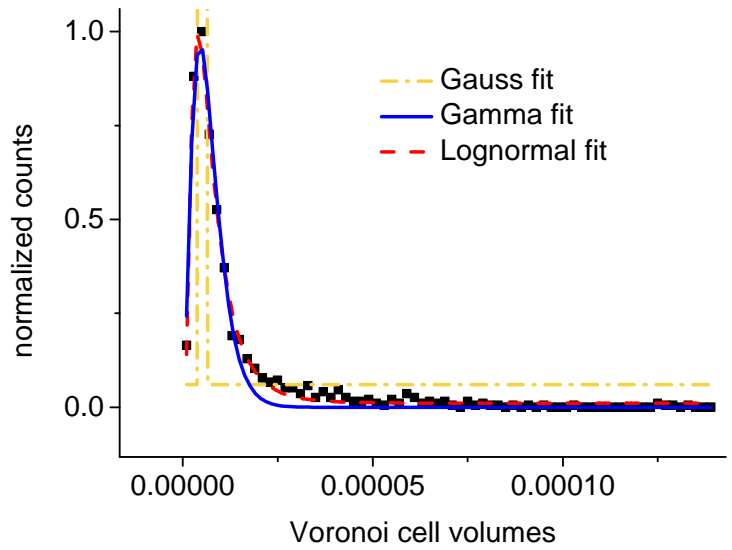
c) *cv* = 2.3

Figure 3.20: Lognormal, gamma and Gauss fits of the CHCV cells with different *cv*-values.

The mean AD values for equiaxial structures with different *cv*-values are compared in Figure 3.21. Although the lognormal and gamma distribution functions are very similar (see Figure 3.20), the AD characteristics of the lognormal fit are systematically smaller than that of the gamma assumption. Hence, it can be concluded that the developed CHCV method delivers reliable lognormal-distributed cell structures of arbitrary grain size variation. For that reason the novel CHCV method is much more suitable for a realistic modeling of the polycrystalline materials than the PV, HCV, Cluster-Voronoi and Constrained Voronoi procedures.
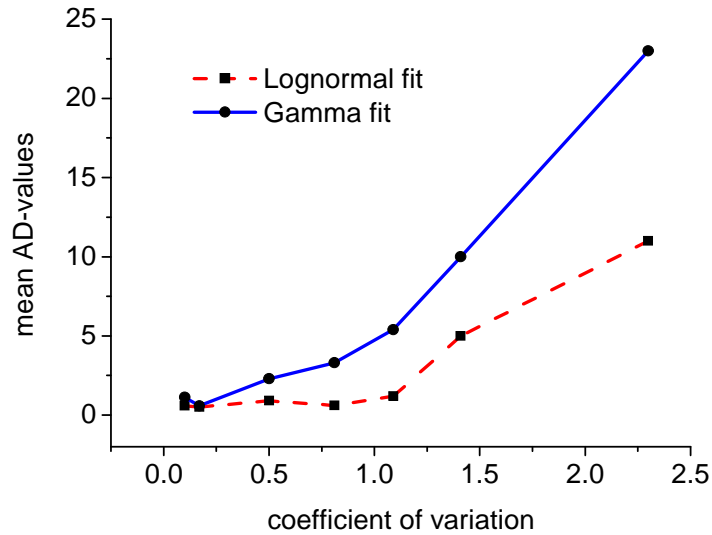
Figure 3.21: **AD-values of CHCV grain structures with different coefficients of variation.**

3.3.2 Discussion

The results shown in Figure 3.21 are similar to those obtained by Z. Fan with the LRCPS method (see Figure 3.22). The author utilized the χ^2-test instead of the Anderson-Darling test for the quantitative evaluation of fit goodness. In [Fan 2004] χ^2-values of the lognormal fit lie below the corresponding values of the gamma approximation for all *cv*-values of the closed packing of spheres[3]. However, the novel CHCV method is much less time-consuming in comparison to the LRCPS procedure. Here, the hard-core spheres are neither modeled geometrically nor rearranged by any time-consuming algorithm. Instead, in the proposed CHCV tessellation only the generating points which do not fulfill the constraining Hard-core condition are eliminated. By numerical experience this algorithm is very fast. Moreover, the simple non-weighted Voronoi tessellation is applied which is also less time-consuming than the weighted Laguerre tiling as, for instance, in the LRCPS procedure.

---

[3] One should keep in mind that the *cv*-values of the closed packing of spheres are not equal to the *cv*-values of the corresponding Laguerre cells. However, it has been shown that the correlation between the both characteristics is almost linear [Fan 2004, Redenbach 2009].
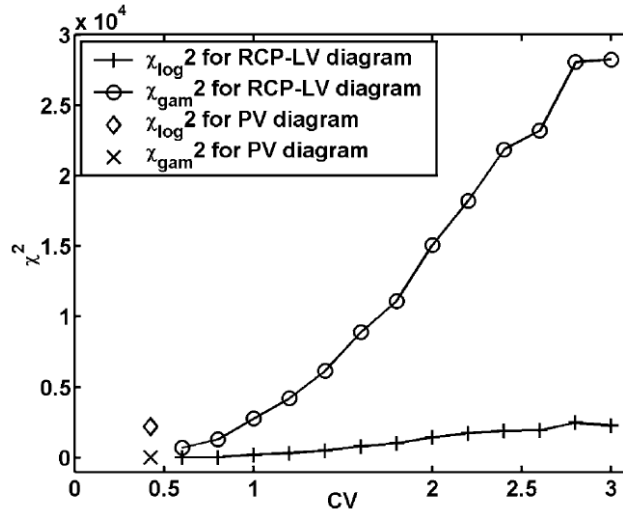
Figure 3.22: Values of the χ^2 -test statistics for the LRCPS grain structures with different coefficients of variation of the closed packing of spheres [Fan 2004].

The cell size distribution in the result of tessellation depends not only on the parameters of the distribution of the HC spheres but also on the number of the generating points before applying the constraining HC procedure. For instance, in order to produce structures with several thousand cells and *cv > 1.5* sets with more than *200 000* generating points are required. Another example concerns an adjustment of a preset distribution function with given parameters μ and σ. For the small grain ensembles (< *10 000* cells) produced from the small sets of generating points (< *200 000*) usually several realization are have to be performed until the given fit parameters are met with a small tolerance. The number of the necessary realizations can be significantly reduced by means of large grain structures (> *15 000* cells) originating from a big set of generating points (> *300 000*). Then, a correlation function between the parameters of the input

and output distributions (e.g. $\begin{pmatrix} \mu^{in} \\ \sigma^{in} \end{pmatrix} \left(\mu^{out}, \sigma^{out} \right)$) for a certain size of the set of generating

points can be determined empirically.

Because of the stochastic nature of the CHCV procedure the number of the resulting CHCV grains cannot be predicted exactly. However, with a fair tolerance it is defined by the parameters of the HC volume distribution. For instance, for small values of σ the cell number grows with descending parameter μ. Thus, a given number of cell sizes can be adjusted by several iteration steps, in which characteristics μ, σ or n (the number of generating points) are tuned.

In the introduced CHCV procedure the non-weighted Voronoi tessellation is applied. This means that the cell boundaries are located in the middle of the Delaunay bonds, although the HC spheres belonging to the same bond probably have different radii. In this manner the sizes of the small cells are overestimated and vice versa, the sizes of the big cells are underestimated. This effect, however, does not harm the lognormal grain size distribution. The Voronoi tessellations with different *cv*-values based on the lognormal distributed HC spheres fulfill the lognormal distribution function very precisely (see section 3.3.1). In contrast, in the Voronoi tilings based on the Gauss distributed HC sphere volumes the effect of the over- and underestimated cell volumes becomes considerable.

In the following we discuss, whether every type of the HC distribution function is inherited by the cell volumes or not. It will be shown, that for the Gauss and gamma distributed HC spheres it is not true. In Figure 3.23 the histograms of two different structures with Gauss distributed HC sphere volumes are presented. The probability plot of the CHC volumes (see Figure 3.24 a) shows a very good adjustment to the Gauss distribution function ($p = 0.254 \gg 0.05$). In contrast, the derived CHCV cells are not Gauss distributed. The frequency plots of the CHCV cell volumes (see Figure 3.23 a) and b) are non-symmetric. They offer less small and big cells than the Gauss fit curve predicts (see also Figure 3.24 b)). Due to the underestimation of the largest cells the number of the grains with volumes of size 0.0003 in Figure 3.23 a) and 0.0002 in case of Figure 3.23 b) exceed the corresponding Gauss fit. The best description of the structure consisting of 3230 grains is achieved with the help of the lognormal distribution function (see Figure 3.23 and Figure 3.25), whereas for the structure with 6110 grains the best fit can be reached by means of the gamma function. In case of the CHCV tilings based on the gamma distributed HC spheres either lognormal or gamma distribution are best suited. It can be assumed that the application of a weighted Voronoi tessellation (Laguerre diagram) instead of the non-weighted one, where the utilized Hard-core radii serve as weights, might minimize the described effect. The proposed modification might also broaden the range of the mean number of facets per grain which lies in the CHCV cell structures between 15.1 and 15.4.
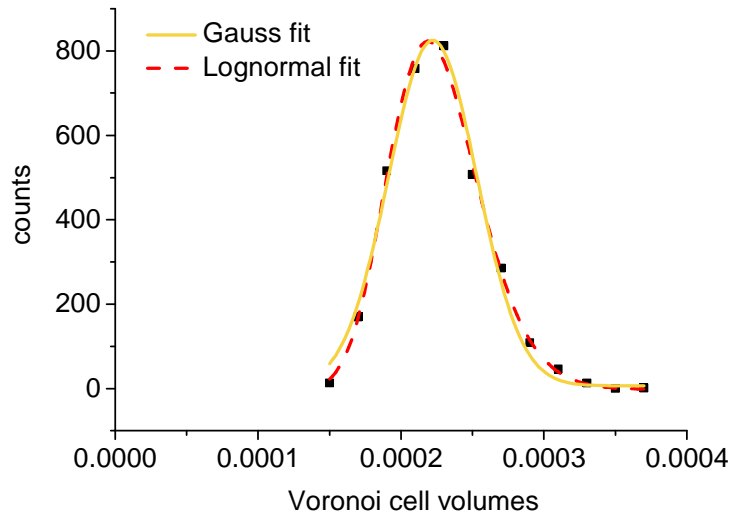
a) *cv* = 0.1; 3230 grains
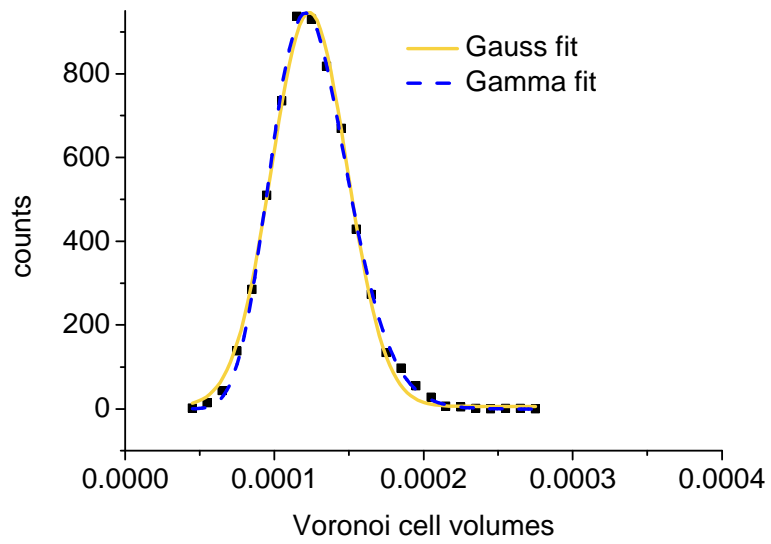
b) *cv* = 0.2; 6110 grains

Figure 3.23: Histograms of the CHCV cells for two different structures with Gauss distributed sphere volumes.
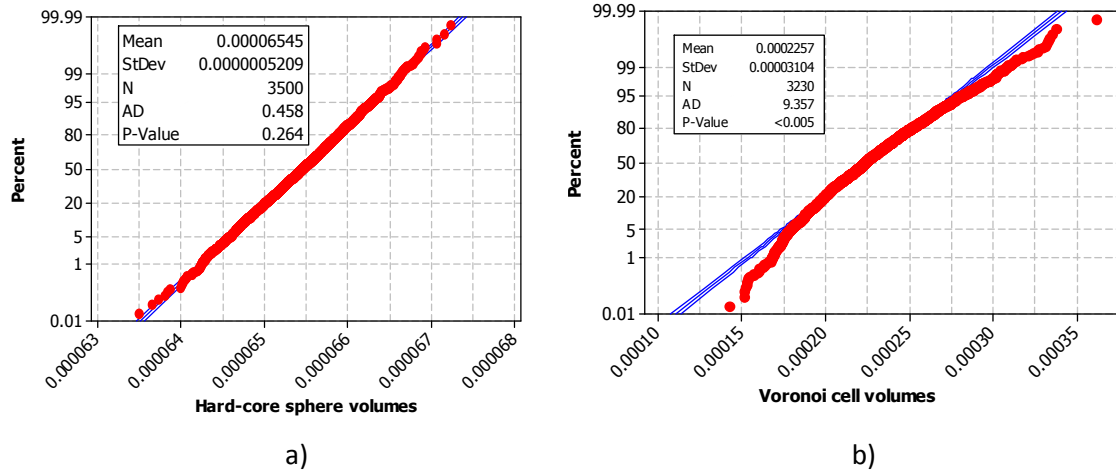
Figure 3.24: Normal probability plots: a) the Gauss distributed volumes of the CHC spheres; b) the corresponding CHCV cells.
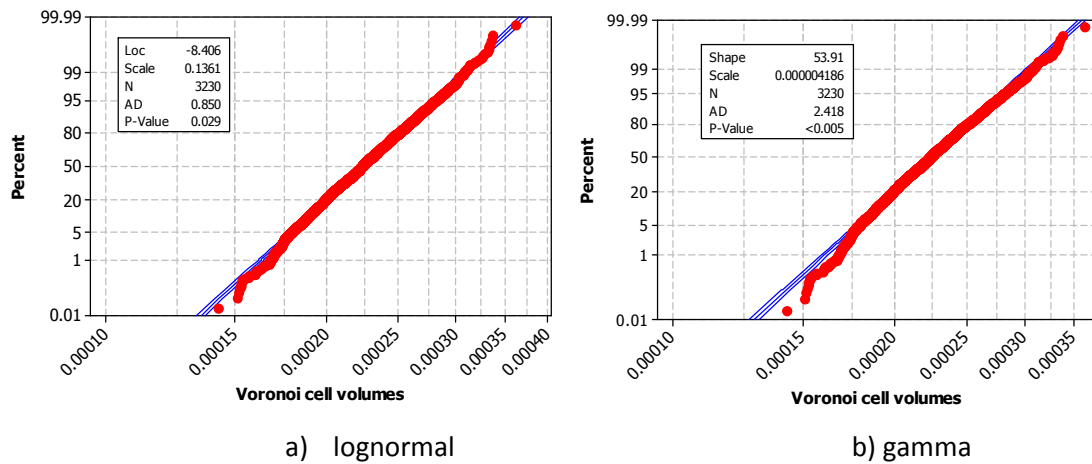
Figure 3.25: Probability plots for the volumes of the CHCV cells with Gauss distributed Hard-core sphere volumes.

All types of space tessellations discussed in sections 3.1 to 3.3 are compared in Table 3.2. It can be seen that the LRCPS and the novel CHCV methods are superior to the Poisson-Voronoi, Hard-core-Voronoi, Cluster-Voronoi and Constrained Voronoi tilings with respect to the accurate description of the real polycrystalline structures. Though, the proposed CHCV procedure is numerically much simpler and faster than the LRCPS tessellation.

Type of tiling	Globularity	Lognormal grain size distribution	cv range
Poisson-Voronoi	no	no	0.424
Hard-core-Voronoi	yes	no	0.0…0.424
Cluster-Voronoi	no	no	arbitrary
Constrained Voronoi	unknown	Comparison with gamma is missed	0.1…0.445
LRCPS	yes	yes	arbitrary
Novel CHCV	yes	yes	0.0…3.0
Real material	yes	yes	1…3 [Rhines 1982] [Nettleship 2002]

Table 3.2: Comparison of the features of different space tessellations and a real material.

3.4 Modeling of thin films

The columnar thin film models are built on the basis of a 2D CHCV tessellation (see Figure 3.26 a), which is then extruded in the direction of the cells normal ("growth direction", see Figure 3.26 b). An alternative method to produce columnar structures with the 3D Voronoi tessellation is based on the confinement of the generating points in a plane perpendicular to the orientation of the columnar structures. In that case the software producing Voronoi tessellations could fail, since the Voronoi cells are not bounded in the growth direction. One possibility to avoid the problem of the unbounded Voronoi cells is to confine generating points within a very thin slice instead of a plane. However, this procedure is significantly less efficient than the extrusion of a 2D Voronoi tessellation, since the creation of a 3D tiling is more time-consuming. Moreover, the 3D tessellation bears a higher probability for the appearance of the problem of the short edges (see section 3.8).
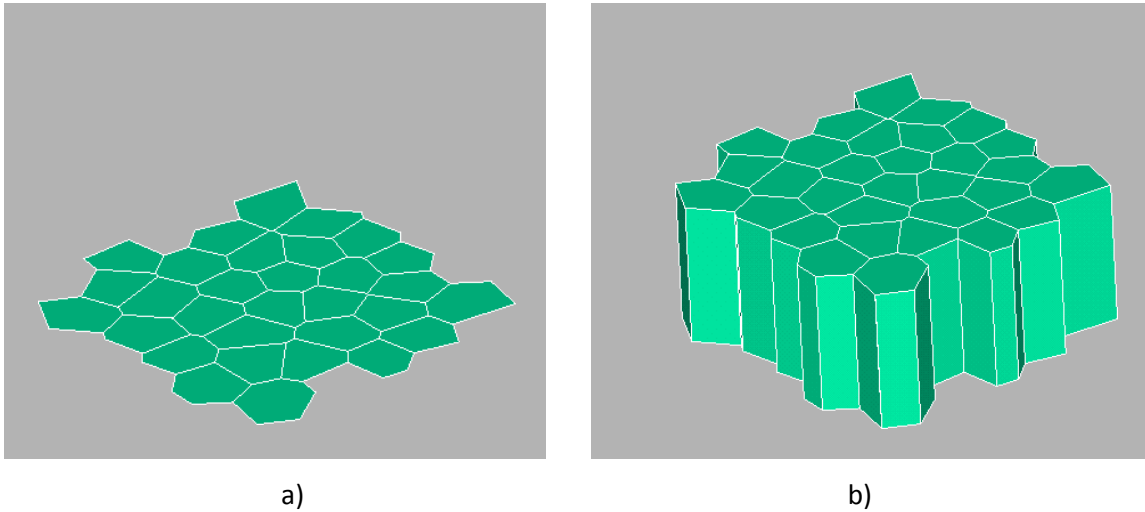
Figure 3.26: 2D Voronoi tessellation (a) and its extrusion (b).

3.5 Periodically extendable structures

In order to avoid any influence of the structural boundaries onto the microscopic and macroscopic properties in some cases it is necessary to extend the grain structure in 2 or 3 dimensions periodically (see Figure 3.27). For that purpose the set of generating points has to be periodically extended (see Figure 3.28). The CHCV tessellation is then performed in the extended point set. In order to simultaneously assure the lognormal distribution of the grain sizes and the periodic extendability of grain structures, the generating points in the extended set originating from the same point in the initial configuration (marked by the red circles in Figure 3.28) have to possess the same Hard-core radius.

a)
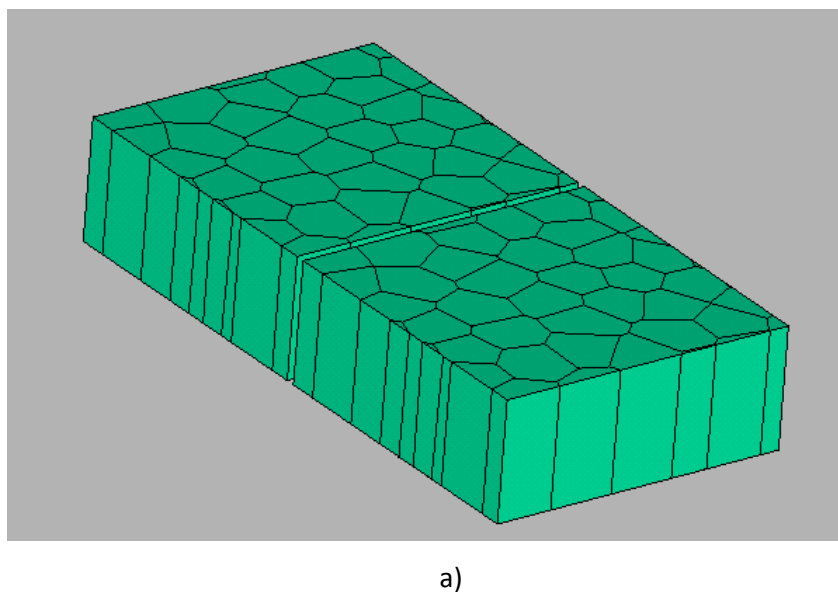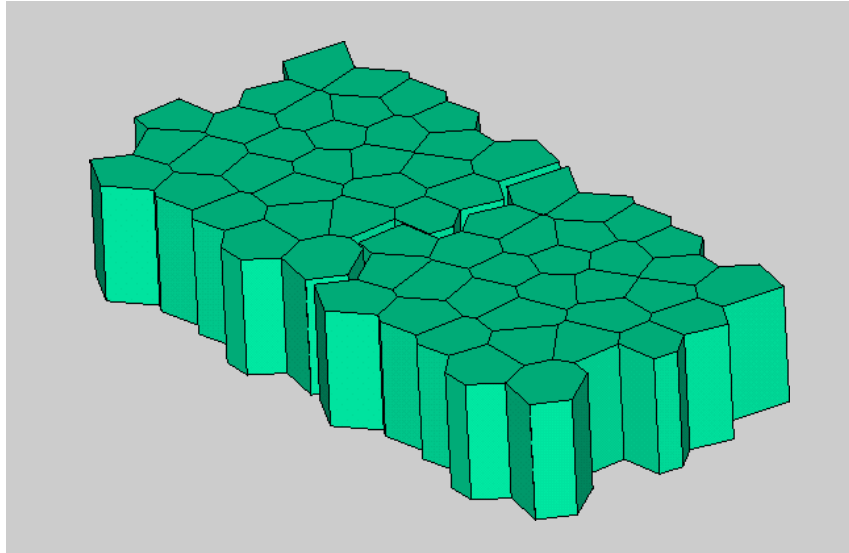
b)

Figure 3.27: Periodically extendable grain structures: a) with planar sample boundaries; b) with sample boundaries aligned with grain boundaries.
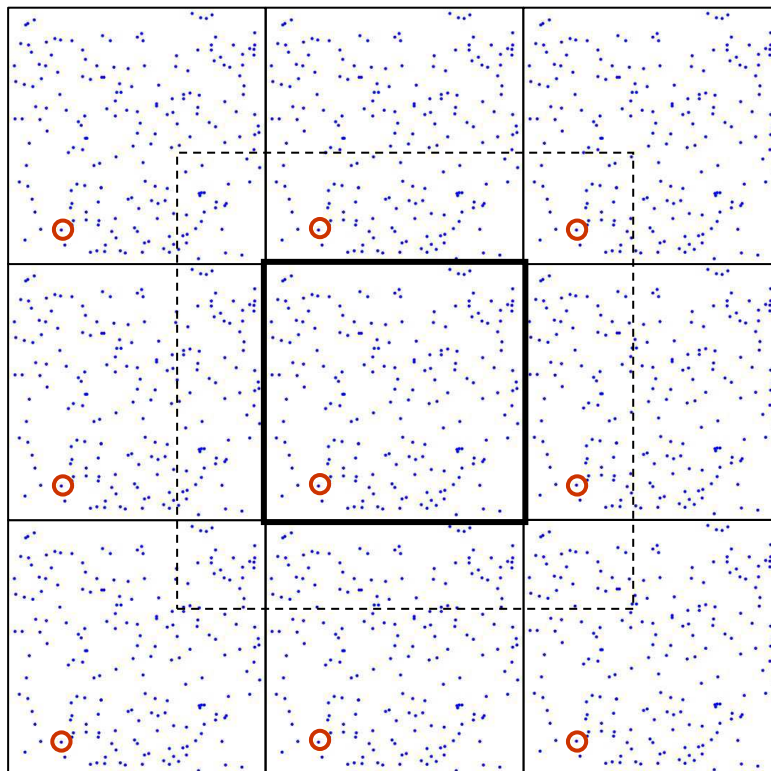
Figure 3.28: 2D-extension of the set of generating points for the construction of periodically extendable structures. To the points within the red circles the same Hard-core radius is assigned.

In case of columnar structures the extended set of generating points is $3^2=9$ times larger than the initial configuration of vertices. The point set of equiaxial bulk structures exceeds $3^3=27$

times the non-extended grain structure. For large grain ensembles this can lead to enormous calculation times. In order to minimize the computational efforts the original set of generating points can be extended only partially as shown in Figure 3.29.

$$x = x_{min} \qquad x = x_{min} + l \quad x$$
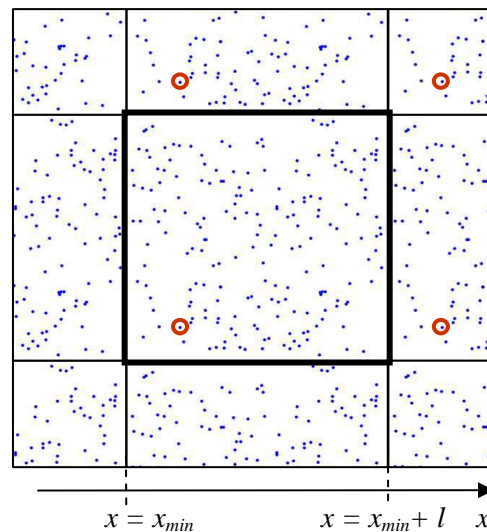
Figure 3.29: 2D-extension of the set of generating points for ensembles with a high density of generating points after performing CHC procedure.

The Constrained Hard-core procedure and the Voronoi tessellation are performed in the extended set of generating points. Subsequently, the geometry is converted into the ANSYS format. By means of ANSYS tools the structure is then cut off to the original size l.

3.6 Modeling of pores

As an approximation the pores can be modeled by a random elimination of several cells until a given porosity is achieved (see Figure 3.30). In periodically extendable grain structures with plane sample boundaries all fragments of the same grain have to be deleted (see Figure 3.31).
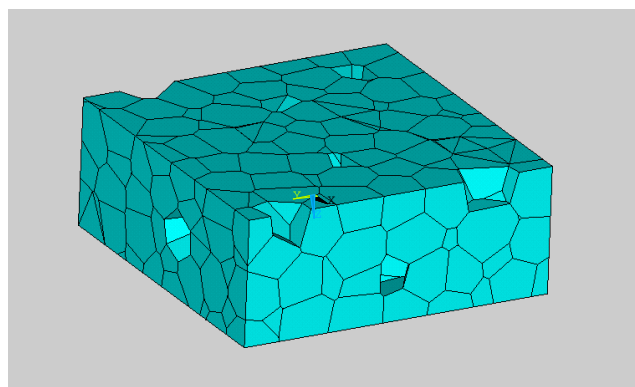
Figure 3.30: A grain model with pores.
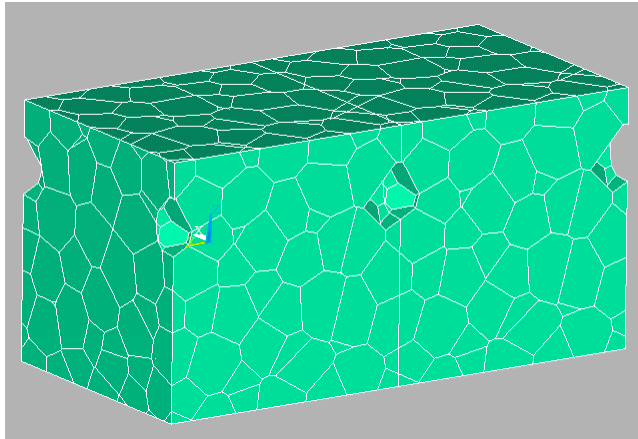
Figure 3.31: A periodically extendable grain model with pores.

3.7 Meshing of the periodically extendable grain structures

The virtual grain structures are meshed by means of the ANSYS meshing tools (see Figure 3.32). In the most common case of samples with planar boundaries and periodic grain structure the boundary grains are divided into two or more parts (see Figure 3.32 b). All parts of each split grain are assigned to the same crystal orientation and identical physical properties which is demonstrated in Figure 3.32 b by the same colors. However, the separate meshing of the split grain parts causes a larger number of finite elements than for samples with boundaries aligned with the grain boundaries (see Figure 3.32 a). In the case of the small columnar grain ensemble of Figure 3.32 (31 crystallites) the difference is about 30%. For small equiaxial structures it can be even larger, whereas in configurations with high grain numbers the difference decreases. Another advantage of the non-planar sample boundaries is a better quality of the shape of finite elements because of absence of more or less regular split grains. Despite the advantages de-scribed above it might be difficult to construct a reliable fully automated identification of the boundary surfaces for that kind of boundary structure which is necessary to assign the boundary conditions. This is an essential drawback of the grain structures with non-planar sample bounda-ries. For this reason the following analyses are exclusively concentrated on grain structures with plane boundaries as shown in Figure 3.32 b).
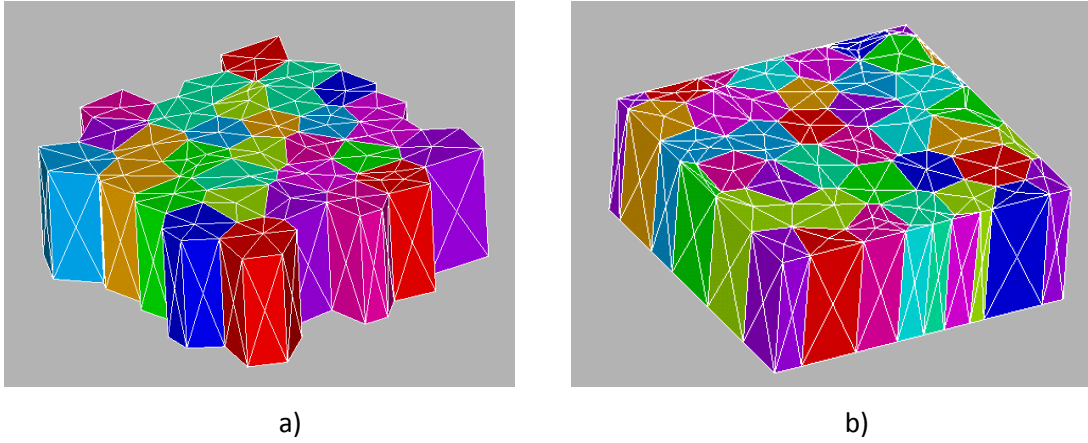
Figure 3.32: Meshed grain structures: a) with sample boundaries aligned with the grain boundaries; b) with planar sample boundaries.

In the present work generation of periodically extendable meshes has been fully automated by means of the ANSYS script language APDL. In the following, the corresponding algorithm is briefly described. In the first stage, three non-collinear sample edges are meshed. The resulting one-dimensional finite elements are then copied to the corresponding three parallel edges of each of three flanks. Subsequently three non-coplanar boundary surfaces are meshed with respect to all edges already meshed. The produced 2D finite elements are then copied to the opposite boundary surfaces. Finally, the cell volumes are meshed with respect to the periodic surface finite elements.

3.8 Numerical problems in large tilings and proposed solutions

For statistical reasons the cells of the Voronoi tessellation sometimes have extremely short edges. When the relation of the shortest edge to the longest edge $\dfrac{l_{\min}}{l_{\max}}$ of the Voronoi cells goes bellow a critical value (typically $\dfrac{1}{100}$ or $\dfrac{1}{500}$) the structure can not be meshed or a mesh would result in ill conditioning of the finite element matrices. A recent study [Fröhlich 2001] has shown that the probability of $\dfrac{l_{\min}}{l_{\max}} \geq \dfrac{1}{100}$ in a 2D Voronoi tessellation with 200 cells is less than 0.4%. This means that on average not even every hundredth grain structure can be meshed without any complication. This result will be even more dramatic in case of 3D tessellations since the number of edges of 3D tessellation cells is about two times larger than the number of edges in 2D cells.

In the framework of the freeware PyXL[4] [PyXL] C. Myers proposed an algorithm, which acciden-tally displaces generating points until a given $\dfrac{l_{min}}{l_{max}}$ ratio is exceeded. However, as follows from the results of A. Fröhlich [Fröhlich 2001] the algorithm proposed by C. Myers might take a very long time for large structures (>200 grains) until convergence is reached. Moreover, because of the accidental displacements of generating points the resulting structures might not be able to render the desired size distribution function. Hence, a more efficient and reliable method for elimination of the short edges is required.

Besides the short edges, which originate from the Voronoi tessellation itself, the short edges resulting from the sample cutting procedure (see Figure 3.33) might retard the meshing process. In the present work two merging schemes were utilized in order to eliminate the short edges at the sample boundaries as well as in the interior of the sample.
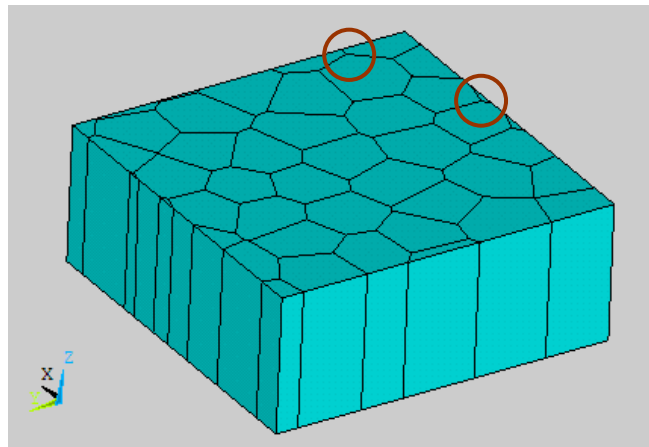
Figure 3.33: Short edges originating from the plane sample cut.

One of the merging procedures has been proper developed and integrated into our software converting space tessellations from the PyXL-format to the ANSYS-format, since structures with a large number of grains (>500) often could not be read (and consequently could not be merged and meshed) in ANSYS. In the first step the algorithm identifies cell vertices whose distances to a certain vertex lie below some critical value r_m, which is called merging radius. In the following these sets of cell corners with mutual low distances are called groups of critical points. In order to preserve periodic boundary geometry, in each group of critical points the so-called *master point* is identified. The *master point* always remains in the structure. For the identification of the *master vertex* the so-called *boundary level bl* is essential. We assign zero boundary level *bl=0* to

---

[4] The tool was utilized in the present work for generation of Voronoi tessellations.

the points, which do not belong to the sample outer surfaces. The vertices belonging to the sample surfaces but not to the edges obtain $bl=1$. The points belonging to the model edges but not to the model corners are assigned with $bl=2$. The *master vertex* is required to have the highest bl-value in the group of critical points. Other critical points in the group are eliminated. We call these vertices *victim points.* The striking fact is that the eliminated vertices belonged to edges and facets of several grains. In the whole topological setup of the structure they have to be replaced by the non-eliminated points. This is, however, a challenging task since the planarity of several areas might be distorted or some edges, areas and volumes have to be additionally eliminated. An example is treated in the following paragraph.

In Figure 3.34 a) four facets of a Voronoi cell are presented. A group of critical points contains only two vertices. The *victim point* has to be deleted and substituted by the *master point* in the facets A, B and C. The *master vertex* lies in the plane of the areas A and B. Therefore, the *victim point* can be substituted by the *master* without difficulty for these facets. The *master vertex*, however, does not belong to the area C and, hence, it cannot easily replace the *victim* (see Figure 3.34 b). In such common case our algorithm provides a supplementary triangle, which contains the neighbor points of the *victim* and the *master vertex* (see Figure 3.34 c).
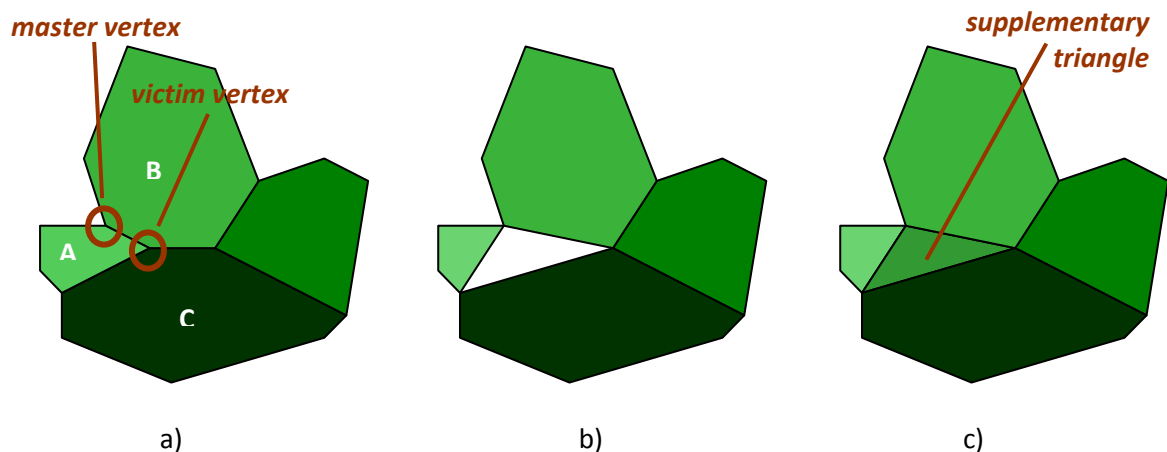
Figure 3.34: **Several facets of a Voronoi cell; an example of the merging procedure: a) identification of the master and victim vertices; b) victim vertex is eliminated; c) supplementary triangle is added.**

As the merging distance r_m becomes larger the number of critical points per group of critical points grows. In the case of the structure from Figure 3.35 a) two victim points have to be eliminated. As a consequence of this action the facet A has to be deleted (see Figure 3.35 b). In other, more complicated configurations several facets or even volumes have to be deleted and the resulting gaps have to be artfully corrected by the supplementary triangles. It is a challenging

task to develop an algorithm considering all possible complicated special cases of the geometrical constellations. Therefore even commercial software packages like ANSYS and Sinterdict [Sinterdict] sometimes exhibit algorithmic problems in merging and meshing procedures.
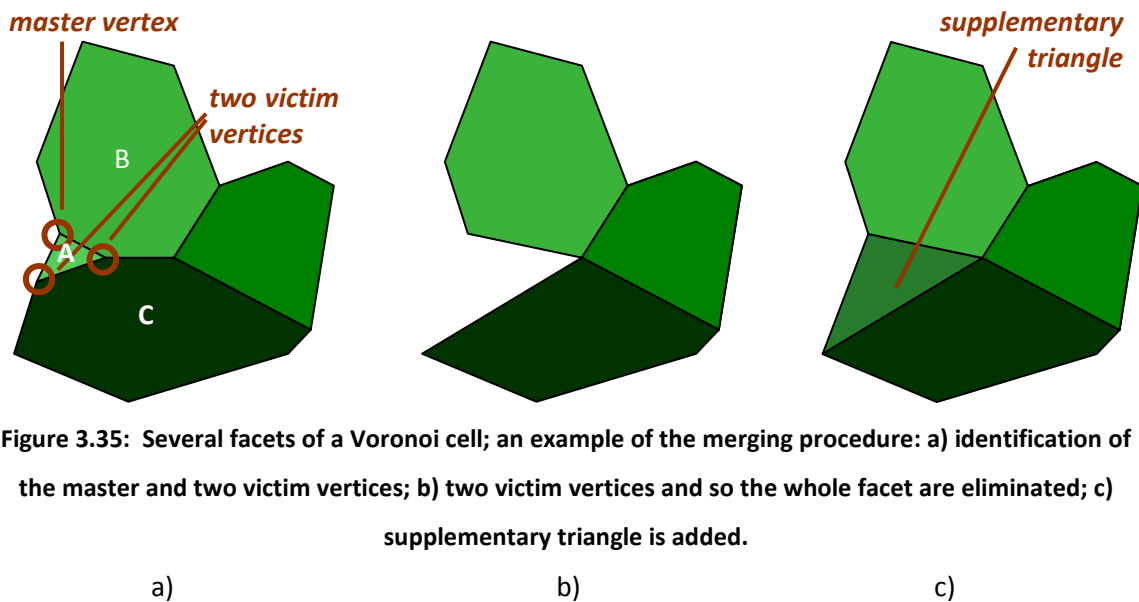
Figure 3.35: Several facets of a Voronoi cell; an example of the merging procedure: a) identification of the master and two victim vertices; b) two victim vertices and so the whole facet are eliminated; c) supplementary triangle is added.

a)   b)   c)

The developed merging procedure is specified for $r_m \leq 0.0005 \cdot l$, where l is the length of the largest sample edge. In the case $r_m > 0.0005 \cdot l$ the algorithm occasionally fails. For this reason a second merging procedure based on the ANSYS macro NUMMRG has been additionally used. In the output of the NUMMRG command only the vertex point with the lowest number from every group of critical points remains in the structure. In order to preserve the boundary geometry, a renumbering algorithm has been implemented in the ANSYS-APDL macro language. This algorithm assigns ascending numbers to the vertices with decreasing *bl* value and updates corresponding topological relations. Then, a subsequent execution of the NUMMRG macro does not affect the boundary geometry.

The NUMMRG command rectifies in many cases correctly the topological drawback of eliminated points and edges. However, casually this merging algorithm fails as well. As a consequence problems with the meshing procedure arise. The variation of the critical merging distance r_m often helps in the described situations. The use of too small merging radii

($r_m \leq 0.0005 \cdot l$), however, should be avoided, since the quality of the finite elements gets worse.

The described procedure for generation of periodically extendable grain structures and FE-meshes developed in the present work was extensively tested for 3D grain ensembles up to 1000 cells. Although a universal merging algorithm is still an unsolved problem, 90 % - 95 % of produced models were periodically meshable by our fully automated procedure. This result constitutes a great improvement comparably to the procedure proposed in [Fröhlich 2001], where less than 0.4% of 2D Voronoi mosaics with 200 cells could be meshed by finite elements.

The implemented merging procedures are important not only for the purpose of FE-meshing but also for the quality and number of finite elements. The FE-meshes produced with and without developed merging algorithms are compared in Figure 3.36. The latter structure offers smaller and less regularly formed elements than the model created using the developed merging procedures. In mosaics, where the short edges are eliminated, the meshing with larger element sizes is possible and thus, the number of finite elements can be reduced down to 50%.

a)   b)
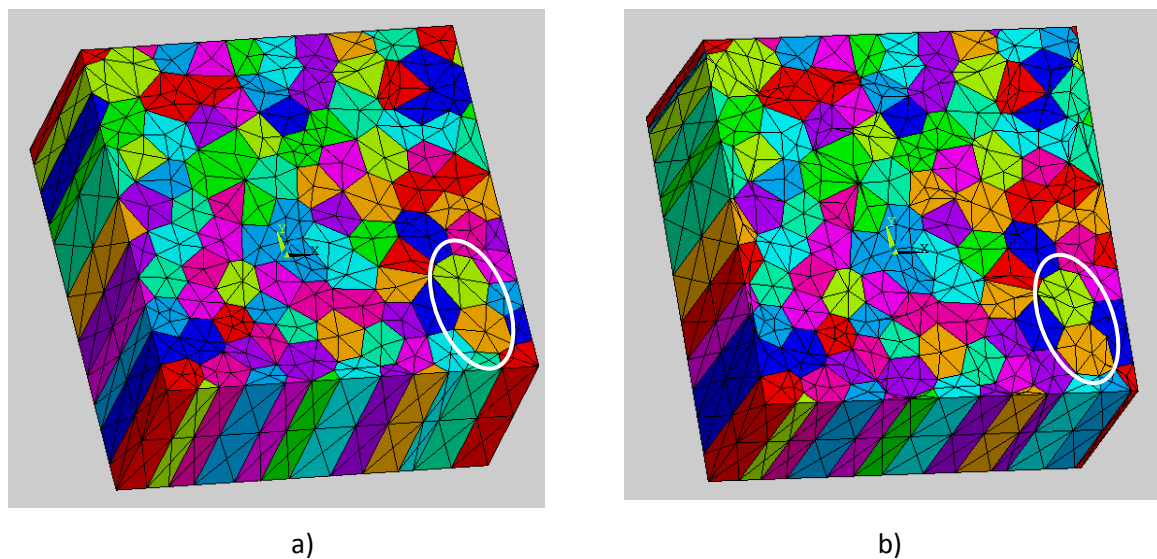
Figure 3.36: Periodic extendable meshed grain structures: a) produced with application of developed merging algorithms; b) produced without application of developed merging algorithms.

Because of the accidental location of the sample boundary within the boundary grains a conjecture could arise that some of grain fragments can become indefinitely sharp and small ($d, \varphi \rightarrow 0$, see Figure 3.37). This fact might be critical for the reliable numerical handling and meshing of the boundary grains. However, this scenario is impossible because of the finite merg-

ing radius and finite grain size. In the last part of the present section a mathematical proof is provided for the existence of a lower bound for the values d and φ (see Figure 3.37), which are critical for the reliable FE-meshing.
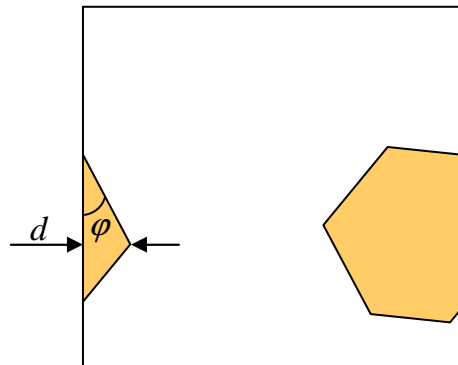
Figure 3.37: Critical fragment (splinter) of the boundary grain.

Claim:

Let V be a Constrained Hard-core Voronoi tessellation of the metric space $\mathbb{R}^3$ with lognormal distribution of hard-core volumes $V_{HC} \in \mathbb{R}$ according to (3.8), merging radius $r_m \in \mathbb{R}$, $r_m > 0$ and density of generating points λ. Then a lower bound for the values d and φ exists.

Proof:

In Figure 3.38 the critical splinter of a boundary grain (yellow), the corresponding Delaunay triangle (dashed black lines) and the circumcircle of the triangle together with circle radii (doted blue lines) are presented. The idea of the proof is as follows: in order that the parameters d and φ become infinitesimal small, the chord length of a Poisson cell c has to be infinitely large or the merging radius r_m - infinitesimal small; both requirements can be, however, neglected due to the finite density of generating points λ and finite merging radius r_m as preconditions of the claim. In following, an estimation procedure for the lower bounds $d_{\min}$ and $\varphi_{\min}$ is given.
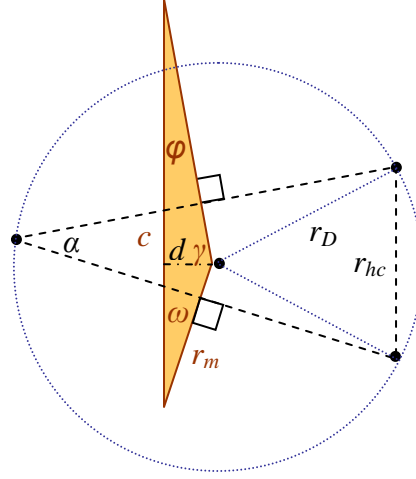
Figure 3.38: Critical splinter of a boundary grain (solid red lines), corresponding Delaunay triangle (dashed black lines) and its circumcircle (dotted blue line).

The probability distribution function (pdf) for the Delaunay circumcircle of radius r_D was derived by R. Miles [Miles 1970] and J. Møller [Møller 1996], [Cowan 2007]:

$$f(r_D) = 2\pi^2 \lambda^2 \frac{r_D^3}{e^{\pi \lambda r_D^2}} .$$ (3.11)

With $t_D \in [10^{-6}, 10^{-8}]$ - the probability that $r_D > r_{D,\max}$ exists - the upper bound $r_{D,\max}$ can be estimated from

$$\int_0^{r_{D,\max}} f(r_D) dr_D = 1 - t_D ,$$

$$\frac{1 + \pi \lambda r_{D,\max}^2}{e^{\pi \lambda r_{D,\max}^2}} = t_D .$$ (3.12)

The latter calculation was performed by means of partial integration.

With $t_{HC} \in [10^{-6}, 10^{-8}]$ - the probability that the hard-core distance $r_{HC} < r_{HC,\min}$ exists - the lower bound $r_{HC,\min}$ can be estimated from

$$\int_0^{r_{HC,\min}} f(r_{HC}) dr_{HC} = t_{HC} .$$ (3.13)

From the law of cosines and the relations of angles within a circle the lower bound for the angle α (see Figure 3.38) equals:

$$\alpha_{\min} = \frac{1}{2} \arccos\left(1 - \frac{r_{HC,\min}^2}{2 r_{D,\max}^2}\right) .$$ (3.14)

According to [Muche 1992] the pdf for the PV chord length reads

$$f(c) = 1 - \frac{6^{1/3} \pi^{2/3} \lambda^{5/3}}{\Gamma(\frac{5}{3})} \int_0^\infty \int_0^\pi \rho^2 \sin\alpha \frac{\partial v_3(\alpha,\rho,c)}{\partial c} e^{-\lambda v_3(\alpha,\rho,c)} d\alpha d\rho \qquad (3.15)$$

with

$$v_3(\alpha,\rho,c) = \sqrt{2}\pi\rho \sin\alpha \times$$

$$\times \frac{\frac{2}{3}\rho^2 \cos^2\alpha\left(4c^2+\rho^2\right) + \rho c \cos\alpha\left(\frac{13}{6}\rho^2 + \frac{17}{6}c^2\right) + \left(\frac{2}{3}\rho^2+c^2\right)\left(c^2+\rho^2\sin^2\alpha\right)}{\sqrt{\rho^2+2\rho c\cos\alpha+c^2}\sqrt{\sqrt{\left(\rho^2+c^2\right)^2-\left(2\rho c\cos\alpha\right)^2}+c^2+\rho^2\left(\sin^2\alpha-\cos^2\alpha\right)}} +$$

$$+\sqrt{2}\pi\rho \sin\alpha \frac{\frac{2}{3}\rho^2 \cos^2\alpha\left(4c^2+\rho^2\right) + \rho c \cos\alpha\left(\frac{13}{6}\rho^2 + \frac{17}{6}c^2\right) + \left(\frac{2}{3}\rho^2+c^2\right)\left(c^2+\rho^2\sin^2\alpha\right)}{\sqrt{\rho^2-2\rho c\cos\alpha+c^2}\sqrt{\sqrt{\left(\rho^2+c^2\right)^2-\left(2\rho c\cos\alpha\right)^2}+c^2+\rho^2\left(\sin^2\alpha-\cos^2\alpha\right)}} +$$

$$2\pi c\left(\rho^2 + \frac{1}{2}\rho^2\cos^2\alpha + c^2\right)\left(\pi - \arctan\frac{\rho\sin\alpha + \frac{1}{\sqrt{2}}\sqrt{\sqrt{\left(\rho^2-c^2\right)^2+\left(2\rho c\cos\alpha\right)^2}-\left|c^2-\rho^2\right|}}{r + \frac{1}{\sqrt{2}}\sqrt{\sqrt{\left(\rho^2-c^2\right)^2+\left(2\rho c\cos\alpha\right)^2}-\left|c^2-\rho^2\right|}}\right)$$

With $t_c \in [10^{-6},10^{-8}]$ - the probability that a cell chord with length $c > c_{\max}$ exists - the upper

bound $c_{\max}$ can be estimated from

$$\int_0^{c_{\max}} f(c)dc = 1 - t_c . \qquad (3.16)$$

From the sine law for the grain fragment triangle (solid red line in Figure 3.38) follows:

$$\varphi = \arcsin\left(\frac{r_m}{c}\sin\gamma\right) = \arcsin\left(\frac{r_m}{c}\sin(\pi-\alpha)\right).$$

Consequently, the lower bound for $\varphi_{\min}$ exists:

$$\varphi_{\min} = \arcsin\left(\frac{r_m}{c_{\max}}\sin(\pi-\alpha_{\min})\right),$$

$$\varphi_{\min} = \arcsin\left(\frac{r_m}{c_{\max}}\sin\left(\pi - \frac{1}{2}\arccos\left(1 - \frac{r_{HC,\min}^2}{2r_{D,\max}^2}\right)\right)\right). \qquad (3.17)$$

Consistent,

$$d_{\min} = r_m \sin\omega = r_m \sin(\alpha_{\min} - \varphi_{\min}). \qquad (3.18)$$

3.9   Summary: grain and mesh generator

Figure 3.39 gives an overview for the procedure of grain and FE-mesh generation developed in the present work. The green highlighted methods are proper implementations either in C++ or in ANSYS®-APLD macro language. Important progresses have been achieved in the field of efficient generation of periodically extendable grain structures with lognormal distribution of volumes and diameters as well as in the area of reliable meshability of the space tessellations.
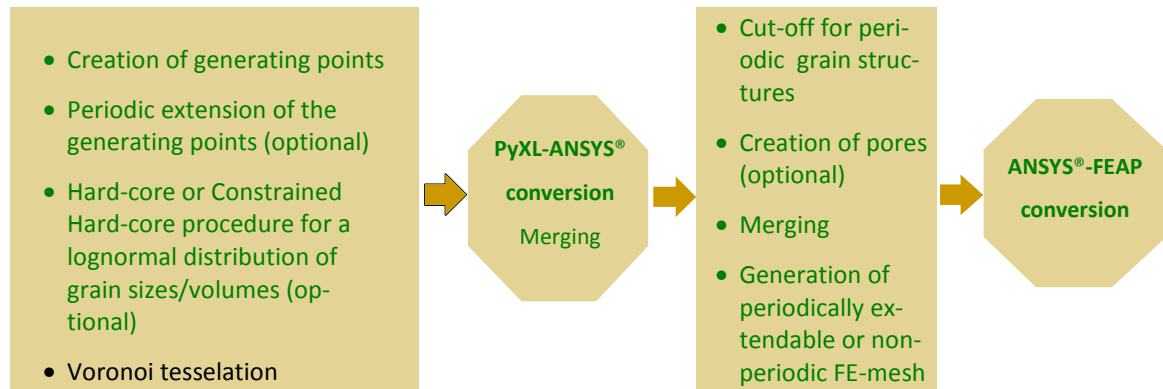
Figure 3.39: **Scheme of the developed procedure for grain and mesh generation: green font symbolizes methods, which were partially or completely implemented within the present work.**

The resulting FE-meshes were either directly utilized for the linear piezoelectric studies within the ANSYS® package or converted into FEAP format for the non-linear Huber-Fleck calculations. The basics of these physical models for ferroelectric materials are described in the next chapter.

4 Physical modeling of the ferroelectric materials

In the present chapter several physical models of the ferroelectric materials, which act on different scales, will be introduced. On the scale of electrons and atomic nuclei quantum mechanical Density Functional Theory (DFT) is an effective tool for computation of miscellaneous properties of ferroelectrics. It is briefly described in the first section of the chapter. The DFT approach is, however, too time-consuming for systems with more than 200 atoms. Therefore, for studies of structural defects or crack propagation in larger systems classical atomistic calculations are usually utilized. The empirical shell-model, which is described in the second section of the present chapter, is one of the classical atomistic approaches. Fitted to the data obtained in DFT-calculations it was shown to be capable to reproduce intrinsic features and domain wall properties of PTO [Sepliarsky 2005, Shimada 2008]. The DFT and shell-model simulations in the project COMFEM were performed at the Fraunhofer Institut für Werkstoffmechanik (Freiburg, Germany) by P. Marton and C. Elsässer. On the meso-scale of several hundred nanometers the phase-field modeling is a good choice to describe the evolution of ferroelectric domains [Völker 2010]. In order to give a knowledge based description of ferroelectric material a linkage between DFT, shell-model and phase-field theories was developed within the scope of the BMBF-project COMFEM [Völker 2010]. As will be demonstrated in the present chapter, the developed multi-scale scheme is a powerful tool for calculation of necessary input data for further micromechanical simulations of PTO and PZT. The phase-field model and its coupling to the DFT and atomistic simulations are outlined in the third section.

In the fourth section available results on effective macroscopic material properties in thin films and bulk BTO and PTO are summarized. The described numerical results depend on the misorientation or on the texture angle. The models utilized up to now to describe the macroscopic properties of BTO and PTO ferroelectrica are not able to predict the polarization configuration, remanent polarization and, hence, the effective piezoelectric and dielectric material constants at remanence. Moreover, the ferroelectric hysteresis of BTO and PTO ceramics could not been determined theoretically. In order to bridge this gap we use the recently published model of Huber and Fleck, described in the fifth section of the chapter, for our micromechanical calculations. Another drawback of the theoretical investigations performed so far is use of experimental single-crystal constants. Such a procedure is, however, ineffective or even misleading for design of new materials with unknown parameters. Moreover, even for some known ceramics, e.g. PZT, experimental data on single-crystal constants are not available and so no theoretical

results for this material from a micromechanical model exist. For these reasons in the last section of the chapter we propose different possibilities of bridging of micromechanical Huber-Fleck calculations with DFT, shell-model and phase-field single-crystal data. The elaboration of such a multi-scale simulation chain (see Figure 4.1), which has been defined as the goal of the COMFEM project, is the main topic of the present thesis and, as it will be shown below, can provide an effective theoretical tool for the modeling of materials free of experimental input parameters. The results of the multi-scale simulations and comparison with experimentally measured properties are presented and discussed in the next chapter.

nano-scale   meso-scale   micro-scale

DFT, shell-model   phase-field method   micromechanics
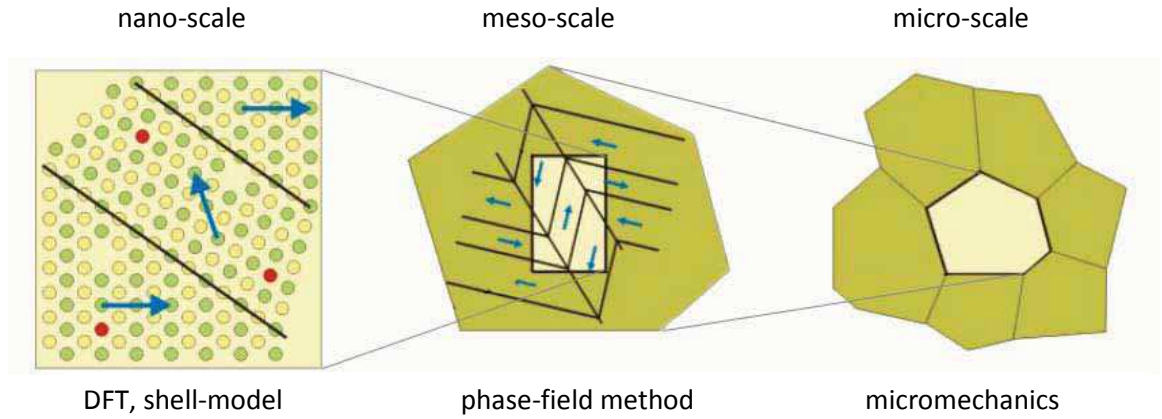
Figure 4.1: Multi-scale simulation chain for ferroelectrics implemented in the scope of the BMBF-project COMFEM.

4.1 DFT calculations

Knowledge of the total ground state energy of a system consisting of electrons and atomic nuclei E_0 allows to estimate various material properties like lattice constants [Vedmedenko 2007], elastic [Panda 2006] and piezoelectric [Saghi 1999] tensors, lattice dynamics [Ghosez 1999], deformation mechanisms [Vedmedenko 2008], etc. According to [Panda 2006], the total energy of a crystal E_0 under strain S_{ij} can be expressed in terms of the Taylor's series as

$$E_0(V) = E_0(V_0) + V_0 \sum_{i,j=1}^{3} T_{ij} S_{ij} + \frac{V_0}{2!} \sum_{i,j,k,l=1}^{3} \hat{c}_{ijkl} S_{ij} S_{kl} + \dots \quad (4.1)$$

Here, V_0 is the volume of the unstrained crystal, $E_0(V_0)$ - the total energy of the unstrained crystal, T_{ij} are the elements of the stress tensor and $\hat{c}_{ijkl}$ - components of the elastic tensor. Hence, the elastic constants can be obtained as a curvature of the energy-strain function:

$$\hat{c}_{ijkl} = \frac{\partial^2 E_0}{\partial S_{ij} \partial S_{kl}}. \quad (4.2)$$

In a similar way the piezoelectric coefficients e_{ijk} can be calculated from polarization differences as a function of strain:

$$\hat{e}_{ijk} = \frac{\partial P_i}{\partial S_{jk}}.$$ (4.3)

The polarization can be estimated using

$$P = \frac{1}{V}\left(\sum_{\alpha=1}^{N_N} Z_\alpha \boldsymbol{R}_\alpha + e \int_V n_0(\boldsymbol{r})\boldsymbol{r}d^3r\right).$$ (4.4)

Hereby N_N is the number of the nuclei in the system, $\boldsymbol{R}_\alpha$ and Z_α ($\alpha = 1...N_N$) the positions and charges of the nuclei, n_0 the ground state electron density and e electron charge.

The equilibrium domain wall thickness is typically identified with that corresponding to the configuration possessing minimal total ground state energy among all investigated systems with different domain wall thicknesses.

Determination of the ground state density and the total energy of an electronic system is, however, a challenging task. On this scale a quantum mechanical treatment is required. In general, the non-relativistic time-independent Schrödinger equation for N_N nuclei and N_e electrons has to be solved:

$$\left(-\sum_{\alpha=1}^{N_N}\frac{\hbar^2}{2M_\alpha}\Delta_{\boldsymbol{R}_\alpha} - \sum_{i=1}^{N_e}\frac{\hbar^2}{2m_e}\Delta_{r_i} + e^2\sum_{\alpha=1}^{N_N}\sum_{\beta>\alpha}^{N_N}\frac{Z_\alpha Z_\beta}{|\boldsymbol{R}_\alpha - \boldsymbol{R}_\beta|} - e^2\sum_{\alpha=1}^{N_N}\sum_{i=1}^{N_e}\frac{Z_\alpha}{|\boldsymbol{R}_\alpha - \boldsymbol{r}_i|} +\right.$$

$$\left.+e^2\sum_{i=1}^{N_e}\sum_{j=1}^{N_e}\frac{1}{|\boldsymbol{r}_i - \boldsymbol{r}_j|}\right)\Psi\left(\boldsymbol{R}_1,...,\boldsymbol{R}_{N_N},\boldsymbol{r}_1,...,\boldsymbol{r}_{N_e}\right) = E_0 \cdot \Psi\left(\boldsymbol{R}_1,...,\boldsymbol{R}_{N_N},\boldsymbol{r}_1,...,\boldsymbol{r}_{N_e}\right).$$ (4.5)

Hereby $\Psi\left(\boldsymbol{R}_1,...,\boldsymbol{R}_{N_N},\boldsymbol{r}_1,...,\boldsymbol{r}_{N_e}\right)$ is a many-particle wave function, m_e - the mass of an electron, M_α - the masses of the nuclei, $\Delta_{\boldsymbol{R}_\alpha}$ - the Laplace operator regarding variables $\boldsymbol{R}_\alpha$, Δ_{r_i} - the Laplace operator regarding variables $\boldsymbol{r}_i$ and $\hbar$ - the reduced Planck constant. An analytical solution of this differential equation is available only for some selected cases, such as hydrogen atom with one proton and one electron or helium ion with two protons, two neutrons and one electron. A numerical treatment of the many-particle problem (4.5) is possible for systems with less than 10 atoms only.

Density functional theory (DFT) is a computational quantum mechanical approach, which is able to predict the total ground state energy E_0 for systems consisting of electrons and atomic nuclei up to several hundred atoms:

$$E_0(\boldsymbol{R}_\alpha) = \sum_{\alpha=1}^{N_N} \sum_{\beta>\alpha}^{N_N} \frac{Z_\alpha Z_\beta}{|\boldsymbol{R}_\alpha - \boldsymbol{R}_\beta|} + E_0^{el}(\boldsymbol{R}_\alpha). \tag{4.6}$$

$E_0^{el}(\boldsymbol{R}_\alpha)$ is the ground state energy of an electronic system in presence of nuclei. According to the theorems of Hohenberg and Kohn [Hohenberg 1964] E_0^{el} is a unique functional of the ground state electron density n_0:

$$E_0^{el} = E^{el}[n_0]. \tag{4.7}$$

The functional consists of several terms like kinetic, Hartree, exchange and correlation energies, for details see [Vedmedenko 2007] or [Elsässer 1990]. Using the theorems of Hohenberg and Kohn the Schrödinger equation (4.5) containing many-particle wave function can be divided into N_e differential equations with one-particle wave functions $\phi_i(\boldsymbol{r})$:

$$\left(-\frac{\hbar^2}{2m_e}\Delta + V_{eff}\right)\phi_i(\boldsymbol{r}) = \varepsilon_i \phi_i(\boldsymbol{r}), \quad i \in (1...N_e). \tag{4.8}$$

This formulation describes a hypothetic system of N_e non-interacting electrons in an effective potential V_{eff}. The particle density of the hypothetic system is equal to that of the original set of interacting electrons:

$$n(\boldsymbol{r}) = \sum_{i=1}^{N_e} |\phi_i(\boldsymbol{r})|^2. \tag{4.9}$$

The effective potential V_{eff} is a functional of the particle density:

$$V_{eff}(\boldsymbol{r}) = e^2 \int \frac{n(\boldsymbol{r}')}{|\boldsymbol{r} - \boldsymbol{r}'|} d^3\boldsymbol{r}' + \frac{\delta E_{xc}}{\delta n} - \sum_{\alpha=1}^{N_N} \frac{Z_\alpha e^2}{|\boldsymbol{r} - \boldsymbol{R}_\alpha|}. \tag{4.10}$$

Equations (4.8), (4.9) and (4.10) are called Kohn-Sham equations. Knowing E_{xc} they can be iteratively solved according to the following scheme:

$$n^{(0)} \rightarrow V_{eff} \rightarrow \phi_i^{(1)} \rightarrow n^{(1)} \rightarrow ... \tag{4.11}$$

From the solution the particle density and the ground state energy can be determined.

In the course of DFT investigations within the project COMFEM it was found that the ground state of PZT within the utilized virtual crystal approximation is not exactly tetragonal but slightly monoclinic, which is in agreement with experimental observations [Völker 2011]. Therefore,

some components of the tetragonal material tensors for PZT cannot be obtained within the DFT scheme. Another example is given by properties of 90° domain walls, deformed because of the broken tetragonal symmetry and, therefore, inapplicable for the development of the phase-field model. Moreover, the dielectric constants cannot be estimated from the DFT simulations because of the difficulty to apply an electric field to a super cell with periodic boundary conditions. In order to overcome these problems, the DFT data have been used to develop parameters for a classical empirical shell-model of PTO and PZT with a strictly tetragonal equilibrium ground state.

To illustrate the resulting effective elasticity and piezoelectricity tensors in the form of matrix arrays, the compressed matrix notation (also denoted as Voigt notation) is used:

$$c_{ijkl}^{E} \equiv c_{pq}^{E}, \quad e_{ikl} \equiv e_{ip} \, . \tag{4.12}$$

According to this notation the indices i, j, k, l are replaced by p,q as shown in Table 4.1.

ij or kl	p or q
11	1
22	2
33	3
12 or 21	4
13 or 31	5
23 or 32	6

Table 4.1: Compressed matrix (Voigt) notation.

4.2 Shell-model

In the shell-model [Dick 1958] an ion consists of two hypothetical particles, a core and a shell, which imitate the atomic nucleus and electron shell, respectively. The core has a charge X and the mass of the corresponding atom, whereas the shell has a charge Y and no mass. The sum of X and Y is equal to the charge of the ion Z. The displacement between the core and shell represents polarization. Figure 4.2 shows a schematic illustration of the interactions between cores and shells of two arbitrary ions.
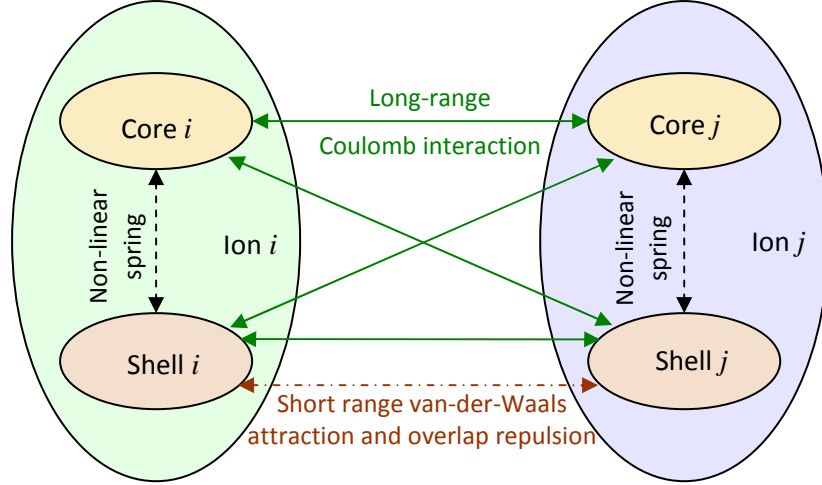
Figure 4.2: Interactions within the shell-model.

Three types of interactions are defined in the shell-model. The long-range interaction V_{LR} is represented by the Coulomb potential between cores and/or shells and by the interaction between dipoles and macroscopic electric field E:

$$V_{LR}(|\,\boldsymbol{r}_i - \boldsymbol{r}_j\,|) = \frac{q_i q_j}{4\pi\varepsilon_0} \frac{1}{|\,\boldsymbol{r}_i - \boldsymbol{r}_j\,|} - \left(q_i \boldsymbol{r}_i + q_j \boldsymbol{r}_j \right) \cdot \boldsymbol{E} \,. \tag{4.13}$$

Here, q_i and $\boldsymbol{r}_i$ denote the charge and the position of the core or shell respectively.

The short-range V_{SR} interaction includes the van-der-Waals attraction V_{vW} and the overlap repulsion V_o, which originate from the quantum mechanical Pauli principle:

$$V_{SR}(|\,\boldsymbol{r}_i - \boldsymbol{r}_j\,|) = V_o(|\,\boldsymbol{r}_i - \boldsymbol{r}_j\,|) + V_{vW}(|\,\boldsymbol{r}_i - \boldsymbol{r}_j\,|) = A_{ij} e^{-\frac{|\boldsymbol{r}_i - \boldsymbol{r}_j|}{\rho_{ij}}} - \frac{C_{ij}}{|\,\boldsymbol{r}_i - \boldsymbol{r}_j\,|^6} \,. \tag{4.14}$$

Here A_{ij}, ρ_{ij} and C_{ij} denote the potential parameters, which determine the pair interaction between ions. The last, third type of interactions is represented by the non-linear spring potential between a core and a shell of an ion:

$$V_{CS}(r) = \frac{1}{2} k_2 r^2 + \frac{1}{24} k_4 r^4 \,, \tag{4.15}$$

where k_2 and k_4 are the spring parameters and r the distance between the two hypothetic particles. The fourth-order anharmonic term is introduced to describe the effect of hybridization on the ionic polarizability of perovskite oxides [Shimada 2008].

The total potential, which summarizes the interaction of a particle i with all other particles and an external electric field, equals

$$V_i = \sum_j (V_{LR} + V_{SR} + V_{CS}).$$ (4.16)

Knowing V_i and equilibrium positions of cores and shells their dynamics can be estimated solving classical Newton's equations:

$$m_i \frac{\partial^2}{\partial t^2} \boldsymbol{r}_i = -\nabla V_i.$$ (4.17)

Furthermore, the knowledge of equilibrium particle locations $\boldsymbol{r}_i$ allows to derive the lattice constants, thickness and energies of domain walls as well as the total polarization

$$\boldsymbol{P} = \frac{1}{V} \sum_i \sum_{j>i} \left(q_i \boldsymbol{r}_i + q_j \boldsymbol{r}_j \right)$$ (4.18)

of a crystal. Hereby V is the volume of the super cell containing cores and shells. Consequently, the effective dielectric constant $\hat{\varepsilon}_{kl}$ can be estimated as

$$\hat{\varepsilon}_{kl} = \frac{\partial P_k}{\partial E_l}.$$ (4.19)

In the scope of the COMFEM-project the shell-model parameters A_{ij}, ρ_{ij}, C_{ij}, k_2 and k_4 for PTO and PZT were determined by fitting several materials properties obtained from the shell-model to those derived from the DFT calculations. The target properties were lattice constants, equilibrium positions of atoms, energy differences between selected configurations (e.g. with and without certain stacking faults), Born effective charges, elastic constants and phonon frequencies.

4.3 Phase-field method

This subsection is based on the thesis of B. Völker [Völker 2010], who developed the described phase-field model.

The key quantity of the phase-field model utilized in the multi-scale simulation chain within the project COMFEM is the Helmholtz free energy $\Psi(P_i, P_{i,j}, S_{ij}, D_i)$, which describes an energy density per unit volume. The Helmholtz energy is a polynomial series expansion depending on the components of the polarization vector P_i, the polarizations gradient $P_{i,j} \equiv \frac{\partial P_i}{\partial P_j}$, the strain S_{ij} and the dielectric displacement D_i. The energy functional consists of five parts: the Landau

energy ψ_{Landau} , the gradient energy ψ_{grad} , the electrostrictive coupling energy ψ_{coup} , the elastic

energy ψ_{elast} and the electric energy ψ_{elec} :

$$\Psi\left(P_i, P_{i,j}, \delta_{ij}, D_i\right) =$$
$$= \psi_{Landau}\left(P_i\right) + \psi_{grad}\left(P_{i,j}\right) + \psi_{coup}\left(S_{ij}, P_i\right) + \psi_{elast}\left(S_{ij}\right) + \psi_{elec}\left(P_i, D_i\right) =$$
$$= \sum_i \alpha_i P_i^2 + \sum_{i,j} \alpha_{ij} P_i^2 P_j^2 + \sum_{i,j,k} \alpha_{ijk} P_i^2 P_j^2 P_k^2 + \sum_{i,j,k,l} G_{ijkl} P_{i,j} P_{k,l} + \qquad (4.20)$$
$$+ \sum_{i,j,k,l} Q_{ijkl} S_{ij} P_k P_l + \sum_{i,j,k,l} c_{ijkl} S_{ij} S_{kl} + \frac{1}{2\varepsilon_0} \sum_i \left(D_i - P_i\right)^2 .$$

The Landau potential ψ_{Landau} describes an energy landscape with a certain number of energeti-cally equivalent global minima. These global minima define the states of spontaneous polariza-tion. The spatial symmetry of the degenerated energy minima specifies the phase of the mate-rial. For a tetragonal ferroelectric material like BTO, four equivalent minima are located in the x-y-plane along the <100> and <010> axes (see Figure 4.3). Two further equivalent minima are positioned along the <001> direction. Landau energy represents the potential of a bulk material in the absence of mechanical stress, electromechanical coupling and structural inhomogeneities (for example domain walls). In the scope of the project COMFEM the expansion of ψ_{Landau} up to the sixth order has been implemented.
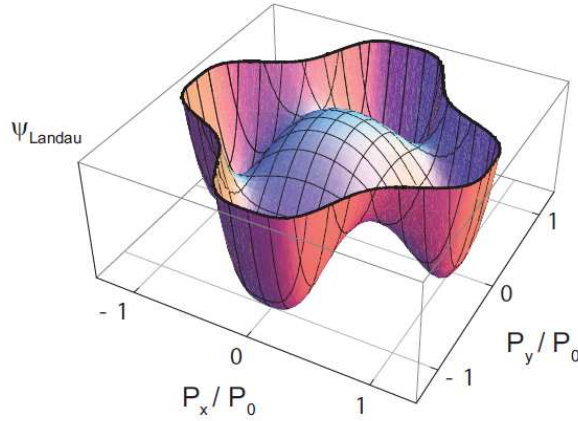
Figure 4.3: Three-dimensional representation of the Landau energy potential $\psi(P_x, P_y)$ for a tetrago-nal ferroelectric material [Völker 2010]. Four equivalent minima define the degenerated ground states of the spontaneous polarization in the x-y-plane.

The gradient energy ψ_{grad} contributes in the cases, when the polarization changes spatially, e.g. in domain walls. Hence, it enforces formation of any polarization gradients including domain walls. ψ_{elast} describes energy resulting from the applied external mechanical stresses, while

ψ_{coup} takes into account the effect of mechanical loading on spontaneous polarization and strain. In a cubic phase (in absence of spontaneous polarization) ψ_{elast} and ψ_{coup} vanish when no mechanical fields are applied. In a homogeneously polarized material without any external mechanical or electrical loading ψ_{elast} and ψ_{coup} have the same value but different signs and, hence, cancel each other. The electric potential ψ_{elect} represents the energy of electric field, stored in the space occupied by the material.

In the phase-field model temporal and spatial evolution of the polarization is governed by the Ginzburg-Landau equation, which requires minimization of the Helmholtz free energy.

$$\left(\frac{\partial \Psi}{\partial P_{i,j}} \right)_{,j} - \frac{\partial \Psi}{\partial P_i} = \beta_{ij} \frac{\partial P_j}{\partial t} . \tag{4.21}$$

According to [Völker 2011] the Helmholtz energy (4.20) is uniquely defined by the 15 independent coefficients, which are called $\alpha_1, \alpha_{11}, \alpha_{111}, \alpha_{12}, \alpha_{112}, \alpha_{123}, G_{11}, G_{12}, G_{44}, Q_{11}, Q_{12}, Q_{44}$ and c_{11}, c_{12}, c_{44}. For the latter three elastic constants the Voigt notation has been used (see Table 4.1). All these constants can be adjusted to physical properties obtained by DFT calculations in several steps presented in the following [Völker 2010].

The sensitivity study of the Helmholtz energy, where all model parameters have been slightly varied, has pointed out that the elastic constants c_{11}, c_{12} and c_{44} are completely decoupled from all other coefficients and can be directly transferred from the elastic stiffness tensor obtained by DFT-calculations (see equation (4.2)):

$$c_{ij} = \hat{c}_{ij} . \tag{4.22}$$

The electrostrictive coupling coefficients have been determined via the procedure described in [Devonshire 1954] from the spontaneous strains $\hat{S}_{\parallel}$, $\hat{S}_{\perp}$ and spontaneous polarization $\hat{P}_0$ obtained in DFT-calculations:

$$Q_{11} = \frac{\hat{S}_{\parallel}}{\hat{P}_0^2} , \qquad Q_{12} = \frac{\hat{S}_{\perp}}{\hat{P}_0^2} . \tag{4.23}$$

The curvature of the Helmholtz energy as a function of polarization defines the dielectric permittivities $\hat{\varepsilon}_{11}$ and $\hat{\varepsilon}_{33}$ [Devonshire 1948]:

$$\frac{\partial^2 \psi_{Landau}}{\partial P_1^2} = \frac{1}{\hat{\varepsilon}_{11}} , \qquad \frac{\partial^2 \psi_{Landau}}{\partial P_{33}^2} = \frac{1}{\hat{\varepsilon}_{33}} . \tag{4.24}$$

Introducing the Helmholtz free energy (4.20) into equation (4.24) for the homogeneously polarized stress- and field-free state with magnitude of spontaneous polarization $\hat{P}_0$ the Landau energy coefficients α_1, α_{111} and α_{112} can be expressed in terms of the α_{11}-constant [Völker 2011].

The Landau coefficient α_{11} as well as the gradient coefficient G_{44} have been derived in the next step from two non-linear algebraic equations for the thickness $\hat{\xi}_{180}$ and the energy $\hat{\gamma}_{180}$ of a 180° domain wall:

$$\hat{\xi}_{180} = \frac{2\hat{P}_0}{\left.\dfrac{\partial P_3(x_1)}{\partial x_1}\right|_{x_1=0}}, \quad \hat{\gamma}_{180} = \int_{-\infty}^{\infty} \left(\Psi\left(P_3(x_1), P_{3,1}(x_1), S_{11}(x_1)\right) - \Psi_{bulk} \right) dx_1. \quad (4.25)$$

The first equation implements the geometrical definition of the domain wall thickness, see Figure 4.4. Ψ_{bulk} in the second equation symbolizes the equilibrium bulk energy density.
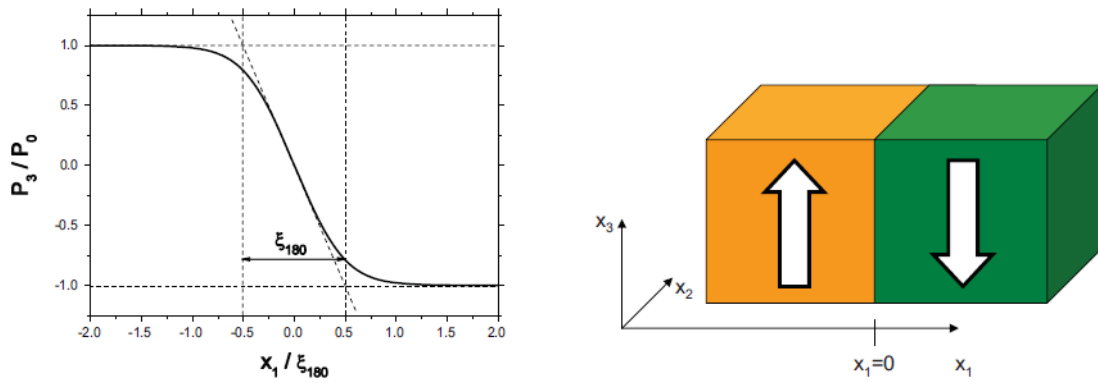

Figure 4.4: Polarization profile and thickness $\hat{\xi}_{180}$ of a 180° domain wall [Völker 2010].
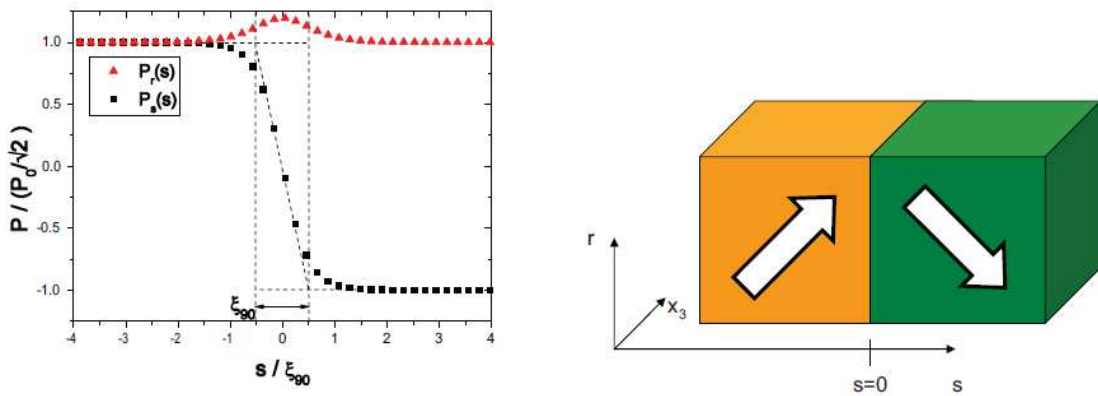

Figure 4.5: Polarization profile and thickness $\hat{\xi}_{90}$ of a 90° domain wall [Völker 2010].

In the case of a 90° domain wall the Landau-Ginzburg equation (4.21) cannot be solved analytically. In order to overcome this difficulty the minimization of the Helmholtz energy can be carried out numerically in a finite element formulation [Su 2007], where the components of the polarization P_i, the mechanical displacement u_i and the electrical potential ϕ are used as degrees of freedom. The domain wall thickness ξ_{90} and energy γ_{90} can than be calculated in the notation of Figure 4.5 from the following two equations:

$$\xi_{90} = \frac{\dfrac{2\sqrt{\hat{P}_0}}{2}}{\left.\dfrac{\partial P_s(s)}{\partial s}\right|_{s=0}},$$

$$\gamma_{90} = \int_{-\infty}^{\infty} \left(\Psi\left(P_s(s), P_r(s), P_{s,s}(s), P_{r,s}(s), S_{ss}(s), S_{rs}(s), \phi(s)\right) - \Psi_{bulk} \right) ds.$$

(4.26)

For the calculation of ξ_{90} and γ_{90} an extended 2D-model has been utilized. In this model, three components of the polarization and three components of the mechanical displacement are implemented as degrees of freedom, although the model is spatially confined to the two-dimensional plane. The confinement of three-dimensional vectorial characteristics to the two-dimensional geometry has been dictated by enormous computational effort required for three-dimensional models.

Sensitivity analysis [Völker 2010] has shown that the 90° domain wall properties depend on the energy coefficients α_{12}, G_{11} and G_{12}. In particular, α_{12} determines the height of the energy barrier between the neighboring minima, while G_{11} and G_{12} determine the shift, the thickness and the energy of a 90° domain wall. Hence, the coefficients α_{12}, G_{11} and G_{12} have been systematically varied, the stable polarization configurations, the $P_s(s)$ and $P_r(s)$ curves have been calculated. Domain wall thickness ξ_{90} and energy γ_{90} have been then obtained using equation (4.26). The above described steps have been iterated until a set of Helmholtz coefficients is found that matches the predictions of DFT-calculations $\hat{\xi}_{90}$ and $\hat{\gamma}_{90}$ [Völker 2010].

According to [Völker 2010], the Landau energy coefficient α_{123} has no influence on the tetragonal material properties, but rather controls the energy barrier between neighboring minima of the Landau energy changing the height of the saddle point along the <111> direction. Parameter α_{123} has been chosen in such a way that the heights of the energy barriers in <110> and <111>

75

directions become identical. The last unknown coefficient Q_{44} has been adjusted to match the piezoelectric coefficient $\hat{d}_{15}$ obtained from the DFT simulations. Since in the described phase-field approach the sixth order expansion of the Landau energy was implemented[5] the $\hat{d}_{31}$ and $\hat{d}_{33}$-constants were not used in the adjustment, which restricts predictability of the multi-scale approach.

For the evaluation of the small-signal parameters of the entire equilibrium domain configuration the average values of the stress $\langle T_i \rangle$, strain $\langle S_i \rangle$, electric field $\langle E_i \rangle$ and dielectric displacement $\langle D_i \rangle$ tensors have been calculated from the nodal results as

$$\langle X_i \rangle = \frac{1}{A} \int_A X_i \left(x_1, x_2 \right) dx_1 dx_2, \tag{4.27}$$

where A is the area of the extended 2D-model in the x_1-x_2-plane. The dielectric and piezoelectric constants ε_{ij}^S and e_{ikl} have been obtained via application of the electrical load E_i while keeping the global strain constant as:

$$\varepsilon_{ij}^S = \frac{\partial \langle D_i \rangle}{\partial \langle E_j \rangle}, \tag{4.28}$$

$$e_{ikl} = \frac{\partial \langle T_{kl} \rangle}{\partial \langle E_i \rangle}. \tag{4.29}$$

Correspondingly, the application of a mechanical load at a constant electric field yields the elastic small-signal constants:

$$c_{ijkl}^E = \frac{\partial \langle T_{ij} \rangle}{\partial \langle S_{kl} \rangle}. \tag{4.30}$$

The obtained results (see section 3.6) are given in Voigt notation (see section 4.1, Table 4.1).

4.4 Micromechanical modeling

The basic idea of the micromechanics is homogenization of the microstructure. Hereby the homogeneous material properties on the macro-scale have to be derived from the heterogeneous structure on the micro-scale. The region under investigation on the micro-scale has to be large enough to ensure the independence of the effective physical properties on the microstructure.

---

[5] due to the limited duration of the COMFEM project

At the same time the investigated sample has to be small enough to neglect the stress gradients on the macroscopic scale within the micro-region. A region which fulfills these requirements is called representative volume element. Geometrical modeling of the representative volume element has been discussed in the previous chapter. In the present and following sections different physical modeling procedures of the representative volume element are introduced.

An often used micromechanical approach for the determination of effective material parameters is the self-consistent method of effective medium. In this model a micro component like a grain, a pore or a crack with a known elastic tensor c^I, dielectric tensor ε^I and piezoelectric tensor e^I is surrounded by an infinitely large effective medium. This medium possesses effective material parameters c^*, ε^* and e^* to be determined. According to [Dunn 1995] the required macroscopic effective material tensors depend on those of the inclusion c^I, ε^I and e^I and on the so-called concentration tensors A^I, a^I, B^I and b^I:

$$c^* = \left(\left\{ c^I A^I \right\} + \left\{ \left(e^I \right)^T a^I \right\} \right) \left\{ A^I \right\}^{-1},$$

$$-\varepsilon^* = \left(\left\{ e^I B^I \right\} + \left\{ \varepsilon^I b^I \right\} \right) \left\{ b^I \right\}^{-1}.$$

(4.31)

Hereby $\{\ \}$ represents an average over grain orientations weighted by the orientation distribution function $w(\zeta,\psi,\varphi)$; i.e.

$$\{\ \} = \int\limits_{0}^{2\pi} \int\limits_{0}^{2\pi} \int\limits_{-1}^{1} (\ )\, w(\zeta,\psi,\varphi)\, d\zeta\, d\psi\, d\varphi .$$

(4.32)

Dunn and Taya derived the dependency of the concentration tensors on the material properties of the inclusion and on that of the effective medium [Dunn 1993]:

$$A_2 = J_1^{-1} + J_1^{-1} J_2 \Gamma^{-1} J_3 J_1^{-1}$$

$$B_2 = -J_1^{-1} J_2 \Gamma^{-1}$$

$$a_2 = -\Gamma^{-1} J_3 J_1^{-1}$$

(4.33)

$$b_2 = \Gamma^{-1}$$

$$\Gamma = J_4 - J_3 J_1^{-1} J_2$$

where

$$J_1 = I + S_e \left[S^* \left(c^I - c^* \right) + g^{*T} \left(e^I - e^* \right) \right] + S_{ed} \left[g^* \left(c^I - c^* \right) - \varepsilon^{*-1} \left(e^I - e^* \right) \right]$$

$$J_2 = S_e \left[S^* \left(e^I - e^* \right) + g^{*T} \left(\varepsilon^I - \varepsilon^* \right) \right] + S_{ed} \left[g^* \left(e^I - e^* \right) + \varepsilon^{*-1} \left(\varepsilon^I - \varepsilon^* \right) \right]$$

$$J_3 = S_{de} \left[S^* \left(c^I - c^* \right) + g^{*T} \left(e^I - e^* \right) \right] + S_d \left[g^* \left(c^I - c^* \right) - \varepsilon^{*-1} \left(e^I - e^* \right) \right]$$ (4.34)

$$J_4 = I + S_{de} \left[S^* \left(e^I - e^* \right) + g^{*T} \left(\varepsilon^I - \varepsilon^* \right) \right] + S_d \left[g^* \left(e^I - e^* \right) + \varepsilon^{*-1} \left(\varepsilon^I - \varepsilon^* \right) \right]$$

In the latter equations $g^* = d^* \varepsilon^{*-1} = c^{*-1} e^* \varepsilon^{*-1}$. S_e, S_{ed}, S_{de} and S_d are the piezoelectric analog of the Eshelby's tensor in elasticity (see [Dunn 1993]). Equations (4.31) with (4.33) and (4.34) are self-consistent and can be iteratively solved for the effective material parameters c^*, ε^* and e^*.

By means of the above presented method the influence of the aspect ratio of spheroidal grains on the effective material constants of BTO has been investigated in [Dunn 1995]. Differences between elastic coefficients for oblate and prolate grains of an unpoled ceramic were found to be small. The calculated effective dielectric constant of spherical and prolate grains (1400) lies in the range of the corresponding experimental value, while the same coefficient for the oblate grains is by more than 50% smaller.

Nan and Clarke applied the self-consistent method in order to evaluate the effect of the grain shape and orientation on the effective piezoelectric properties of polarized BTO ceramics [Nan 1996]. The piezoelectric modules have been found to be nonsensitive to a wide range of the grain shapes.

Pertsev used an advanced self-consistent method of effective piezoelectric medium, "which takes into account the piezoelectric interactions between grains in full measure" [Pertsev 1998]. In this work besides the effective parameters for bulk BTO and PTO ceramics the influence of the two-dimensional clamping by the substrate on the ferroelectric thin films has been investigated. The results are illustrated in Figure 4.6.
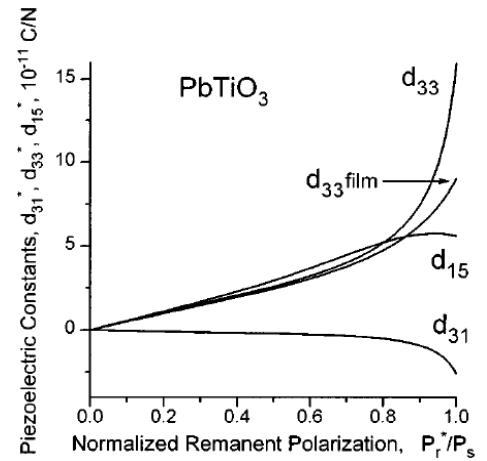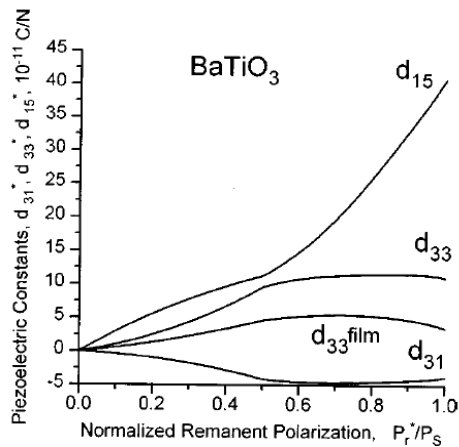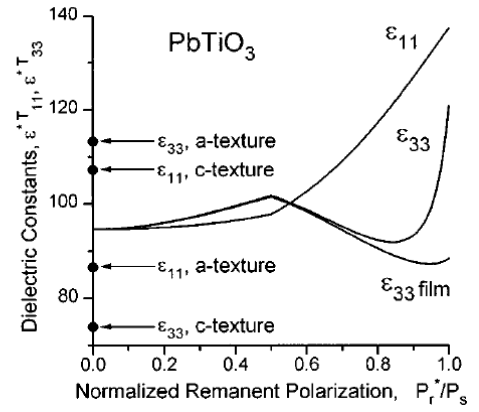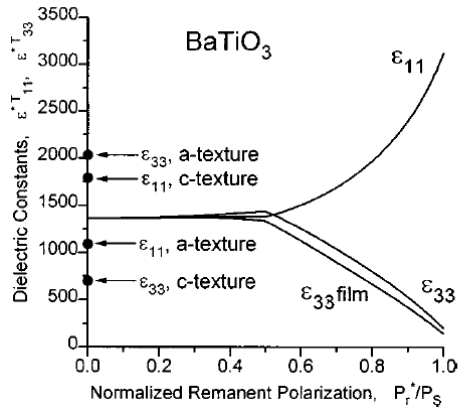
Figure 4.6: Variations of the effective dielectric and piezoelectric coefficients as a function of the remanent polarization for BTO and PTO thin films and bulk ceramics [Pertsev 1998].

In the work of Pertsev as well as in the publication of Nan polarizations are assumed to be uniformly distributed within a cone with a threshold opening angle θ_E around the applied electric field (see Figure 4.7). However, the prediction and physical motivation of the total remanent polarization as well as the corresponding polarization distribution seems to be impossible within this approach. For this reason all calculated material parameters in [Pertsev 1998, Nan 1996] are presented as a functions of the critical angle θ_E or corresponding remanent polarization P_r^*, while the expectation values of the material parameters are not discussed.
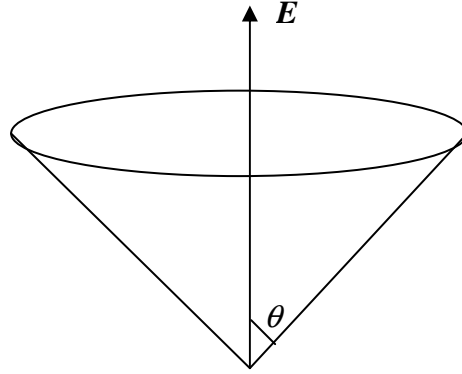
Figure 4.7: Orientations of polarizations in the models of [Nan 1996], [Pertsev 1998], [Fröhlich 2002] and [Jayachandran 2007] are assumed to lie within a cone with opening angle θ around the applied electric field.

In [Fröhlich 2002] the next step has been made and the tetragonal symmetry of BTO has been taken into account for the determination of the polarization configuration. Initially, the polarization is distributed uniformly in this model. Then, the domains having $\theta > \theta_E$ switch into one of six crystallographic directions building the smallest angle with the applied electric field. In the present investigation the model [Fröhlich 2002] with $\theta_E = 0$ has been implemented. We address this prescription for the polarization orientation as the "smallest (or least) angle model".
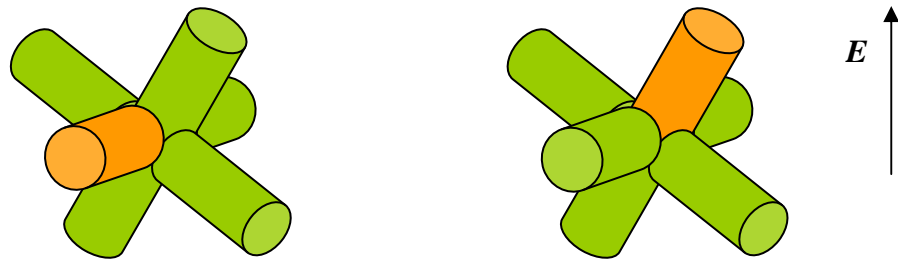
Figure 4.8: Switching event of polarization direction (orange cylinder) in the „least angle model".

In [Fröhlich 2002] the procedure of homogenization was carried out by means of a numerical 2D finite element model instead of an analytical self-consistent method. A 2D representative volume element was filled with polygons (see chapter 3) and discretized with 2D finite elements. For all nodes coupled mechanical and electric field equations were solved:

$$\nabla \cdot \left(c_{ijkl}^{E} S_{kl} - e_{ijk} E_k \right) = 0$$
$$\nabla \cdot \left(e_{ijk} S_{kl} + \varepsilon_{ij}^{S} E_j \right) = 0.$$

(4.35)

The mean values of elastic modules of 2D grain models from the Hard-core-Voronoi, Poisson-Voronoi and Cluster-Voronoi tessellations (see chapter 2) were compared and no differences were found [Fröhlich 2002].

According to the above introduced models of the poling by an external electric field the threshold angle θ_E exists, which is considerably smaller than 90° at the late stages of poling, which means in the fully saturated or in the remanent state. In contrast, the models of polarization ensembles described in [Jayachandran 2008] and [Jayachandran 2009] assume that the Euler angle θ of the polarization vector follows the normal (Gaussian) probability distribution function with 0 as the mean value:

$$f(\theta) = \frac{1}{\sigma\sqrt{2\pi}} e^{-\frac{\theta^2}{2\sigma^2}}. \tag{4.36}$$

Here, the standard deviation σ controls the distribution of polarization orientations. For $\sigma \to 0$ the ferroelectric domains are highly textured. In contrast, for $\sigma \to \infty$ the polarizations configuration is isotropic. In the mentioned publications a maximum for the effective piezoelectric coefficient d_{33}^* in thin film and in bulk BTO ceramics has been found at $\sigma \approx 0.6$, which is quite high textured (see Figure 4.9). Corresponding distribution function of the Euler angle θ and that of the z-components of polarization P_z in the direction of the applied electric field is plotted in Figure 4.9. Obviously, in this model orientations with $\theta > 90°$ in the poled, highly anisotropic state are predicted.
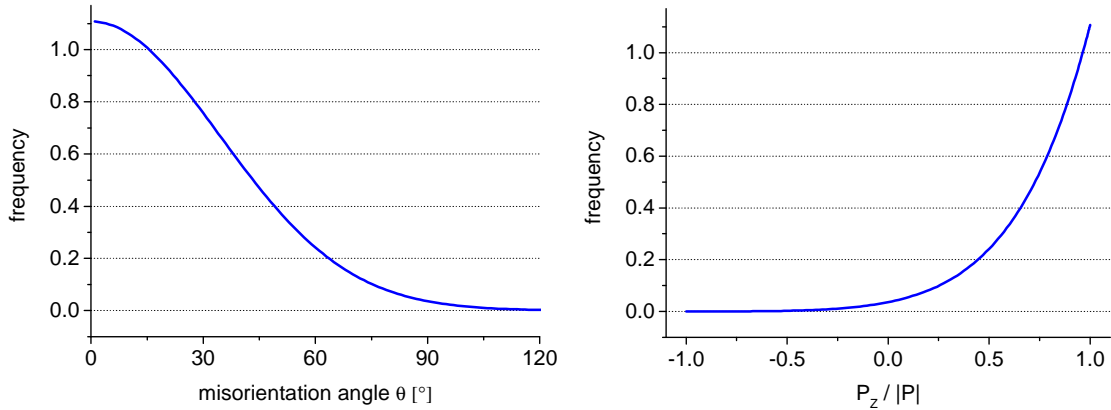
Figure 4.9: Polarization distribution according to [Jayachandran 2008] and [Jayachandran 2009].

Models from [Jayachandran 2009] provide identical polarization configurations for all materials at a certain value of the total remanent polarization, which might be false. In the next section we introduce the Huber-Fleck model. It allows to simulate the development of polarization con-

figuration during a large-signal excitation in dependence on the material specific single-crystal constants, spontaneous strain, spontaneous polarization, switching energy etc.

4.5 Calculations in the framework of the Huber-Fleck model

The Huber-Fleck procedure is a constitutive model for the non-linear switching of ferroelectric polycrystals under a combination of mechanical stress and electric field [Huber 1999], [Huber 2001]. In [Huber 1999], [Huber 2001] a self-consistent analysis has been performed in order to estimate the macroscopic response of tetragonal crystals. In the present work a three-dimensional finite element simulation according to [Pathak 2009] is utilized. For the case of tetragonal polycrystals the model was implemented by L. Kunz [Kunz].

In the implementation of Pathak every polycrystalline grain is represented by the 8-noded cubic element. In our model single grains may have complex polyhedral shape (see chapter 3.3). For this reason they cannot be discretized by the regular cubical elements. Instead, 5 to 40 4-noded tetrahedral elements are located in a grain. Each finite element possesses four Gaussian integration points used to compute all necessary volume integrals. At every integration point volume fractions c^I of domain type I are defined. In a tetragonal crystal there are $M = 6$ variants of polarization direction $I = 1...6$ and $N = M(M-1) = 30$ switching systems (possibilities for the orientation switching).

The load-depending change of the domain volume fractions c^I is calculated in several steps. We call these loading steps also time steps. The size of a time step is adaptively varied during the large-signal excitation. At the loading level, at which many domains switch and the total strain as well as polarization grow rapidly, somewhat smaller steps have been used for the sake of convergency. In contrast, in the case when no switching took place, larger time steps were sufficient.

For each time step the calculations start with the values of stress tensor T_{ij}, electric field E_i, dielectric displacement D_i as well as domain volume fractions c^I at each Gauss point. Further input parameters of the Huber-Fleck model are summarized in Table 4.2. At the beginning of the first loading step the volume fractions of polarization domains were assumed to be

82

equal: $c^1 = c^2 = \ldots = c^6 = \dfrac{1}{6}$. Consequently, the stress and the strain at each Gauss point vanish.

Input parameter	Identifier
Single-crystal stiffness tensor	s_{ijkl}^{E}
Single-crystal dielectricity tensor	ε_{ij}^{S}
Single-crystal piezoelectricity tensor	d_{ijk}
Spontaneous polarization	P^0
Spontaneous strain	S^0
Critical driving force for a 90° domain switch	$G_c^{90°}$
Critical driving force for a 180° domain switch	$G_c^{180°}$
Scaling factor	B^α
Creep exponent	n
Hardening parameter	C_0

Table 4.2: Input parameters of the Huber-Fleck model.

At every time step mechanical and electrical field equations are solved. For the finite element implementation the finite element interpolation matrices for strain $[B_S]$, displacement $[A_u]$, electric field $[B_E]$ and for electric potential $[A_\phi]$ were defined, such that $\{S\} = [B_S]\{u_n\}$, $\{u\} = [A_u]\{u_n\}$, $\{E\} = [B_E]\{\phi_n\}$ and $\{\phi\} = [A_\phi]\{\phi_n\}$. Hereby $\{u_n\}$ and $\{\phi_n\}$ are the nodal displacements and the nodal values of the electric potential for the finite element model. By means of the interpolation matrices field equations can be written in the weak form

$$\int_V [B_S]\{T\}\,dV = \int_A [A_u]^T \{T'\}\,dA$$
$$\int_V [B_E]\{D\}\,dV = \int_A [A_\phi]^T \{q\}\,dA. \tag{4.37}$$

Here, $\{T'\}$ is an array of surface traction components and q is the surface charge density.

With the effective stiffness matrix

$$[K_{Fu}] = \int_V [B_S]^T [\hat{s}]^{-1} [B_S]\,dV, \tag{4.38}$$

the effective piezoelectric matrix

$$\left[K_{qu} \right] = \int\limits_{V} \left[B_{E} \right]^{T} \left[\hat{d} \right] \left[\hat{s} \right]^{-1} \left[B_{E} \right] dV \,, \tag{4.39}$$

the effective capacitance matrix

$$\left[K_{q\phi} \right] = \int\limits_{V} \left[B_{E} \right]^{T} \left(\left[\hat{\varepsilon} \right] - \left[\hat{d} \right] \left[\hat{s} \right]^{-1} \left[\hat{d} \right]^{T} \right) \left[B_{E} \right] dV \,, \tag{4.40}$$

the incremental nodal forces

$$\left\{ \Delta F_{n} \right\} = \int\limits_{A} \left[A_{u} \right]^{T} \left\{ T' \right\}^{V} dA - \int\limits_{V} \left[B_{S} \right]^{T} \left\{ T \right\}^{V-1} dV + \int\limits_{V} \left[B_{S} \right]^{T} \left[\hat{C} \right] \left[\Delta \hat{S}^{R} \right] dV \,, \tag{4.41}$$

and the incremental nodal charges

$$\left\{ \Delta q_{n} \right\} = \int\limits_{A} \left[A_{\phi} \right]^{T} q^{V} dA - \int\limits_{V} \left[B_{E} \right]^{T} \left\{ D \right\}^{V-1} dV +$$
$$+ \int\limits_{V} \left[B_{E} \right]^{T} \left[\hat{d} \right] \left[\hat{s} \right]^{-1} \left[\Delta \hat{S}^{R} \right] dV - \int\limits_{V} \left[B_{E} \right]^{T} \left\{ \Delta \hat{D}^{R} \right\} dV. \tag{4.42}$$

equations (4.37) can be written as system of equations for the change of the nodal displace-

ments $\left\{ \Delta u_{n} \right\}$ and electric potentials $\left\{ \Delta \phi_{n} \right\}$ during the loading (time) step V:

$$\left[K_{Fu} \right] \left\{ \Delta u_{n} \right\} - \left[K_{qu} \right]^{T} \left\{ \Delta \phi_{n} \right\} = \left\{ \Delta F_{n} \right\}$$
$$\left[K_{qu} \right] \left\{ \Delta u_{n} \right\} - \left[K_{q\phi} \right]^{T} \left\{ \Delta \phi_{n} \right\} = \left\{ \Delta q_{n} \right\}. \tag{4.43}$$

Tensors $\hat{s}$, $\hat{d}$, $\hat{\varepsilon}$, $\Delta \hat{S}^{R}$ and $\Delta \hat{D}^{R}$ originate from the previous loading step.

Change of the strain ΔS and electric field ΔE as well as the new total strain S^{V} and electric

field E^{V} at the loading step V for each Gauss point can be calculated from the solution of (4.43)

as

$$\left\{ \Delta S \right\} = \left[B_{S} \right] \left\{ \Delta u_{n} \right\}$$
$$\left\{ \Delta E \right\} = \left[B_{E} \right] \left\{ \Delta \phi_{n} \right\} \tag{4.44}$$

$$\left\{ S^{V} \right\} = \left\{ S^{V-1} \right\} + \left\{ \Delta S \right\}$$
$$\left\{ E^{V} \right\} = \left\{ E^{V-1} \right\} + \left\{ \Delta E \right\}. \tag{4.45}$$

For calculation of the input data for the next step ΔS , ΔE (equations (4.44)) and the opera-

tion rate $\dot{f}^{\alpha}$ of switching system α from the previous loading step are required. The value $\dot{f}^{\alpha}$

describes how large the change of the volume fractions c^{I} is. The change of stress ΔT, dielec-

tric displacement ΔD, rate of operation Δf^{α} and domain volume fraction Δc^{I} during the pre-

sent loading step in each Gauss point can be obtained via

$$\{\Delta T\} = [s]^{-1}\{\Delta S\} - [\hat{s}]\big[\hat{d}\big]\{\Delta E\} - [s]^{-1}\big\{\Delta \hat{S}^R\big\}$$

$$\{\Delta D\} = \big[\hat{d}\big][s]^{-1}\{\Delta S\} - \Big([\hat{\varepsilon}] - \big[\hat{d}\big][s]^{-1}\big[\hat{d}\big]^T\Big)\{\Delta E\} - \big\{\Delta \hat{D}^R\big\}$$

$$\Delta f^\alpha = \dot{f}^\alpha \Delta t\left(1 + \theta \frac{n}{G^\alpha}\Big(\hat{D}_i^\alpha \Delta E_i + \hat{S}_{ij}^\alpha \Delta T_{ij}\Big)\right)$$

$$\Delta c^I = \sum_{\alpha=1}^{30} A^{I\alpha}\Delta f^\alpha .$$

(4.46)

The matrix $A^{I\alpha}$ indicates, which domain I increases ($A^{I\alpha}=1$), depletes ($A^{I\alpha}=-1$) or remains unchanged ($A^{I\alpha}=0$) in the course of the switching process α.

The new values of stress, dielectric displacement and domain volume fraction are consequently

$$\{T\}^\nu = \{T\}^{\nu-1} + \{\Delta T\}$$

$$\{D\}^\nu = \{D\}^{\nu-1} + \{\Delta D\}$$

$$c^{I,\nu} = c^{I,\nu-1} + \Delta c^I .$$

(4.47)

For each possible switching system α the linear response of the strain $\tilde{S}_{ij}^\alpha$ and dielectric displacement $\tilde{D}_i^\alpha$ of the changed domains can be calculated as

$$\tilde{S}_{ij}^\alpha = \sum_I A^{I\alpha}\Big(s_{ijkl}^{E(I)}T_{kl} + d_{kij}^{(I)}E_k\Big)$$

$$\tilde{D}_i^\alpha = \sum_I A^{I\alpha}\Big(d_{ikl}^{(I)}T_{mn} + \varepsilon_{ik}^{T(I)}E_k\Big).$$

(4.48)

Hereby $s_{ijkl}^{E(I)}$, $d_{ikl}^{(I)}$ and $\varepsilon_{ik}^{T(I)}$ are elastic, piezoelectric and dielectric tensors of the different domains I, which can be obtained from the single-crystal values s_{ijkl}^E, d_{ikl}, ε_{ik}^T and Euler angles ψ, θ, φ. If Euler angles describe transformation from the local coordinate system of the crystal into the global coordinate system of the sample accordingly to the Z-X-Z convention (right-handed rotation around the z axes by angle ψ, followed by the right-handed rotations around the new axes x' by θ, and around the resulting z'' axes by angle φ), the rotation matrix is

$$M = \begin{pmatrix} \cos\varphi & -\sin\varphi & 0 \\ \sin\varphi & \cos\varphi & 0 \\ 0 & 0 & 1 \end{pmatrix}\begin{pmatrix} 1 & 0 & 0 \\ 0 & \cos\theta & -\sin\theta \\ 0 & \sin\theta & \cos\theta \end{pmatrix}\begin{pmatrix} \cos\psi & -\sin\psi & 0 \\ \sin\psi & \cos\psi & 0 \\ 0 & 0 & 1 \end{pmatrix}. \quad (4.49)$$

Material tensors in the global coordinate system can be obtained as

$$\varepsilon_{ik}^{T(I)} = M_{ip}M_{kq}\varepsilon_{pq}^T,$$

$$d_{ikl}^{(I)} = M_{ip}M_{kq}M_{ls}d_{pqs},$$

$$s_{ijkl}^{E(I)} = M_{ip}M_{jq}M_{ks}M_{lt}s_{pqst}^E.$$

(4.50)

With non-linear contributions to the strain ΔS^α and polarization ΔP^α due to the switching process α, the total strain $\hat{S}^\alpha$, and polarization $\hat{P}^\alpha$ at the end of the switching process α can be written as

$$\hat{S}^\alpha = \tilde{S}^\alpha + \Delta S^\alpha$$
$$\hat{P}^\alpha = \tilde{P}^\alpha + \Delta P^\alpha.$$

(4.51)

The driving force leading to a specific switching α is defined as

$$G^\alpha = \left(\Delta P_i^\alpha + \frac{1}{2}\tilde{D}_i^\alpha \right)E_i + \left(\Delta S_{ij}^\alpha + \frac{1}{2}\tilde{S}_{ij}^\alpha \right)T_{ij}.$$

(4.52)

Dependence of $\dot{f}^\alpha$ on the driving force G^α is proposed [Kamlah 2005] as

$$\dot{f}^\alpha = B^\alpha \left| \frac{G^\alpha}{G_c^\alpha} \right|^{n-1} \left(\frac{G^\alpha}{G_c^\alpha} \right).$$

(4.53)

Hereby B^α is a scaling factor, n is a creep exponent and G_c^α is the critical driving force. Reasonable values for the creep exponent were identified to vary between 10 and 50. Accordingly to the relation (4.53) a switching event α occurs even in the case of $G^\alpha < G_c^\alpha$. However it is rather sluggish. In contrast, if $G^\alpha > G_c^\alpha$ the rate of operation is high.

Using (4.48), (4.51), (4.52) and (4.53) one finds

$$\hat{s}_{ijkl} = \sum_{I=1}^{6} c^I s_{ijkl}^I + \left(\sum_{\alpha=1}^{30} \frac{\dot{f}^\alpha}{G^\alpha} \hat{S}_{ij}^\alpha \hat{S}_{kl}^\alpha \right)\lambda n \Delta t$$

$$\hat{d}_{kij} = \sum_{I=1}^{6} c^I d_{kij}^I + \left(\sum_{\alpha=1}^{30} \frac{\dot{f}^\alpha}{G^\alpha} \hat{D}_k^\alpha \hat{S}_{ij}^\alpha \right)\lambda n \Delta t$$

$$\hat{\varepsilon}_{ijkl} = \sum_{I=1}^{6} c^I \varepsilon_{ik}^I + \left(\sum_{\alpha=1}^{30} \frac{\dot{f}^\alpha}{G^\alpha} \hat{D}_i^\alpha \hat{D}_k^\alpha \right)\lambda n \Delta t$$

(4.54)

$$\Delta \hat{S}_{ij}^R = \sum_{\alpha=1}^{30} \hat{S}_{ij}^\alpha \dot{f}^\alpha \Delta t$$

$$\Delta \hat{D}_i^R = \sum_{\alpha=1}^{30} \hat{D}_i^\alpha \dot{f}^\alpha \Delta t,$$

where λ is a weighting factor $0 \leq \lambda \leq 1$. With tensors (4.54), rates of operation $\dot{f}^\alpha$, and domain volume fractions c^I the next loading step can be carried out.

The macroscopic values of strain $\langle S \rangle$, electric field $\langle E \rangle$ and dielectric displacement $\langle D \rangle$ for each time step ν have been calculated from the nodal values $\{S\}$, $\{E\}$ and $\{D\}$ obtained in (4.45) and (4.47) via integration over the volume V of the representative volume element:

$$\langle S \rangle = \frac{1}{V} \int_V \{S\} dV,$$

$$\langle E \rangle = \frac{1}{V} \int_V \{E\} dV, \qquad (4.55)$$

$$\langle D \rangle = \frac{1}{V} \int_V \{D\} dV, \text{ etc.}$$

The effective piezoelectric d_{33}^* and dielectric ε_{33}^* material coefficients of a polycrystal have been obtained from these macroscopic mean values via numerical differentiation (similar to (4.28), (4.29) and (4.30)):

$$d_{33}^* = \frac{\partial \langle S_3 \rangle}{\partial \langle E_3 \rangle}, \qquad (4.56)$$

$$\varepsilon_{33}^* = \frac{\partial \langle D_3 \rangle}{\partial \langle E_3 \rangle}. \qquad (4.57)$$

4.6 Multi-scale coupling

In the present chapter practical procedures connecting the micromechanical Huber-Fleck simulations with the DFT, shell-model and phase-field procedures are proposed in order to efficiently determine the effective macroscopic parameters of ferroelectric materials. Coupling of the four simulation scales is realized by means of the parameter transfer. Elastic, dielectric and piezo-electric tensors, domain boundary energies and thicknesses calculated by means of DFT and atomistics are used as input and fit parameters in the phase-field simulations (see section 4.3). Subsequently, the results of the phase-field procedure accounting for the domain wall dynamics are used to identify the entry values for the micromechanical model. However, at the current stage of development of the multi-scale simulation chain not all phase-field results can be utilized in the Huber-Fleck model. Hence, input parameters from DFT and shell-model calculations have been utilizes as well. Several different multi-scale coupling schemes are proposed in the present section. They will be evaluated, compared with simulations based on the experimental input parameters and discussed in chapter 5.

4.6.1 Input data from experiments, DFT and atomistic calculations

In the present section we start with the analysis of the experimental, DFT, shell-model and phase-field data available for the micromechanical simulations.

BaTiO$_3$ is one of the most studied ferroelectric materials. Since many experimental results are available for ceramic and single crystal BTO, it is very well suited for the evaluation of the Huber-Fleck model. Unfortunately, no DFT, atomistic and phase-field calculations have been performed on BTO within the project COMFEM, where the focus laid on the PTO and PZT ferroelectrics. Therefore, all calculations on BaTiO$_3$ have been performed using the experimental material constants gathered in [Pertsev 1998] (see Table 4.3), while the spontaneous polarization P^{sp} as well as a longitudinal strain s^{sp} stem from [Landolt 2001].

For the micromechanical modeling of hysteretic behavior the critical energies of 90°-switching G$^{90°}$ and 180°-switching G$^{180°}$ are needed (see details in sections 2.2 and 4.5). These energies have been determined via following procedure. First, an ansatz for the energy released by a switching event has been defined as

$$G^{\alpha} = \boldsymbol{T} \cdot \boldsymbol{\Delta S} + \boldsymbol{E} \cdot \boldsymbol{\Delta P} , \qquad (4.58)$$

where $\boldsymbol{T}$ is the stress tensor, $\Delta \boldsymbol{S}$ is the tensor describing the change of the strain during the switching process, $\boldsymbol{E}$ is the vector of electric field and $\Delta \boldsymbol{P}$ is the vector of the polarization change.

In case of purely electrically loaded bulk ceramics the term $\boldsymbol{T} \cdot \Delta \boldsymbol{S}$ vanishes and the switching energy is directly correlated with the coercive electric field $\boldsymbol{E}_c$, since in the range of $\boldsymbol{E}_c$ most switches occur:

$$G^{\alpha} = \boldsymbol{E}_c \cdot \Delta \boldsymbol{P}^{\max} . \qquad (4.59)$$

Examples of 90° and 180°switching events with maximal energy benefit are depicted in Figure 4.10 a), b).

$$\Delta \boldsymbol{P} = \left(0, 0, \sqrt{2}P^{sp}\right)^T \qquad\qquad \Delta \boldsymbol{P} = \left(0, 0, 2P^{sp}\right)^T$$

a)   b)
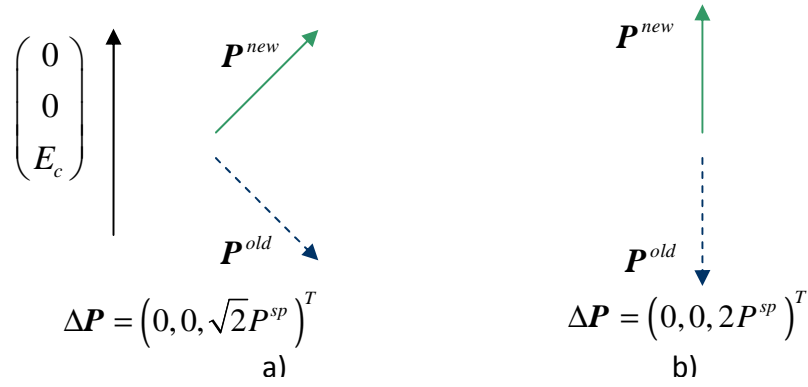
Figure 4.10: 90°- und 180°- switching with highest gain of energy.

From the equation (4.59) and Figure 4.10 the upper limit of the critical switching energies can be estimated as:

$$
\begin{aligned}
G^{90°} &= \sqrt{2}P^{sp}E_c, \\
G^{180°} &= 2P^{sp}E_c.
\end{aligned}
\tag{4.60}
$$

For calculation of $G^{90°}$- und $G^{180°}$- values for BTO, PTO and PZT crystals the strength of the coercive field has been taken to be $E_c = 1$ kV/mm.

Simulation parameters BTO	Experiment
ε_{11}^{S} ( )	1910
ε_{33}^{S}	117
d_{33} (pC/N)	110
d_{31}	-38
d_{15}	407
c_{11}^{E} (GPa)	327
c_{12}^{E}	233
c_{13}^{E}	196
c_{33}^{E}	199
c_{44}^{E}	64.9
c_{66}^{E}	107
P^{sp} (C/m^2)	0.25
s^{sp} (-)	0.01
$G^{90°}$ (MJ/ m^3)	0.35

$G^{180°}$ (MJ/ m^3)		0.5

Table 4.3: Experimental constants for BTO used for simulations.

The material constants for a single-domain PTO crystal have been derived by the project partner FhG-IWM in the framework of the DFT and shell-model calculations (see sections 4.1 and 4.2). They are collected and compared with experimental data in Table 4.4. In the following microme-chanical calculations both theoretical as well as experimental coefficients have been used as input parameters.

Simulation parameters PTO	DFT / shell-model (a)	Experiment
ε_{11}^{S} ( )	53[a]	110 [Pertsev 1998]
ε_{33}^{S}	16[a]	37
d_{33} (pC/N)	122	160
d_{31}	-29	-26
d_{15}	99	56
c_{11}^{E} (GPa)	279	264
c_{12}^{E}	118	149
c_{13}^{E}	83	75
c_{33}^{E}	99	56
c_{44}^{E}	70	77.5
c_{66}^{E}	109	132
P_{sp} (C/m^2)	0.88	0.75
s_{sp} (-)	0.05	0.05 [Landolt 2001]
$G^{90°}$ (MJ/ m^3)		0.7
$G^{180°}$		1

Table 4.4: Comparison of theoretically (DFT, shell-model) as well as experimentally [Pertsev 1998] obtained single-crystal constants used in micromechanical simulations on PTO films and PTO ceramics.

Theoretically derived piezoelectric and elastic constants for PTO are very close to those obtained experimentally (see Table Table 4.4). This means that dynamical processes like, e.g., the domain wall motions, which are always present in the experimental studies but are neglected in the DFT

calculations, are insignificant in PTO for d_{ij} and c_{ij} parameters. Recent investigations concerning the reversible domain wall motion [Jones 2010] have shown that the dynamical domain wall contribution to the effective material constant d_{33}^* can be very weak as well as very strong depending on circumstances. In section 5.4 it will be demonstrated that for PZT, on contrary to PTO, the dynamical contributions coming from the reversible motion of the domain walls have to be taken into account when calculating piezoelectric constants of this material.

The dielectric constants for PTO used in micromechanics have been obtained within the shell-model of atomistic calculations. The data are much smaller than the experimental single-crystal values. Hence, we suppose that the domain wall contribution to ε_{ij} parameters in PTO is considerable.

The material constants of a single domain PZT crystal are collected in Table 4.5. The dielectric constants derived within the shell-model are at least one order of magnitude smaller than experimental values for the bulk crystal. This fact gives a hint that the domain wall contribution to the ε_{ij} coefficients of PZT is significant as well as in the case of PTO. In contrast to the PTO, the experimental material constants for PZT are not available. Hence, according to the work of A. Dent [Dent2007], we utilized the effective polycrystalline dielectric coefficients as single-crystal constants $\varepsilon^{\exp*}$. In contrast to the dielectric parameters, the piezoelectric constants determined by means of DFT are significantly closer to the experimental polycrystal values. Hence, c^{DFT} and d^{DFT} were used as input constants in our calculations.

The piezoelectric constants determined by the phase-field model (see section 4.3) considerably underestimate the DFT- and experimental values: they are more than eight times smaller. The main reason for this deviation is that the corresponding mesoscopic calculations have been performed using the Landau-function of the sixth order only. The more recent tests have shown that the functional of eighth-order yields much better agreement between theoretical and experimental results [Völker 2011].

Simulation parameters PZT	DFT / shell-model (a)	Phase-field	Experimental values for bulk polycrystals used as single-crystal values
ε_{11}^{S} ( )	76[a]		630

ε_{33}^S	18[a]		585
d_{33} (pC/N)	51	6.0	150
d_{31}	-12	-1.14	-20
d_{15}	159	9.4	250
c_{11}^E (GPa)	327		-
c_{12}^E	175		-
c_{13}^E	134		-
c_{33}^E	276		-
c_{44}^E	50		-
c_{66}^E	92		-
P_{sp}	0.58		
s_{sp}	0.015		
$G^{90°}$; $G^{180°}$ (MJ/m^3)	0.7; 1		

Table 4.5: Comparison of intrinsic material constants for PZT obtained in the framework of different theoretical methods.

4.6.2   Linking phase-field simulations and micromechanical modeling

TEM and AFM investigations (see Figure 2.8) have demonstrated that thin film ceramics usually contain two types of domains only. The possible domain configurations for this class of materials have been derived in [Romanov 1999] on an example of (111) thin films (see section 2.4). According to this study the polarization axes of the two domains types exhibit an angle of 90° with respect one to another. Assuming this polarization configuration as a thermodynamically ground state for samples under investigation an extended 2D phase-field model containing three components of polarization, three components of displacement, electric potential as degrees of freedom and a FE-mesh confined to the 2D plane has been developed in cooperation with B. Völker (see Figure 4.11, [Völker 2010]). In the framework of this model material constants needed as input for the micromechanical simulations have been identified according to the description in section 4.3.
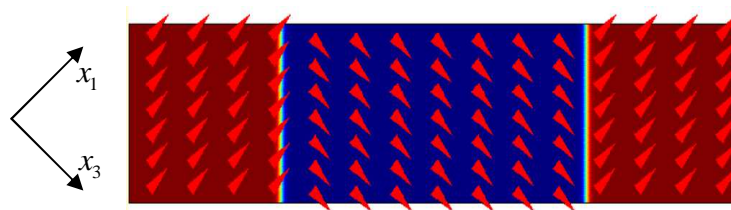
Figure 4.11: Phase-field model of a double-domain structure.

Equations (4.61)-(4.63) give the results of the phase-field modeling for the dielectric $\varepsilon^{PTO,PF}$, the piezoelectric $e^{PTO,PF}$ and the elastic $c^{PTO,PF}$ tensor of a two-domain system. The absolute values of $\varepsilon^{PTO,PF}$ and $c^{PTO,PF}$ tensor elements lie in the range of experimental material constants. The structures of different tensors, however, show considerable deviations.

$$\varepsilon^{PTO,PF} = \begin{pmatrix} 97 & 0 & -73 \\ 0 & 39 & 0 \\ -73 & 0 & 97 \end{pmatrix} \tag{4.61}$$

$$e^{PTO,PF} = \begin{pmatrix} 9.92 & 0.295 & -7.836 & 1.039 & 0 & 0 \\ 0 & 0 & 0 & 0 & 1.094 & 1.094 \\ -7.836 & 0.295 & 9.92 & 1.039 & 0 & 0 \end{pmatrix} \frac{pC}{N} \tag{4.62}$$

$$c^{PTO,PF} = \begin{pmatrix} 2.03 & 1.22 & 2.03 & 0 & 0 & 0 \\ 1.22 & 3.39 & 1.22 & 0 & 0 & 0 \\ 2.03 & 1.22 & 2.03 & 0 & 0 & 0 \\ 0 & 0 & 0 & 0.875 & 0 & 0 \\ 0 & 0 & 0 & 0 & 1.0 & 0 \\ 0 & 0 & 0 & 0 & 0 & 1.0 \end{pmatrix} \cdot 10^{11} \, Pa \tag{4.63}$$

The permeability tensor possesses off-diagonal elements. The reason for their existence is the motion of the domain walls and, hence, microscopic switching of individual grains.

When dipoles in a ferroelectric sample switch their direction, the components of dielectric displacement D_i are composed of two contributions: the linear part D_i^L and the remanent part P_i^R

$$D_i = D_i^L + P_i^R . \tag{4.64}$$

Consequently, the dielectric permeability calculated with the phase-field method is given by

$$\varepsilon_{ij}^{PF} = \frac{\partial D_i}{\partial E_j} = \frac{\partial D_i^L}{\partial E_j} + \frac{\partial P_i^R}{\partial E_j} = \varepsilon_{ij}^L + \frac{\partial P_i^R}{\partial E_j} . \tag{4.65}$$

For the two-domain model depicted in Figure 4.11

$$\varepsilon^L = c^3 \cdot \begin{pmatrix} \varepsilon_{11}^{SM} & 0 & 0 \\ 0 & \varepsilon_{11}^{SM} & 0 \\ 0 & 0 & \varepsilon_{33}^{SM} \end{pmatrix} + c^1 \cdot \begin{pmatrix} \varepsilon_{33}^{SM} & 0 & 0 \\ 0 & \varepsilon_{11}^{SM} & 0 \\ 0 & 0 & \varepsilon_{11}^{SM} \end{pmatrix} , \tag{4.66}$$

where ε_{ij}^{SM} are the dielectric coefficients calculated with the shell-model (see section 4.2), c^1 and c^3 are the volume fractions of the both domains. For small magnitude of the applied electric field c^1 and c^3 can be assessed as $c^1 = c^3 = 0.5$.

Since $P_2 = 0$ in the two-domain model

$$\frac{\partial P_2}{\partial E_i} = 0 \text{ for } i = 1, 2, 3. \tag{4.67}$$

Further, a small variation of $\begin{pmatrix} 0 \\ E_2 \\ 0 \end{pmatrix}$ does not affect domains with $\begin{pmatrix} P_1 \\ 0 \\ 0 \end{pmatrix}$ and $\begin{pmatrix} 0 \\ 0 \\ P_3 \end{pmatrix}$. Hence,

$$\frac{\partial P_1}{\partial E_2} = \frac{\partial P_3}{\partial E_2} = 0. \tag{4.68}$$

Assuming that the domain wall thickness remains unchanged during an infinitesimal domain wall motion, the increase of one domain due to the switching process should be equal to the decrease of another domain:

$$\frac{\partial P_3}{\partial E_1} = -\frac{\partial P_1}{\partial E_1} \text{ and } \frac{\partial P_1}{\partial E_3} = -\frac{\partial P_3}{\partial E_3}. \tag{4.69}$$

With (4.67), (4.68) and (4.69) the non-linear contribution to the permittivity for the discussed two-domain sample reads

$$\frac{\partial \boldsymbol{P}}{\partial \boldsymbol{E}} = \begin{pmatrix} \dfrac{\partial P_1}{\partial E_1} & \dfrac{\partial P_1}{\partial E_2} & \dfrac{\partial P_1}{\partial E_3} \\ \dfrac{\partial P_2}{\partial E_1} & \dfrac{\partial P_2}{\partial E_2} & \dfrac{\partial P_2}{\partial E_3} \\ \dfrac{\partial P_3}{\partial E_1} & \dfrac{\partial P_3}{\partial E_2} & \dfrac{\partial P_3}{\partial E_3} \end{pmatrix} = \begin{pmatrix} \dfrac{\partial P_1}{\partial E_1} & 0 & -\dfrac{\partial P_3}{\partial E_3} \\ 0 & 0 & 0 \\ -\dfrac{\partial P_1}{\partial E_1} & 0 & \dfrac{\partial P_3}{\partial E_3} \end{pmatrix}. \tag{4.70}$$

Introducing equations (4.66) and (4.70) into (4.65) leads to a relationship between the dielectric phase-field- and shell-model-tensors:

$$\varepsilon^{PF} = 0.5 \cdot \begin{pmatrix} \varepsilon_{11}^{SM} & 0 & 0 \\ 0 & \varepsilon_{11}^{SM} & 0 \\ 0 & 0 & \varepsilon_{33}^{SM} \end{pmatrix} + 0.5 \cdot \begin{pmatrix} \varepsilon_{33}^{SM} & 0 & 0 \\ 0 & \varepsilon_{11}^{SM} & 0 \\ 0 & 0 & \varepsilon_{11}^{SM} \end{pmatrix} + \begin{pmatrix} \dfrac{\partial P_1}{\partial E_1} & 0 & -\dfrac{\partial P_3}{\partial E_3} \\ 0 & 0 & 0 \\ -\dfrac{\partial P_1}{\partial E_1} & 0 & \dfrac{\partial P_3}{\partial E_3} \end{pmatrix}. \tag{4.71}$$

Now, relation (4.71) allows to extract the contributions of the domain wall motion to the dielectric constants $\frac{\partial P_1}{\partial E_1}$ and $\frac{\partial P_3}{\partial E_3}$. In the above described two-domain model these contributions for PTO are equal

$$\left(\frac{\partial P_1}{\partial E_1}\right)^{PTO} = \left(\frac{\partial P_3}{\partial E_3}\right)^{PTO} = 73.\tag{4.72}$$

In reality the two contributions might be different.

The relationship between the results of DFT- and phase-field description of piezoelectric tensors can be obtained in a similar manner:

$$\boldsymbol{d}^{PF} = 0.5 \cdot \begin{pmatrix} 0 & 0 & 0 & 0 & d_{15}^{DFT} & 0 \\ 0 & 0 & 0 & d_{15}^{DFT} & 0 & 0 \\ d_{31}^{DFT} & d_{31}^{DFT} & d_{33}^{DFT} & 0 & 0 & 0 \end{pmatrix} +$$

$$+ 0.5 \cdot \begin{pmatrix} d_{31}^{DFT} & d_{31}^{DFT} & d_{33}^{DFT} & 0 & 0 & 0 \\ 0 & 0 & 0 & 0 & 0 & d_{15}^{DFT} \\ 0 & 0 & 0 & 0 & d_{15}^{DFT} & 0 \end{pmatrix} + \tag{4.73}$$

$$+ \begin{pmatrix} \dfrac{\partial S_1}{\partial E_1} & 0 & -\dfrac{\partial S_3}{\partial E_3} & 0 & 0 & 0 \\ 0 & 0 & 0 & 0 & 0 & 0 \\ -\dfrac{\partial S_1}{\partial E_1} & 0 & \dfrac{\partial S_3}{\partial E_3} & 0 & 0 & 0 \end{pmatrix}.$$

Via this ansatz the contribution of the domain wall motion to the piezoelectric constants $\frac{\partial S_1}{\partial E_1}$ and $\frac{\partial S_3}{\partial E_3}$ can be separated.

Tensor $\boldsymbol{d}^{PF}$ has to be estimated from (4.62) and (4.63) according to (2.7) as

$$\boldsymbol{d}^{PF} = \left(\boldsymbol{c}^{PF}\right)^{-1} \boldsymbol{e}^{PF}.\tag{4.74}$$

However, $\boldsymbol{c}^{PTO,PF}$ has a vanishing determinant. Consequently, the tensor $\boldsymbol{c}^{PTO,PF}$ is not invertible. The reason for such a behavior is hidden in the vanishing stiffness of the idealistic two-domain configuration during shear deformation in the $y_1 - y_2$-plane (see Figure 4.12). The corresponding shear stress is almost completely released by the domain wall motion in y_1-direction. Incorporation of defects or charged impurities into the model might lead to more

realistic results with a finite stress during shearing. However, an appropriate theoretical description is not yet available.
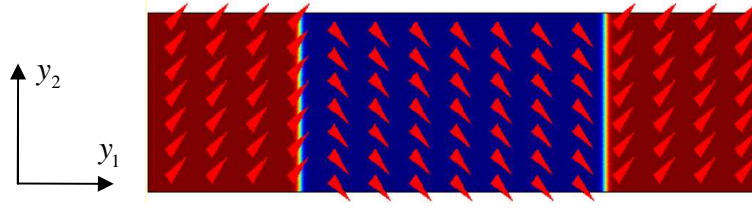

Figure 4.12: Shear leading to practically resistance-less motion of the domain walls.

To eliminate this problem several approaches can be applied. One possibility would be a direct introduction of the intrinsic constant from the DFT or atomistic calculations. Such a procedure can be motivated by the similarities between the experimental and DFT simulated c and d tensors (see section 4.6.1). However, the dielectric constants obtained by the shell-model are significantly lower than the corresponding experimental single-crystal values. Hence, another possibility is to perform a mixed multi-scaling analysis by introduction into the micromechanical calculations the piezo- and elasticity constants stemming from the DFT calculations together with the permeability tensor obtained in the phase-field scheme.

Referring to the latter approach two different possibilities are proposed in the present thesis. For linear calculations of polycrystal consisting of single-domain grains we propose to use the ε^{PF} tensor as it comes out of the phase-field calculations. For Huber-Fleck calculations, in contrast, new single-crystal dielectric constants ε_{11}^{PF*} and ε_{33}^{PF*} have to be defined. According to the ansatz (4.65), these constants are assumed to be a sum of dielectric parameters obtained within the atomistic shell-model ε_{11}^{PF*} and ε_{33}^{PF*} and the domain wall contributions $\dfrac{\partial P_1}{\partial E_1}$ and $\dfrac{\partial P_3}{\partial E_3}$ coming from the phase-field approach.

$$\varepsilon_{11}^{PF*} = \varepsilon_{11}^{SM} + \frac{\partial P_1}{\partial E_1},$$

$$\varepsilon_{33}^{PF*} = \varepsilon_{33}^{SM} + \frac{\partial P_3}{\partial E_3}.$$

(4.75)

In the case of PTO one gets

$$\varepsilon_{11}^{PF*,PTO} = 126,$$

$$\varepsilon_{33}^{PF*,PTO} = 89.$$

(4.76)

The first constant in equation (4.76) lies very close to experimentally determined single-crystal values 110 [Pertsev 1998] und 115 [Gavrilyachenko 1971]. The second matrix element $\varepsilon_{33}^{PTO,PF*}$

obtained with this procedure overestimates the corresponding experimental data 37 [Pertsev 1998] and 51 [Gavrilyachenko 1971].

The complete dielectric tensor resulting from the phase-field calculations for the two-domain PZT-model reads

$$\varepsilon^{PZT,PF} = \begin{pmatrix} 407 & 0 & -372 \\ 0 & 42 & 0 \\ -372 & 0 & 407 \end{pmatrix}. \tag{4.77}$$

According to the relation (4.71), the domain wall contributions for PZT can be estimated as

$$\left(\frac{\partial P_1}{\partial E_1} \right)^{PZT} = \left(\frac{\partial P_3}{\partial E_3} \right)^{PZT} = 372. \tag{4.78}$$

This value is considerably higher than that of PTO. Using (4.78) and the shell-model results (see Table 4.5) we obtain with (4.75)

$$\begin{aligned} \varepsilon_{11}^{PZT,PF*} &= 448, \\ \varepsilon_{33}^{PZT,PF*} &= 390. \end{aligned} \tag{4.79}$$

The elasticity tensor calculated by means of the phase-field model for PZT is, similarly to PTO, singular. For that reason it is not possible to determine the piezoelectric d tensor as well as corresponding domain wall contributions $\dfrac{\partial S_1}{\partial E_1}$ and $\dfrac{\partial S_3}{\partial E_3}$:

$$c^{PZT,PF} = \begin{pmatrix} 2.285 & 1.082 & 2.284 & 0 & 0 & 0 \\ 1.082 & 3.636 & 1.082 & 0 & 0 & 0 \\ 2.284 & 1.082 & 2.285 & 0 & 0 & 0 \\ 0 & 0 & 0 & 0.936 & 0 & 0 \\ 0 & 0 & 0 & 0 & 0.8335 & 0 \\ 0 & 0 & 0 & 0 & 0 & 0.8335 \end{pmatrix} \cdot 10^{11} \, Pa, \tag{4.80}$$

$$e^{PZT,PF} = \begin{pmatrix} 21.528 & 0.114 & -20.425 & 0.383 & 0 & 0 \\ 0 & 0 & 0 & 0 & 0.395 & 0.395 \\ -20.425 & 0.114 & 21.528 & 0.383 & 0 & 0 \end{pmatrix}. \tag{4.81}$$

Material data presented in section 4.6 partly differs from that published in [Völker 2010]. One reason for this deviation is usage of different coordinate systems. A further reason is origination of material data from distinct development stages of project partners. Meanwhile in [Völker 2010] the latest results from DFT, shell-model and phase-field simulations could be published, the micromechanical calculations, which were developed simultaneously to the nano-scale

models, used the preliminary material constants from a previous development stage. Due to the time restriction of the project COMFEM, the repetition of all micromechanical simulations with latest material data was not possible and, considering practical benefit, not reasonable.

5 Simulation results

5.1 Setup of micromechanical simulations

The microstructural evolution and electromechanical behavior of polycrystalline materials can be successfully studied in the framework of micromechanical simulations. While the micromechanical simulations of bulk grained structures is a well developed area of scientific research, the literature on micromechanical simulations of thin ceramic films is very limited. To make a first step along this line we explore two different possibilities: the non-linear simulations according to the so-called Huber-Fleck procedure (see section 4.5), and a linear FE-model (see equations (4.35)), where the polarizations are oriented according to "the model of least angle" (see Figure 4.8). The variety of input parameters utilized in both simulation methods are summarized in Table 5.1.

Material	Input data for single-crystal constants					
	Linear piezoelectric				Huber-Fleck	
BTO	$c^{Exp}, d^{Exp}, \varepsilon^{Exp}$				$c^{Exp}, d^{Exp}, \varepsilon^{Exp}$	
PTO	$c^{Exp}, d^{Exp}, \varepsilon^{Exp}$ $\quad$ $c^{DFT}, d^{DFT}, \varepsilon^{SM}$	$c^{DFT}, d^{DFT}, \varepsilon^{PF}$	$c^{DFT}, d^{DFT}, \varepsilon^{PF*}$		$c^{Exp}, d^{Exp}, \varepsilon^{Exp}$	$c^{DFT}, d^{DFT}, \varepsilon^{SM}$
PZT	$c^{DFT}, d^{DFT}, \varepsilon^{SM}$	$c^{DFT}, d^{DFT}, \varepsilon^{PF}$	$c^{DFT}, d^{DFT}, \varepsilon^{PF*}$		$c^{DFT}, d^{DFT}, \varepsilon^{SM}$	

**Table 5.1: Overview of the performed calculations and corresponding input parameters.**

The following sections document preparatory investigations necessary for the setup of micromechanical simulations on ceramic materials. Here, such interesting and so far non-treated questions as the influence of the grain shape on the results of non-linear Huber-Fleck calculations will be discussed.

5.1.1 Influence of the boundary conditions

Different kinds of boundary conditions have been investigated in the present work. For the bulk structures the condition "$T = 0$ at the sample surface" (see Figure 5.1 a) has been compared with periodic boundary conditions in three directions (see Figure 5.1 b):
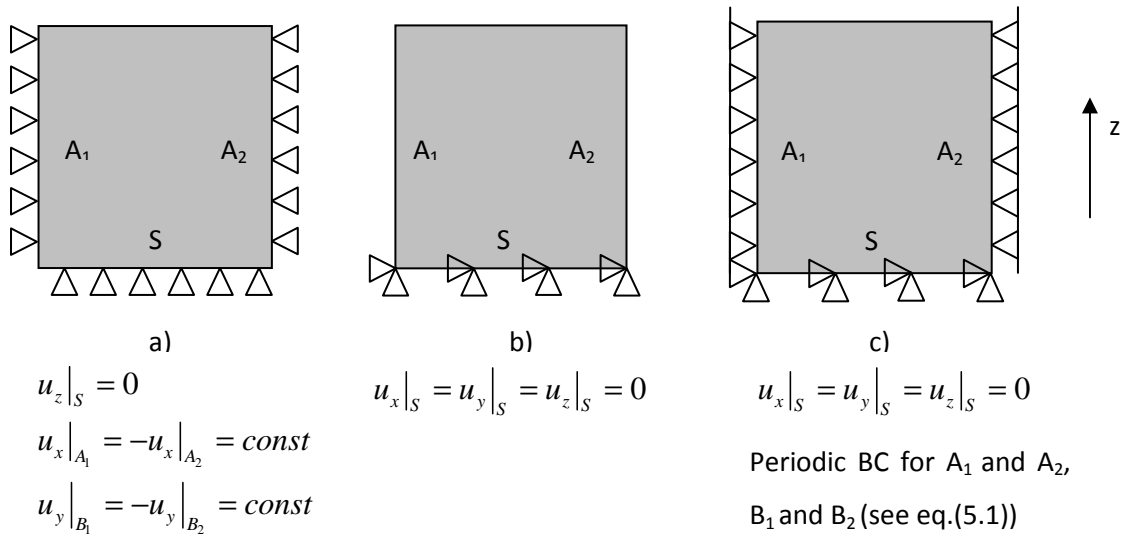
$$u_x^i - u_x^{i+1} = u_x^j - u_x^{j+1}$$
$$u_y^i = u_y^{i+1} \tag{5.1}$$
$$u_z^i = u_z^{i+1}.$$

For the calculated effective dielectric and piezoelectric coefficients no differences between two boundary condition types have been found. The most calculations on bulk structures were performed with boundary conditions from Figure 5.1 a.
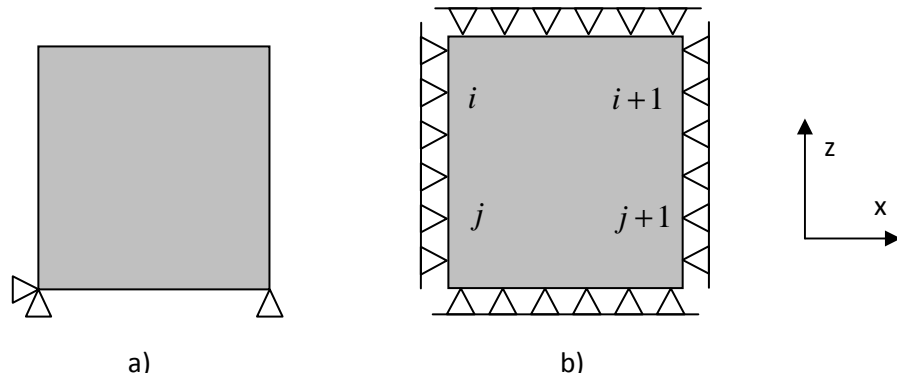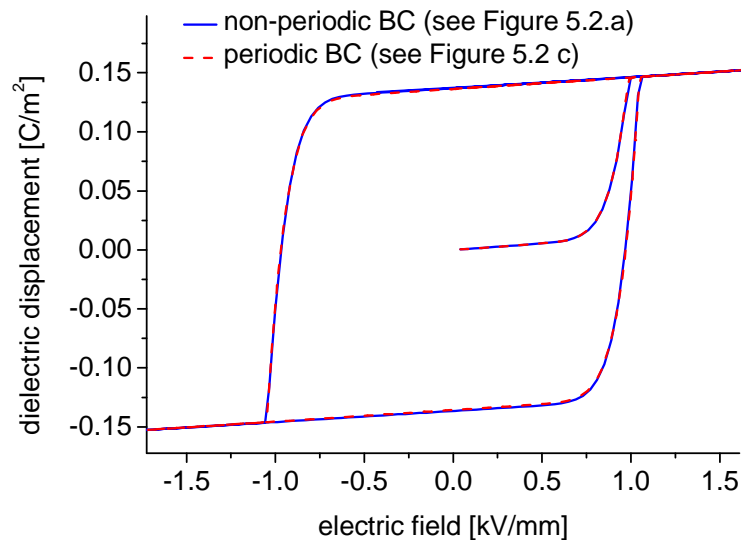

Figure 5.1: Two types of boundary conditions for the modeling of bulk materials: a) stress-free at the sample surface; b) periodic boundary conditions in three directions.

For the thin film structures three different possibilities of clamping depicted in Figure 5.2 have been tested. Linear as well as non-linear calculations demonstrate equal behavior for the clamping cases a and c from Figure 5.2 as shown in Figure 5.3. Results obtained with boundary conditions as shown in Figure 5.2 b offer non-realistic deformations at the free sample edges, which are perpendicular to the substrate. This finding is consistent with results obtained in [Zalachas 2008]. In thin film simulations boundary conditions from Figure 5.2 a) were utilized. Additionally, due to the different coefficients of thermal expansion for substrate and thin film materials a non-zero strain at the boundaries and so a tensile stress parallel to the substrate is applied.

a)

$$u_z\big|_S = 0$$

$$u_x\big|_{A_1} = -u_x\big|_{A_2} = const$$

$$u_y\big|_{B_1} = -u_y\big|_{B_2} = const$$

b)

$$u_x\big|_S = u_y\big|_S = u_z\big|_S = 0$$

c)

$$u_x\big|_S = u_y\big|_S = u_z\big|_S = 0$$

Periodic BC for A_1 and A_2,
B_1 and B_2 (see eq.(5.1))

Figure 5.2: Three types of boundary conditions for the modeling of thin polycrystalline films, boundaries B_1 and B_2 are parallel to the drawing plane:

a) Displacements in z-direction at the sample-substrate interface as well as in x- and y-directions of the sample edges perpendicular to the substrate are fixed;

b) Displacements at the substrate-sample interface only are fixed (has been proven to be inapplicable);

c) All displacements at the sample-substrate interface are fixed, periodic boundary conditions at the sample edges which are perpendicular to the substrate.

Figure 5.3: Influence of the periodic boundary conditions on the ferroelectric hysteresis of a (111)-textured thin film with two types of boundary conditions.

Figure 5.4 shows the influence of the above described clamping (Figure 5.2 a) on the simulated strain hysteresis for a BTO sample. The curve corresponding to the clamped sample becomes flatter and the low-signal-d_{33}^* smaller. This result is obvious as the clamped sample is restricted to contract in the plane parallel to the substrate. This contraction is, however, necessary for a

101

large deformation in the direction perpendicular to the substrate as in the case of the non-clamped bulk samples.
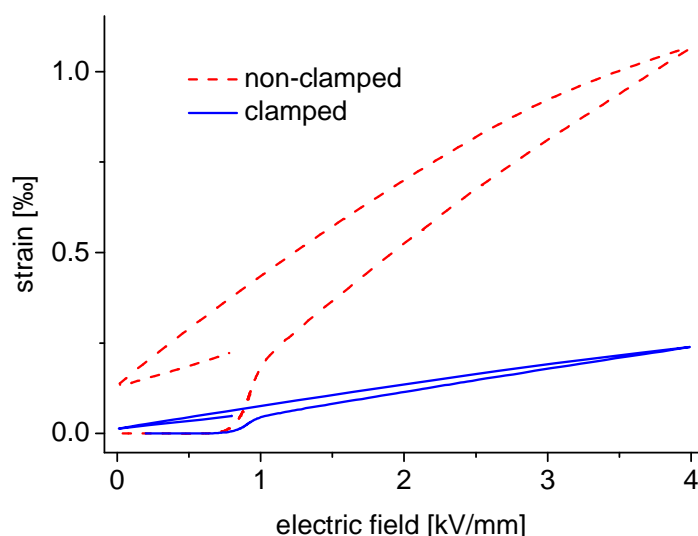

Figure 5.4: The effect of the clamping on the strain hysteresis on an example of a BTO sample.

5.1.2 Creep parameter and direction of loading

The creep parameter n of the Huber-Fleck model defines alongside with the critical switching energy the activity of a switching process (see section 4.5). In [Pathak 2008] the creep constant $n = 50$ has been used for a hypothetic model of polycrystal. In the present work we were able to show that many physical properties like ferroelectric and ferroelastic response in the range between $n = 10$ and $n = 50$ are almost identical, while for $n < 10$ significant changes occur as shown in Figure 5.5. Hence, in our simulations the creep parameter $n = 10$ has been utilized. This finding permits to achieve a strong reduction of computational time without loss of the reliability of results.
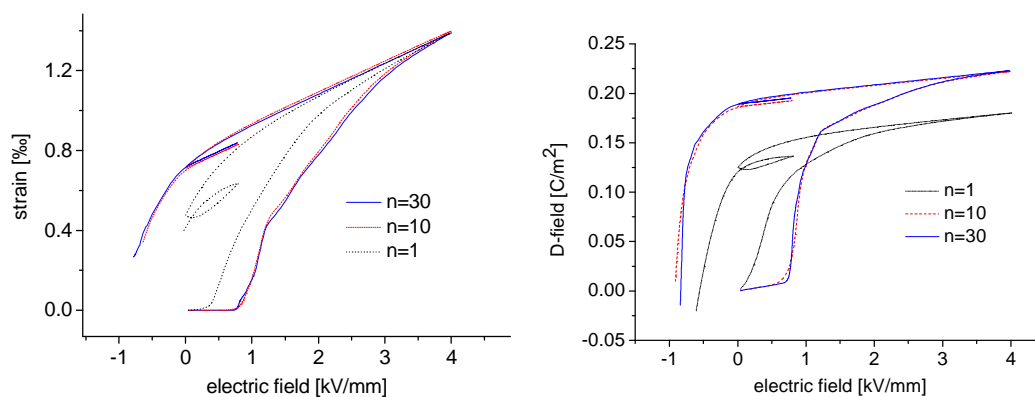

Figure 5.5: Influence of the creep parameter on the strain and the dielectric field as a function of applied electric field for an unclamped BTO.

102

Additionally, the influence of the direction of electrical loading can be clearly seen in Figure 5.5. The slope of curves in the range of zero electric field depends on the sign of the field gradient: for $\nabla E < 0$ before achieving the remanent point at $E = 0 \dfrac{kV}{mm}$ the slope is higher than for $\nabla E > 0$ after achieving the remanence. The effective macroscopic constants have been determined from the latter slope.

5.1.3 Influence of the number of grains in the volume element

In order to ensure the reliability of results the influence of the grain number used in our micro-mechanical simulations has to be investigated. The effect of the number of different grain orientations in the representative volume element on the results of the calculations has been studied in the present work for several idealized samples. Two examples of structures with different grain number are given in Figure 5.6, while the polarization and strain hysteresis curves are shown in Figure 5.7. Resulting material parameters are collected in Table 5.2. The effective dielectric and piezoelectric constants as well as remanent polarization of a clamped and un-clamped 16- and 100-grain model do not show any significant differences. Merely the remanent strain of the 100-grain unclamped model is smaller than that of the unclamped 16-grain model. For the clamped thin film, however, this value is identical in samples with different grain density. Therefore, for the sake of reduction of the CPU time the most simulations has been performed on the basis of the smaller model, while in critical cases the results have been checked on the 100-grain sample.

At first glance the sufficient statistical weight of polarization distribution for a sample consisting of 16 grains might seem surprising. One has, however, to keep in mind that each grain consists of at least five finite elements, and that each element allows for six polarization orientations. As these orientations multiplied with domain volume fraction can be combined to any orientation of the element (see equation (4.54)) the entire sample containing at least 80 elements, in turn, possesses a big manifold of polarization directions. Therefore, in total one gets a representative sample of a polycrystal with a model consisting of 16 grains only.
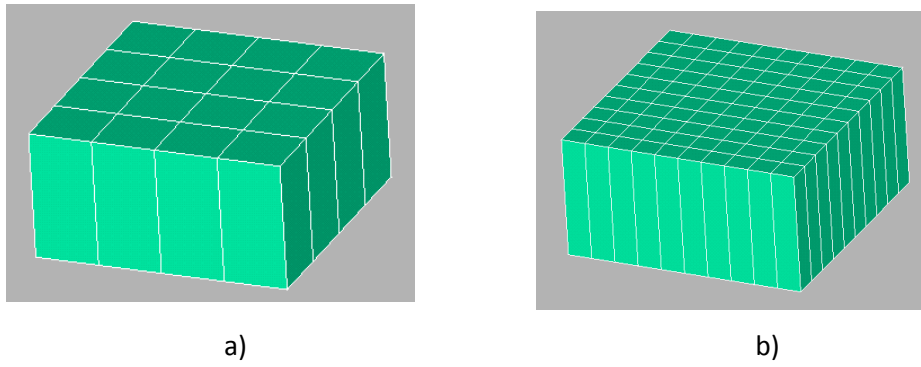
a)   b)

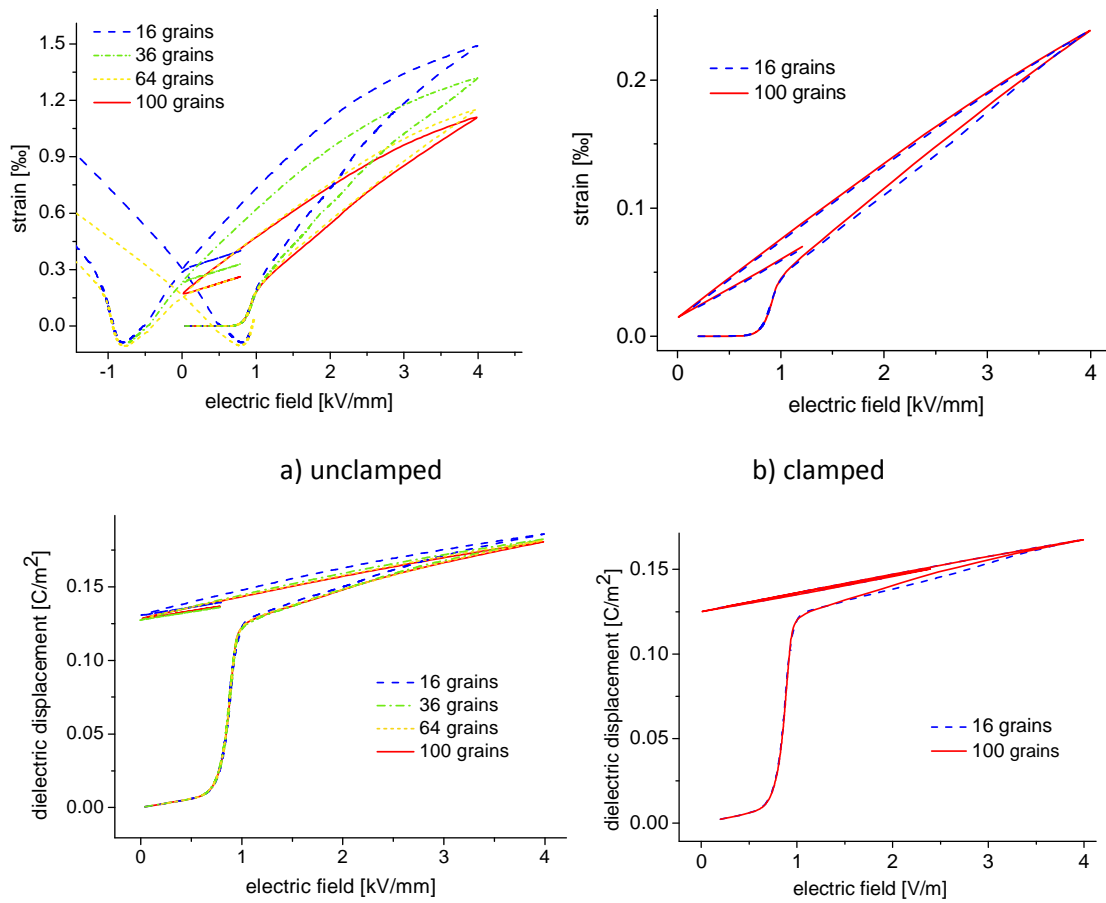**Figure 5.6: Polycrystalline models: a) 16 columnar grains; b) 100 columnar grains.**

a) unclamped   b) clamped

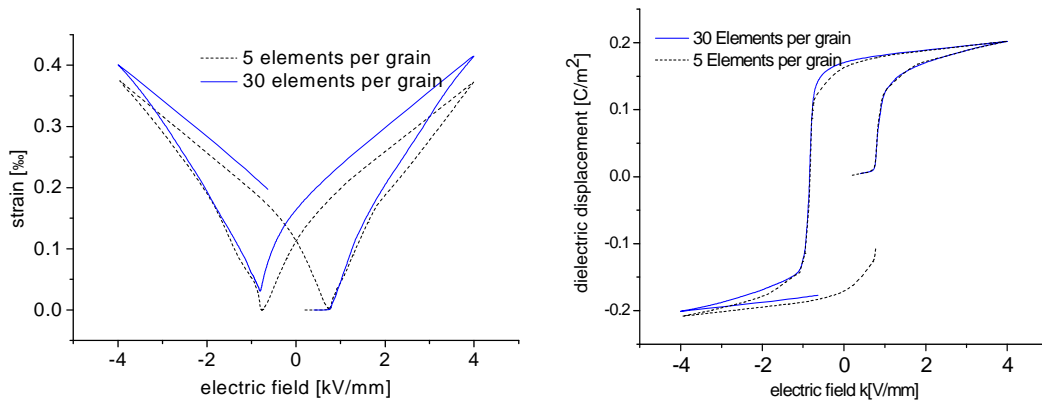**Figure 5.7: Polarization- and strain-hysteresis of several BTO samples with different number of grains.**

	16 columnar grains		100 columnar grains	
	unclamped	clamped	unclamped	clamped
ε_{33}^{*} (-)	1240	1140	1230	1140
d_{33}^{*} (pC/N)	124	45	122	45
P^{rem} (C/m^2)	0.13	0.12	0.13	0.12
s^{rem} (-)	0.3	0.01	0.17	0.01

5.1.4 Influence of the mesh size

Another important parameter for the quality of the micromechanical calculations, apart from the number of grains with different crystal orientations in a sample, is given by the number of finite elements in each grain. The influence of the mesh size is discussed on the example of clamped thin films shown in Figure 5.8 and Table 5.3. A somewhat considerable deviation between the coarse- and fine-meshed samples has been found only for values of the remanent strain. Apart from that the deviations were less than 12%, which permits us to use the coarse mesh for determination of dielectric and piezoelectric constants as well as remanent polarization without loss of accuracy but with a great gain in the computational efforts. One possible reason for the differences in physical parameters calculated on the basis of models with fine- and coarse meshing is the first degree of polynomials used as shape functions for nodal displacements and electric potentials in the FEAP implementation of the Huber-Fleck law.


Figure 5.8: Polarization- and strain hysteresis curves calculated for a clamped BTO thin film consisting of 16 columnar grains.

	5 elements per grain	30 elements per grain
ε_{33}^{*} (-)	890	800
d_{33}^{*} (pC/N)	55	58
P^{rem} (C/m^2)	0.16	0.17
s^{rem} (-)	0.110	0.160

Table 5.3: Comparison of the effective dielectric and piezoelectric constants as well as remanent polarization and strain of two clamped BTO samples with coarse- (5 elements per grain) and fine-meshing (30 elements per grain).

Calculations with the linear piezoelectric model with "least angle" polarizations (see equations (4.35) and Figure 4.8 in section 4.4) have been performed by means of the software ANSYS. Since the linear model is numerically very fast, polynomials of second degree used as shape functions for degrees of freedom and a fine meshing (more than 30 elements per grain) could been utilized in ANSYS calculations. The deviations for effective dielectric and piezoelectric coefficients obtained with different mesh densities are negligible (<1%) in these calculations (see Figure 5.9).
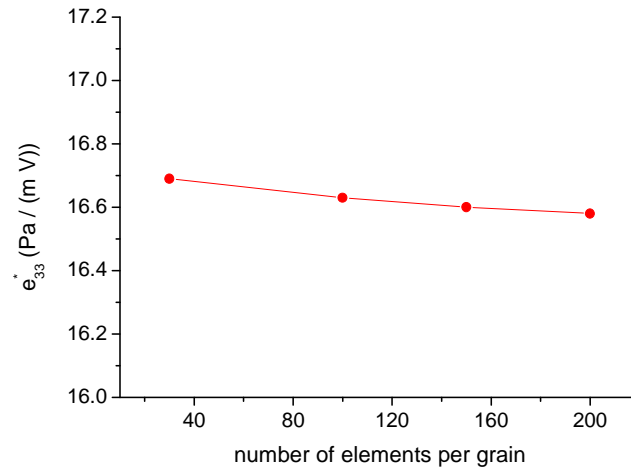

Figure 5.9: Influence of the mesh size on the piezoelectric constant e_{33}^{*} within the linear piezoelectric model with "least angle" polarizations performed within the ANSYS package.

5.1.5 Effects of the realization of crystal orientations in a polycrystal

The distribution of orientations of crystallites in a polycrystal is typically random. In our simulations a standard uniform random number generator has been used to ensure the arbitrariness of the orientation realization. In the following we check whether the generated realization influences the results of calculations. Two different realizations of ensembles of 16 crystallites are shown in Figure 5.10. Here, each green multi-arm represents the occupied polarization directions. The arm lengths correspond to the domain volume fractions c^I (see section 4.5). The polarization and strain hysteresis curves of three different orientations realizations are depicted in Figure 5.11. The three curves in both cases are almost identical. It means that in the framework of Huber-Fleck calculations already 16-grain samples give a representative statistics of polarization orientations.
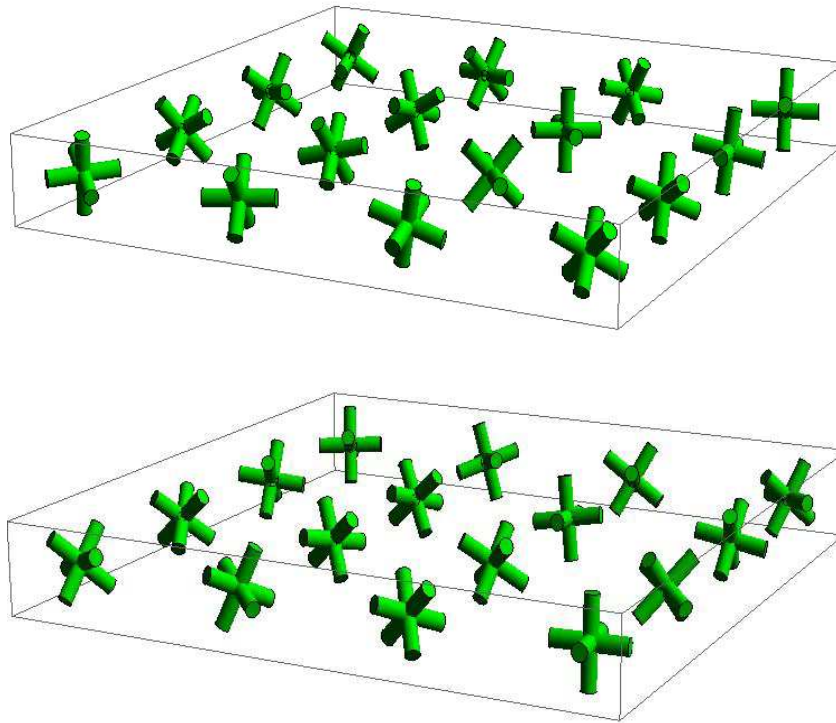
Figure 5.10: Two realization of orientation of crystallites in a polycrystal consisting of 16 grains.
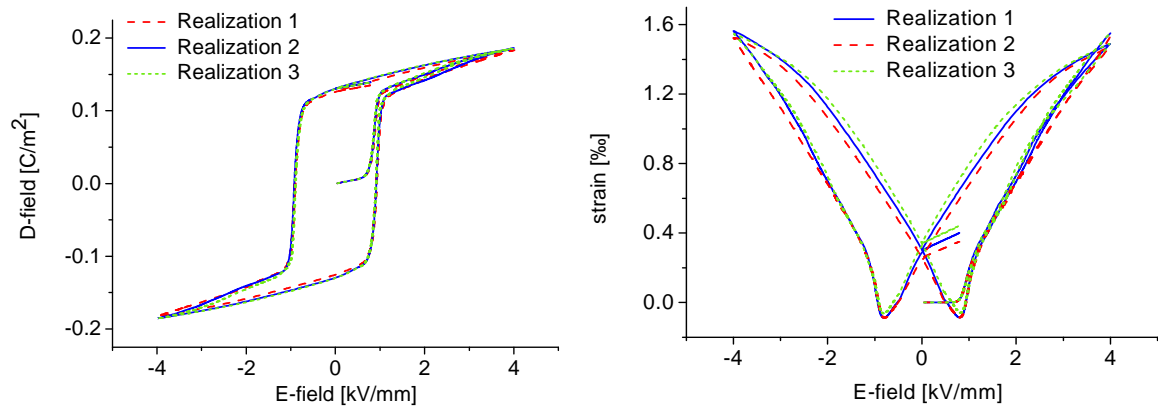
Figure 5.11: Polarization and strain hysteresis of three different realizations of a BTO sample consisting of 16 crystallites.

5.1.6 Effect of the texture

The polarization hysteresis of a texture free and a (111)-textured polycrystal are compared in Figure 5.12. The slope of the hysteresis curve for the perfectly (111)-textured sample shows drastic changes with respect to that of the untextured one. The change of the direction of loading close to remanence in the texture-free model leads to the change of the slope gradient. In the perfect (111) texture, in contrast, the change of the loading direction does not influence the shape of the hysteresis curve at remanence. Moreover, the ferroelastic hysteresis of an exactly (111)-textured sample is linear and hysteresis free as shown in Figure 5.13, because the allowed

90° and 180° domain processes (tetragonal phase) do not change the remanent strain for this structure.

In order to show the influence of the non-perfect (111) fiber texture, which is closer to reality, a random uniform deviation from the perfect texture of maximal 10° has been introduced in the model. Consequently, the hysteresis becomes softer (see Figure 5.14).
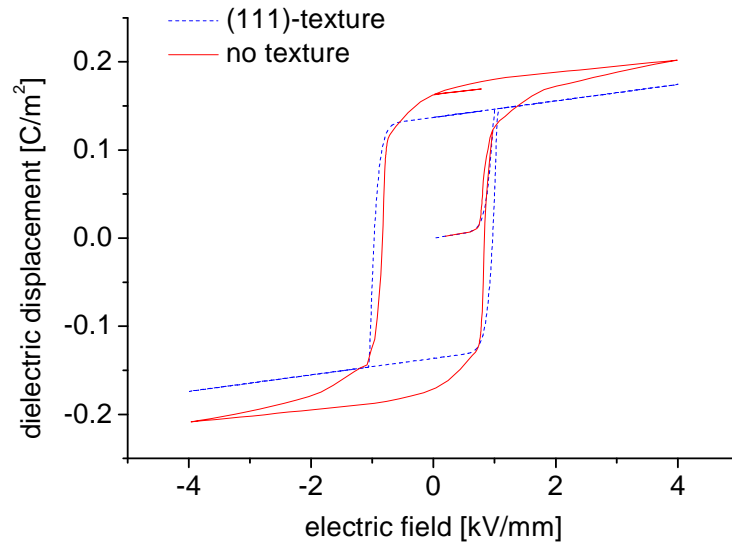

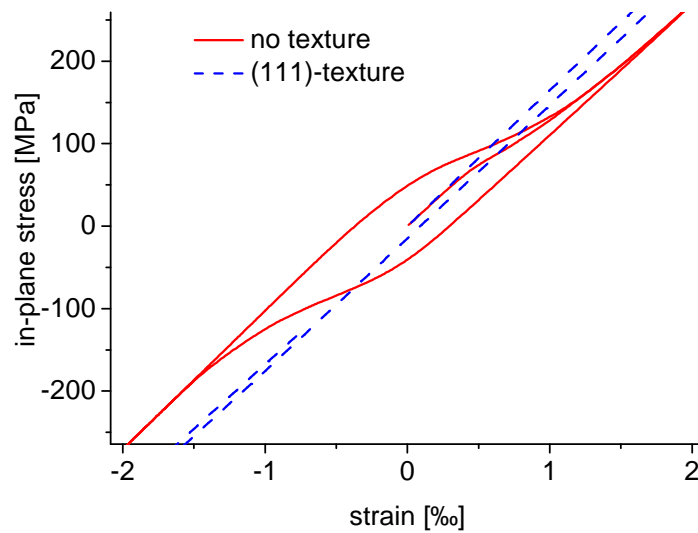**Figure 5.12: Influence of the texture on the polarization hysteresis.**

Figure 5.13: Comparison of the ferroelastic hysteresis of a texture free and a (111)-textured model.
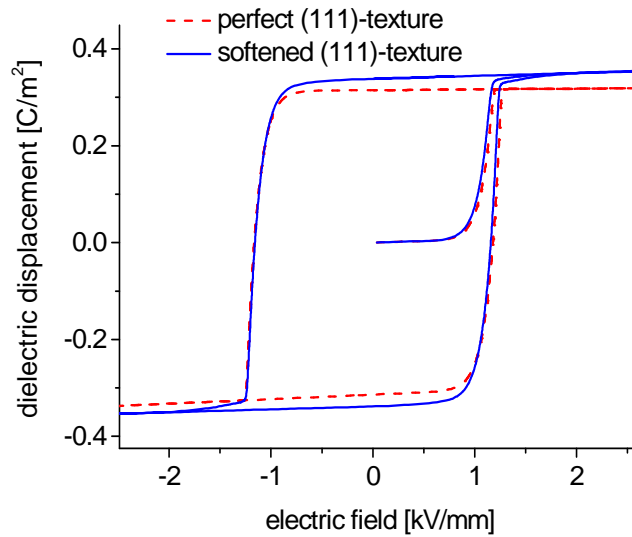
Figure 5.14: Influence of the texture accuracy on the shape of the hysteresis curve.

5.1.7 Influence of the spontaneous strain

The impact of the spontaneous strain on the ferroelectric as well as ferroelastic hysteresis curves is shown in Figure 5.15 and Figure 5.16. Under electrical loading (Figure 5.15) remanent strain and polarization of a sample with smaller spontaneous strain are higher than the corresponding parameters of a model with larger spontaneous strain. In contrast, under mechanical loading (Figure 5.16) remanent strain of a sample with smaller spontaneous strain is less than the corresponding value of a model with larger spontaneous strain. Results of this sort can be used to design materials with desired properties.
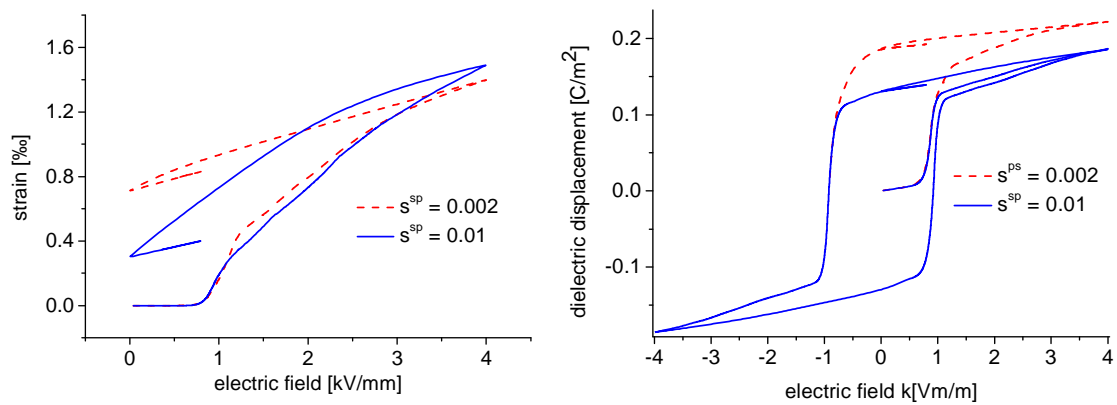

Figure 5.15: Influence of the strength of spontaneous polarization on the strain on an example of an unclamped BTO sample.
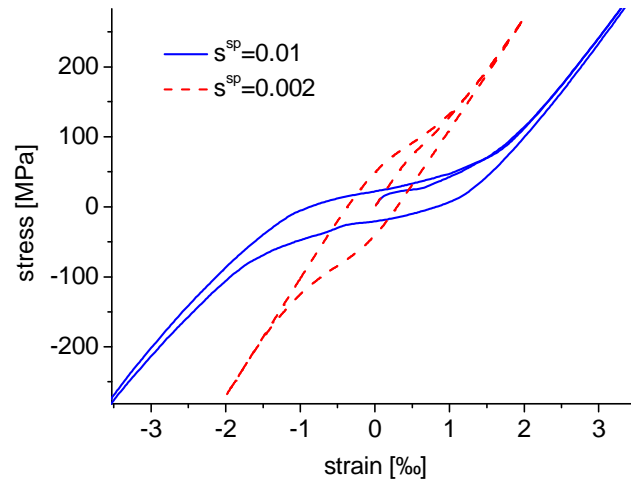
Figure 5.16: Stress-strain correlation for an unclamped BTO sample.

5.1.8 Effect of the grain shape

An essential question is how the modeled hysteretic properties of the ceramics depend on the grain shape. To address this issue the polarization and strain hysteresis of three polycrystalline samples with different grain shape (see Figure 5.17) have been calculated. They are compared in Figure 5.18, while the corresponding effective material constants are summarized in Table 5.4. The hysteresis curves as well as the calculated coefficients do not show any significant dependence on the grain shape. This result is consistent with previous investigations within alternative theoretical methods [Dunn 1995], [Qui 1991] and [Nan 1996]. One possible reason for this finding is the fact that no special physical properties were assigned to the grain boundaries beyond different lattice orientations of the adjacent grains.
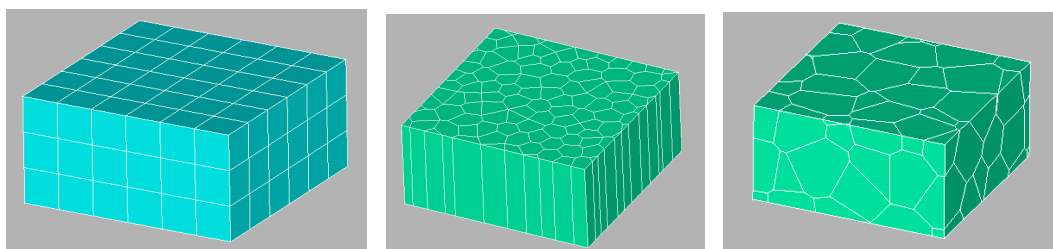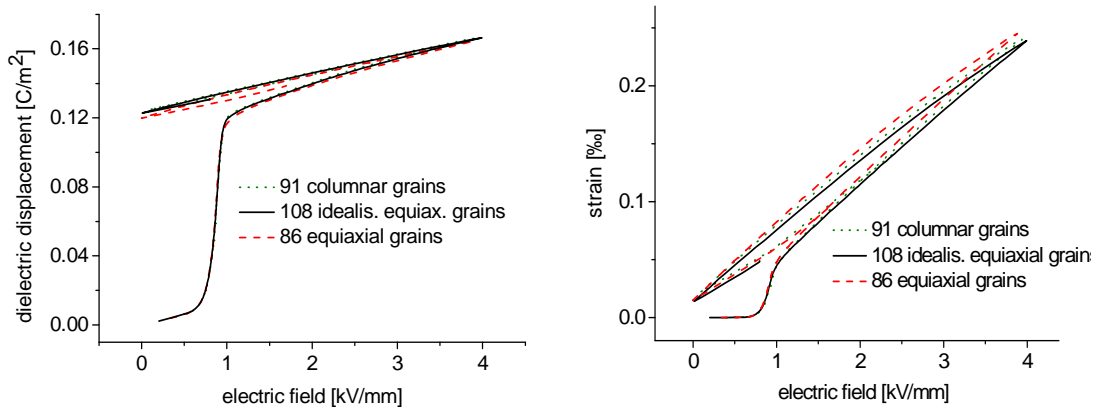

| a) 108 idealized equiaxial grains | b) 91 realistic columnar grains | c) 86 realistic equiaxial grains |

Figure 5.17: Models of polycrystals with different grain shapes.

Figure 5.18: Influence of the grain shape on the hysteretic properties of polycrystals.

BaTiO$_3$	108 idealized equiaxial grains	84 realistic equiaxial grains	91 realistic columnar grains
ε_{33}^{*} (-)	1150	1140	1130
d_{33}^{*} (pC/N)	44	44	43

Table 5.4: Comparison of effective material constants of three polycrystals with different grain shape. The studied shapes are presented in Figure 5.17.

5.2   Investigations of BaTiO$_3$

5.2.1   Bulk crystal

The effective material tensors of a polycrystal are determined by the polarization distribution of individual grains. Therefore, the domain volume fractions, describing the occupation of domains polarized in different directions within the Huber-Fleck model, are one of the most important characteristics of a ferroelectric polycrystal. In an unpoled polycrystal the configuration of polarization is known: all domain types are more or less equally occupied. Hence, the "least angle" model as well as Huber-Fleck calculations provides similar dielectric constant, comparable to the experimental value (see Table 5.5). The piezoelectric coefficients of an unpoled ceramic are equal zero.

| BaTiO$_3$ bulk | Present work | | Method of eff. piezoel. medium (Pertsev 1998) | | Experimental results |
	"Least angle"	Huber-Fleck	$P^{rem}/P^{sp}=0.8$	$P^{rem}/P^{sp}=0.5$	
ε_{33}^* (unpoled)(-)	1300	1300±60	-	-	1400
ε_{33}^* (-)	490±3	1240	800	1300±100	1420 [Jaffe 1958]
d_{33}^* (pC/N)	117±1	120	110±10	110±10	190 [Jaffe 1958] 130 [Bechmann1966]
P^{rem} (C/m^2)	0.8 P^{sp}=0.19	0.5 P^{sp}=0.12	-	-	0.08 [Jaffe 1958]

Table 5.5: Comparison of the material constants of bulk BTO calculated within different theoretical methods and obtained experimentally.

 In a poled state the configuration of domains is not generally known: different theoretical models propose miscellaneous ensembles of polarizations. A typical configuration of polarizations for an unclamped (bulk) BTO sample at remanence calculated within the Huber-Fleck-Model is shown in Figure 5.19. Since only six orthogonal polarization directions are allowed in each grain there is no possibility to completely align the polarization of a polycrystal in the direction of the applied electric field (z-axis). Nevertheless, it is expected that at high strength of electric field close to the saturation the grains will be polarized along the directions making the smallest possible angle with the z-axis. Furthermore, within the so-called model of the "least angle" a similar polarization configuration is expected to persist in the remanent state. Figure 5.19 demonstrates, however, that some domains exist which are oriented at rather large angle or even perpendicular to the applied electric field in the saturated as well as in the remanent state. The physical reason for this phenomenon is probably the complex electromechanical interaction between the multi-domain grains yielding the state of minimal energy. Due to this nontrivial distribution of polarizations the large single-crystal dielectric constant ε_{11}=1910 significantly contributes to the effective dielectric constant ε_{33}^*. Consequently, the results obtained within the Huber-Fleck procedure (ε_{33}^*(Huber-Fleck) = 1240) are much closer to experimental value (ε_{33}^*(experiment) = 1400) than that of the model of the least angle (ε_{33}^*(least angle) = 490) as shown in Table 5.5.

The difference in the polarization configurations of the poled state for the above described two models becomes clearer after statistical analysis in Figure 5.20. The average value of the normalized polarizations P_z/P^{sp} in the "least angle" model equals approximately 0.8 for the remanent state, while the same quantity calculated in the framework of the Huber-Fleck-scheme is about

0.5. In the present work these values have been identified as the normalized remanent polarization. The Huber-Fleck result is significantly closer to the experimental magnitude of remanent polarization than the corresponding "least angle" outcome (see Table 5.5).
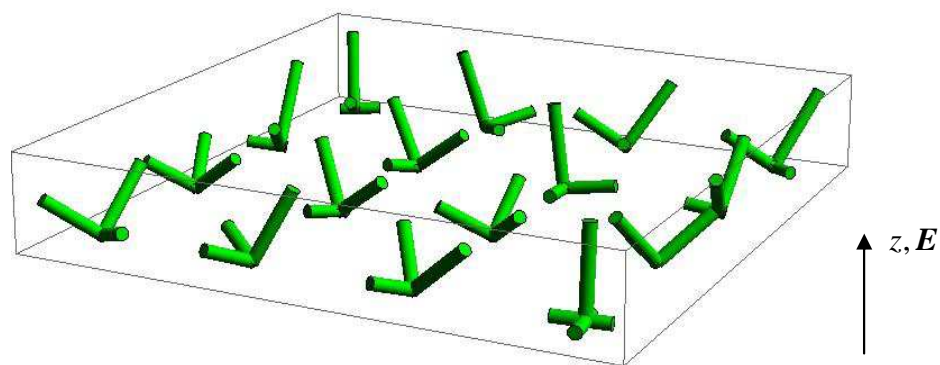
a) saturated state
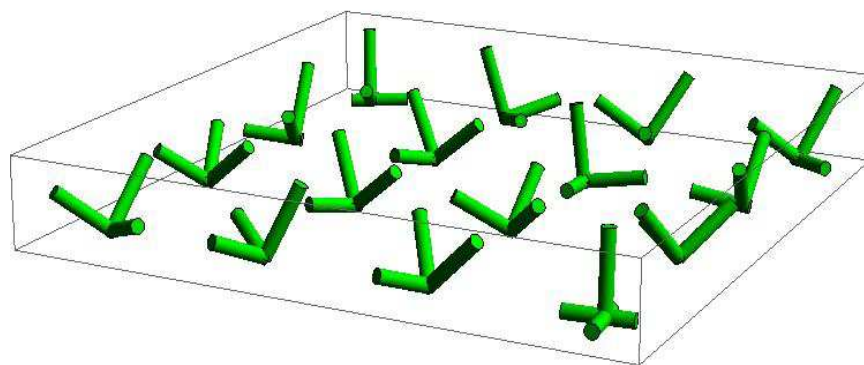
b) remanent state

Figure 5.19: Configuration of the domain volume fractions in the saturated (a) and in the remanent (b) state.

a) "least angle" model

$\langle P_z/P^{sp}\rangle = 0.8$

b) the Huber-Fleck model

$\langle P_z/P^{sp}\rangle = 0.5$

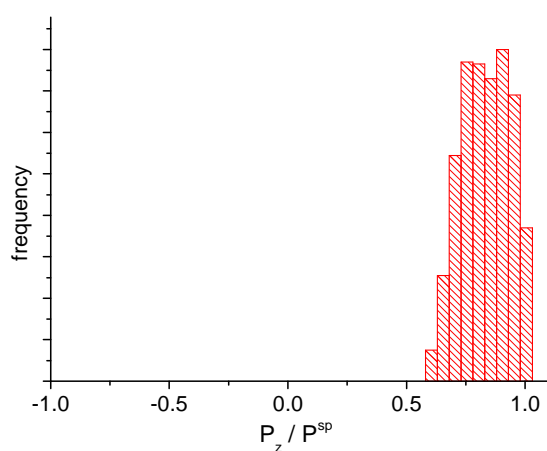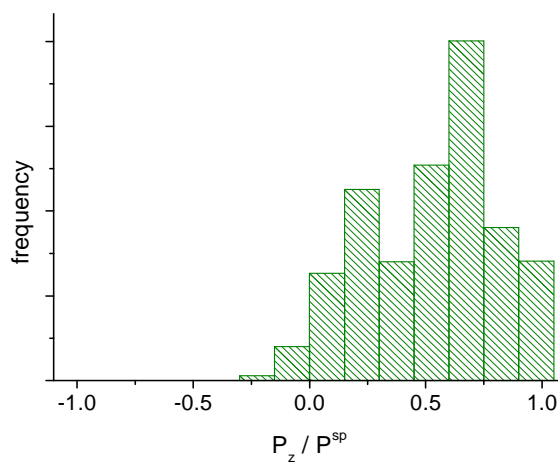**Figure 5.20: Distribution of z-components of the polarizations obtained at remanence within two different numerical models.**

The dependence of the effective material constants on the remanent polarization has been studied theoretically in [Pertsev 1998], [Jayachandran 2009], [Rödel 2003] and [Nan 1996]. The direct comparison of their data with experimental values, however, seems to be barely possible because theoretical data on the polarization or texture angle at the remanent state are not available. Hence, the averaged remanent polarizations determined within the linear "least angle" model and non-linear Huber-Fleck model (see Figure 5.20) were used to obtain the effective ε_{33}^* and d_{33}^* constants of a poled BTO bulk ceramic from the curves of alternative theoretical method [Pertsev 1998]. These values are compared with theoretical results obtained in the present work as well as with experimental data in Table 5.5. The values of effective d_{33}^* coefficients obtained from different theoretical procedures are similar. The corresponding experimental values found in the literature vary considerably. The range of variation includes theoretical predictions. The effective dielectric constant for $<P^{rem}/P^{sp}>$=0.5 determined from the method of effective piezoelectric medium [Pertsev 1998] is of order of 1300 and is very close to the experimentally derived value of 1400. In contrast, the ε_{33}^* constant calculated on the basis of $<P^{rem}/P^{sp}>$=0.8 is much smaller (800) and therewith incomparable with the experimental data. The results discussed above demonstrate that the Huber-Fleck procedure provides realistic values of total remanent polarization, which can be used to obtain effective material coefficients from various theoretical models.

5.2.2 Thin film

The Huber-Fleck simulations for BTO thin films have been performed by means of clamped models with different in-plane tensile stresses (see section 5.1.1). The hysteretic properties of thin films as a function of the tensile stress caused by the substrate are given in Figure 5.21, Figure 5.22 and Table 5.6. The effective dielectric constant ε_{33}^* is almost independent on the in-plane stress. The remanent polarization as well as the piezoelectric parameter d_{33}^*, in contrast, are very sensitive to the tensile stress: the larger the tension, the lower the remanent polarization and the piezoelectric response. Unfortunately, the direct comparison of our results with experimental data is impossible as in the measurements of piezoelectric constants the in-plane stress is usually not published and the variation of experimental results is very large (see Table 5.6).
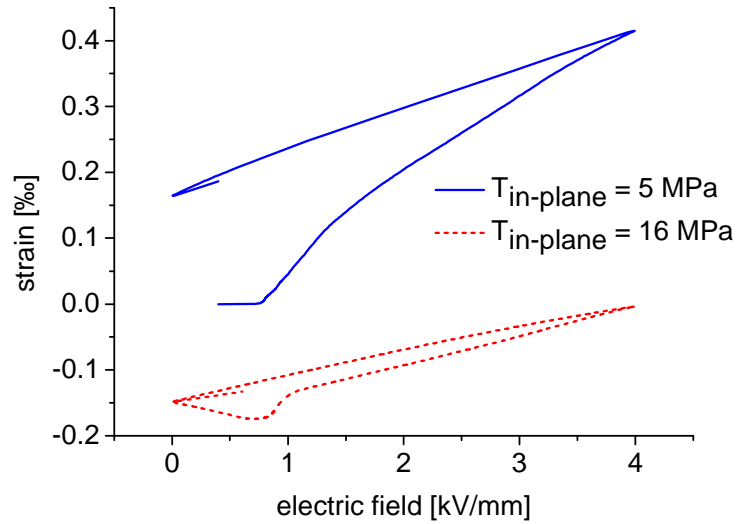
Figure 5.21: Strain hysteresis of a BTO thin film as a function of the tensile stress acting in the film plane.
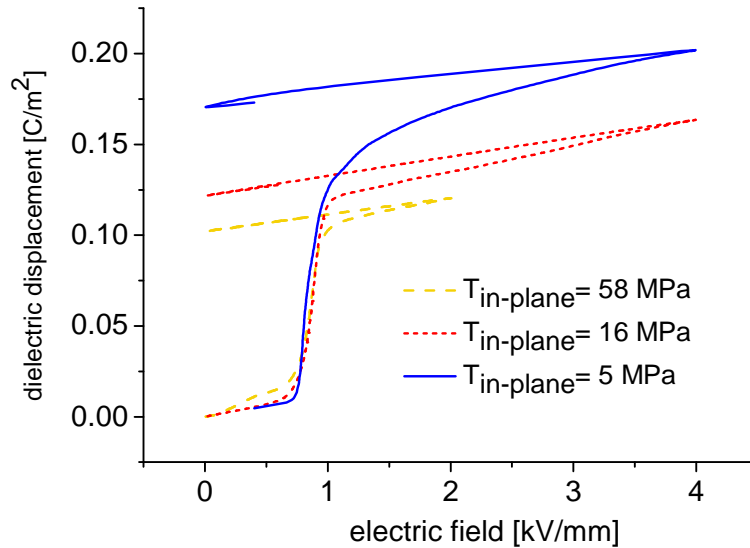
Figure 5.22: Polarization hysteresis of a BTO thin film as a function of the tensile stress acting in the film plane.

BaTiO$_3$ thin film	Present work			Method of eff. piezoel. medium [Pertsev 1998] $<P^{rem}/P^{sp}>=0.27$	Experimental results
	"Least angle"	Huber-Fleck			
		$T_{in-plane}$=5 MPa	$T_{in-plane}$=35 MPa		
ε_{33}^{*} (-)	560±20	1150	1120	1400	1500 [Desu 1993] 700 [Kamlasanan 1993] 385 [Tanaka 2004]
d_{33}^{*} (pC/N)	54±1	44 ±1	26±1	15 ±5	15 [Tanaka 2004]

Table 5.6: Effective material constants of a BTO thin film derived from different theoretical models and from experiments.

The derived effective piezoelectric constants of thin films are considerably smaller than those of the bulk samples (compare with data of Table 5.5). The main reason for such a behavior is the polarization configuration of the thin film sample at remanence (see Figure 5.23 and Figure 5.24). Due to the tensile in-plane stress it exhibits much more domains with negative and nearly zero z-components of polarization than that of a bulk samples. Consequently, the normalized remanent polarization of a BTO film staying under the tensile stress of 35 MPa is of order 0.3, what is 40% lower than the same parameter of a bulk ceramic (0.5, see section 5.1.1). According to [Pertsev 1998], the normalized polarization of $<P^{rem}/P^{sp}>=0.3$ results in the effective piezo-electric constant $d_{33}^{*}=\left(15\pm5\right)pC/N$. This value is in agreement with the experimental data of Ref. [Tanaka 2004]. The excellent agreement between the experiment and our simulations confirms the Huber-Fleck model to be very reliable not only for calculations of the hysteresis curves and material parameters but also for the indirect determination of material properties via the normalized remanent polarization.
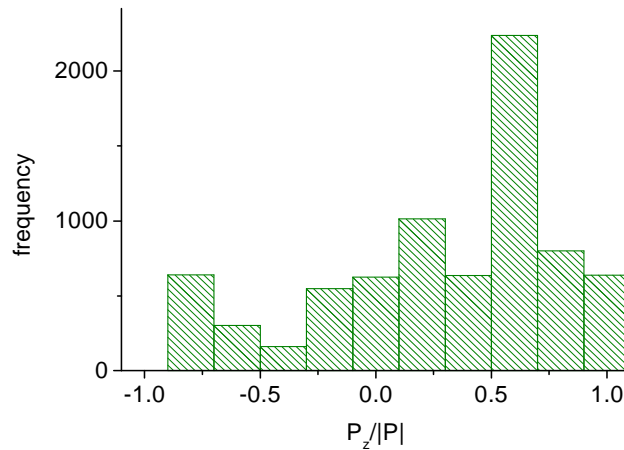

$z, \boldsymbol{E}$
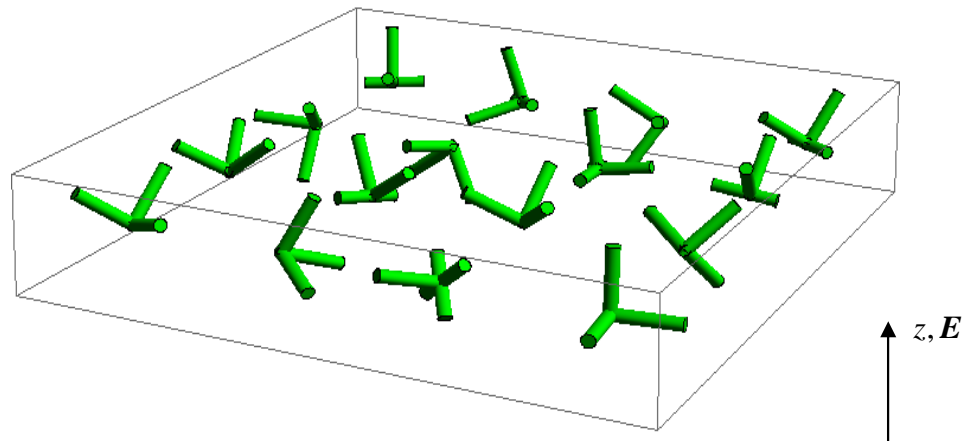
a) clamped BTO thin film with the in-plane stress of 35 MPa
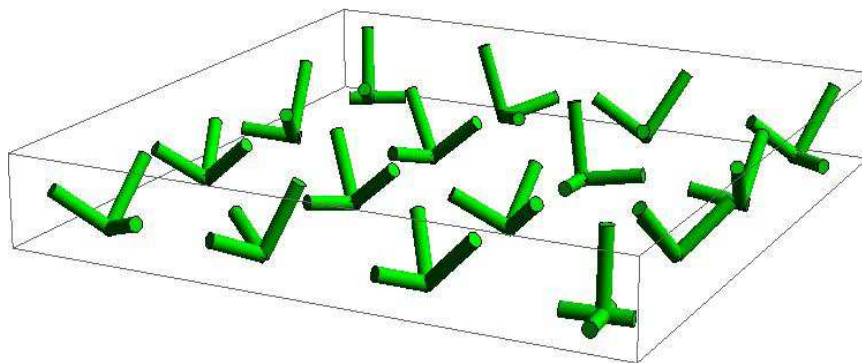
b) BTO bulk sample without stress (see Section 5.2.1)

Figure 5.23: Configuration of the domain volume fractions for a thin film (a) and a bulk BTO samples (b) at remanence.

Figure 5.24: Distribution of z-Components of domain polarization in a clamped BTO thin film staying under in-plane tensile stress of 35 MPa.

Comparing the polarization configurations of the thin film and bulk ceramics at remanence (see Figure 5.23) one notices immediately that the fraction of domains polarized in the surface plane is larger for the thin film than for the bulk sample. With this knowledge it seems to be plausible to expect that the effective dielectric constant ε_{33}^{*} for the thin film is larger in comparison to the bulk polycrystal since the high single-crystal coefficient ε_{11} predominates over the small single-crystal coefficient ε_{33}. The expectation is, however, not true. In contrast, the ε_{33}^{*} of the thin film BTO is about 1120-1150 which is at least 10% smaller than ε_{33}^{*} of the bulk BTO (1240). The reason for the non-trivial behavior of the dielectric constants is the significant fraction of polarization domains with negative z-components enhancing the influence of the small single-crystal ε_{33}-constant. The experimental value ε_{33}^{*} = 385 [Tanaka 2004] is lower than both of the calculated constants and, therefore, cannot be explained just on the basis of clamping or strain induced by the substrate. One possible reason for the extremely small value of dielectric constant obtained by Tanaka is the so-called „dead layer" with a very low dielectric susceptibility at the interface to the electrodes (see section 2.4). This effect has not been modeled in the present work. It can be, however, incorporated in the model if required.

According to the reference [Damjanovic 1998] the hysteresis curves of ferroelectric thin films show a very low remanent polarization and significantly larger coercivity than the bulk materials of similar composition. The results of the present section indicate that the decrease of the remanent polarization can be explained by the in-plane strain arising due to the substrate. However, the tensile strain cannot be the only reason for the increase of the coercive field (see

117

Figure 5.22). The huge enhancement of the coercivity might be caused by the „dead layer"- effect or by the pinning of domain walls at the crystal surface or at the grain interfaces [Damjanovic 1998].

Within the Huber-Fleck model the coercivity can be influenced by the strength of the critical switching energy. In order to determine the sensitivity the critical switching energy has been varied between $0.5\dfrac{MJ}{m^3}$ and $2\dfrac{MJ}{m^3}$ for the models with the tensile in-plane stress of 35 MPa (see Table 5.7 and Figure 5.25). Increase of the critical energy density G$^{180°}$ from $0.5\dfrac{MJ}{m^3}$ to $2\dfrac{MJ}{m^3}$ leads to enhancement of coercive field, remanent strain and to decrease of the effective piezoelectric constant d_{33}^{*} (see Table 5.7).

BaTiO$_3$ thin film T$^{in-plane}$=35 MPa	G$^{180°}$=0.5 MJ/m^3	G$^{180°}$=2 MJ/m^3	Experimental results
ε_{33}^{*} (-)	1120	1180	1500 [Desu 1993], 700 [Kamlasanan 1993], 385 [Tanaka 2004]
d_{33}^{*} (pC/N)	26 ±1	21 ±1	15 [Tanaka 2004]

Table 5.7: **Influence of the critical switching energy on the dielectric and the piezoelectric constants on the example of a clamped BTO sample under the in-plane tensile stress of 35MPa.**

The enlargement of the switching energy and the coercive field could be caused by the lower grain and domain sizes, because the propagation of domain walls is then stronger constrained by the grain and domain boundaries. From this argument it is justified to increase the switching energy for modeling fine-grained systems, which yield lower effective piezoelectric coefficients than in the case of coarse-grained structures as confirmed by the calculations within the Huber-Fleck model.
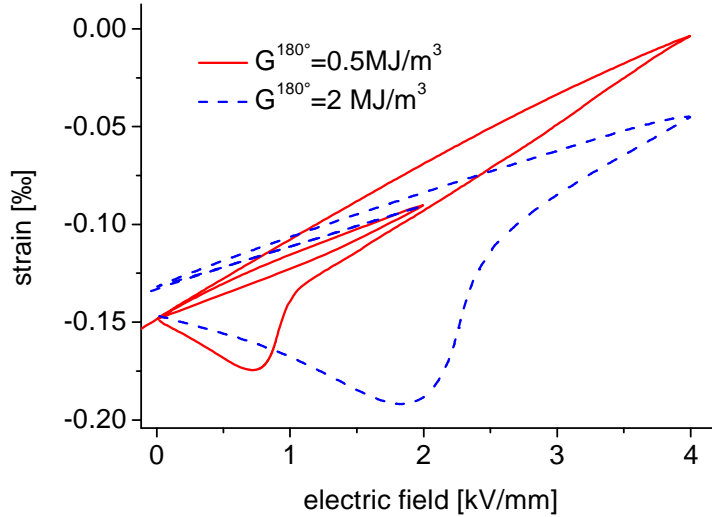
Figure 5.25: Influence of the critical switching energy on the strain hysteresis.

5.3 Simulations of PbTiO$_3$

Similar to the investigations on BTO in section 5.2, theoretical results on linear and non-linear properties of PTO thin films and bulk ceramics are provided in the following. Hereby, several theoretical models are evaluated as to be able to predict properties of the real material.

5.3.1 Bulk

The polarization and strain hysteresis of a non-clamped, stress-free bulk sample have been studied in the framework of the Huber-Fleck procedure using experimental single-crystal constants. The results are shown together with outcomes for PTO thin films in Figure 5.26. The effective dielectric and piezoelectric constants obtained in the Huber-Fleck simulations are collected in Table 5.8 and compared with the corresponding parameters derived from the model of least angle to the applied field as well as from the method of the effective piezoelectric medium. Apart from the last model the calculated constants lie in the range of experimentally determined parameters.

Figure 5.26: Polarization - and strain hysteresis of PTO bulk and thin film models.

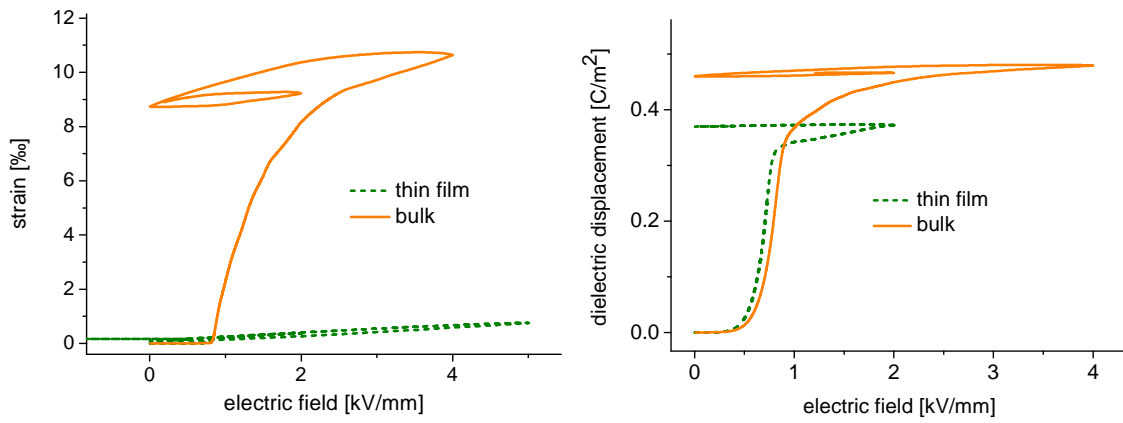| PbTiO$_3$ bulk	COMFEM		Method of eff. piezoel. medium [Pertsev 1998] P^{rem}/P^{sp}=0.53	Experimental results
	Least angle	Huber-Fleck		
ε_{33}^* (-)	54±1	68	100	50 [Shirane 1951]
d_{33}^* (pC/N)	62±2	53	30	51 [Ikegami 1971] 28 [Ueda 1972]

Table 5.8: Effective material constants of a bulk PTO sample, calculated using the experimental constants as input.

The experimental value of effective dielectric constant for PTO (50) is considerably smaller than that of BTO (1400), which significantly affects capacitive properties of PTO. This striking fact can be explained by means of Huber-Fleck calculations. In Figure 5.27 the polarizations configuration of a polarized PTO ceramic is compared with that of an equivalent BTO sample. In the PTO model the orientations near to the applied field are populated stronger than that of the BTO polycrystal, while the directions perpendicular to the field have smaller domain volume fractions compared to the BTO model. So the contribution of the single-crystal dielectric constant ε_{33}=37 to the ε_{33}^* value of bulk PTO is considerably larger than that of single-crystal ε_{11}=110. In contrast, in BTO the contribution of ε_{11}=1910 is stronger than that of ε_{33}=117. The differences in magnitude of domain fractions give a plausible explanation for the very small dielectric constant of a pure PTO. In order to increase the dielectric constant and so the dielectric capacitance of PTO ceramics different kinds of doping are usually used [Ikegami 1971]. A possible reason for the difference between the polarizations configurations of BTO and PTO in remanent state is the larger value of the spontaneous polarization of PTO. It is almost five times larger than that of BTO (see Table 4.3 and Table 4.4:).
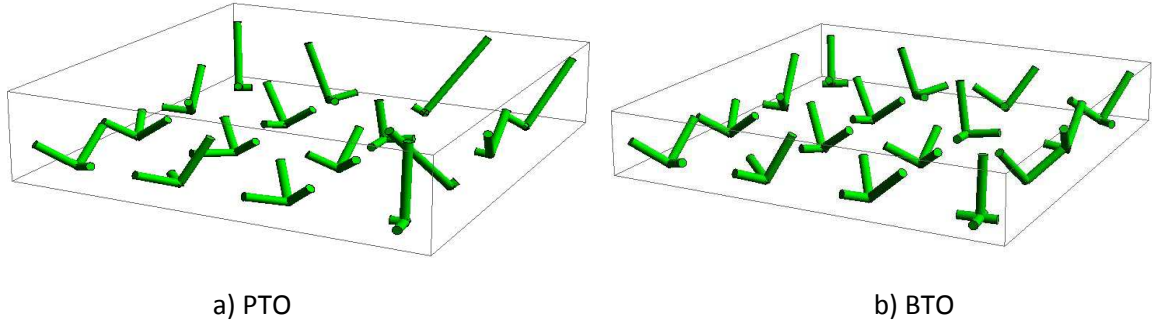
| a) PTO | b) BTO |

Figure 5.27: Comparison of polarization configurations of bulk PTO (a) and BTO (b) polycrystals.

In order to evaluate the multi-scale procedure proposed in section 4.6 the effective dielectric and piezoelectric coefficients of PTO were calculated not only with experimental input data but also using DFT/atomistics as well as DFT/phase-field single-crystal constants. The results of these calculations are summarized in Table 5.9. The computations using the DFT/atomistics data underestimate the experimental dielectric constant ε_{33}^* because of missing contributions from the domain wall motion. The simulations with ε^{PF*}, in contrast, overestimate the experimental value of the effective dielectric constant as the contribution of the domain walls

$$\left(\frac{\partial P_1}{\partial E_1}\right)^{PTO} = \left(\frac{\partial P_3}{\partial E_3}\right)^{PTO} = 73$$ within this approach presumably exceeds its real value as shown

in section 4.6.2.

PbTiO$_3$ bulk	Huber-Fleck Calculations			Experiment
Input data	$c^{Exp}, d^{Exp}, \varepsilon^{Exp}$	$c^{DFT}, d^{DFT}, \varepsilon^{SM}$	$c^{DFT}, d^{DFT}, \varepsilon^{PF*}$	
ε_{33}^* ()	68	22	90	50 [Shirane 1951]
d_{33}^* (pC/N)	53	67	67	51 [Ikegami 1971] 28 [Ueda 1972]

Table 5.9: Effective material constants of bulk PTO ceramics calculated with different input parameters.

5.3.2 Thin film

The material constants derived in the framework of different models with experimental input data are summarized and compared with experimental values in Table 5.10. The dielectric constants obtained within the Huber-Fleck-model lie much closer to the experimentally determined values than those calculated within the least angle model.

PbTiO$_3$ thin film	Present work		Method of eff. piezoel. medium	Experimental results
	Least angle	Huber-Fleck		

		clamped	clamped $T^{\text{in-plane}}$	[Pertsev 1998] $P^{\text{rem}}/P^{\text{sp}}=0.5$	
ε_{33}^{*} ()	54	77	80	100	90-200 [Matsui 1981] 110-120 [Bao 2002]
d_{33}^{*} (pC/N)	52	49	40	20	-
P^{rem} (C/m²)	-	37	34	-	27 [Bao 2002]

Table 5.10: Effective material constants of a clamped 16-grain PTO probe, calculated with experimental input constants.

Figure 5.28 shows the polarization hysteresis curves for different values of the in-plane stress induced by the substrate. As expected the remanent polarization decreases with increasing tension loading. The direct comparison with experimental data seems to be difficult because of the lack of the data on stress magnitudes [Bao 2002].
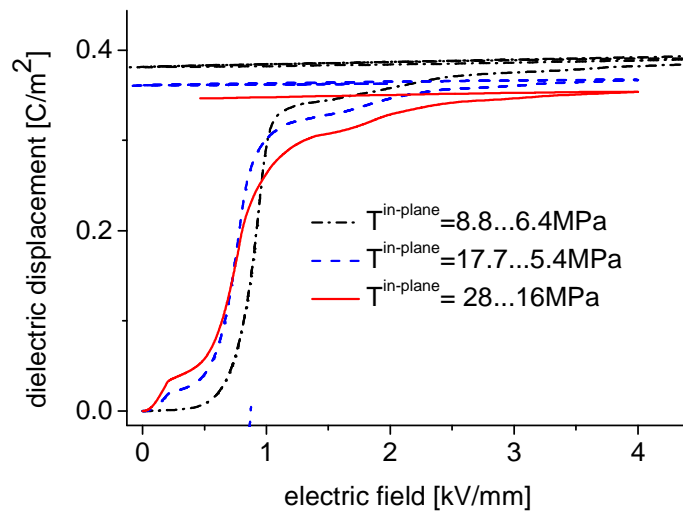
**Figure 5.28: Polarization hysteresis of a PTO thin film for different stress magnitudes.**

The experimentally measured dielectric constant of the PTO thin film as well as that calculated in the framework of the Huber-Fleck model is larger than that of the corresponding bulk polycrystal while for BTO the corresponding relationship between thin film and bulk material is opposite (see section 5.2.2). This surprising effect can be attributed to the domain configurations formed at remanence. The typical polarization configurations of a free, clamped without and with tensile stress PTO polycrystals are compared in Figure 5.29. In the last case the fewest domains are oriented in the direction of the applied field: a large number of polarizations is in-plane oriented. Accordingly, the contribution of $\varepsilon_{11}=110$ is also larger than that of $\varepsilon_{33}=37$ for the PTO thin film, while for the bulk PTO ceramic $\varepsilon_{33}=37$ delivers the dominant contribution.

Effective material constants, derived using the least angle model, do not change for varying magnitude of the in-plane stress because the polarization configuration remains unaffected.

a) unclamped

b) clamped

c) clamped, in-plane tensile stress
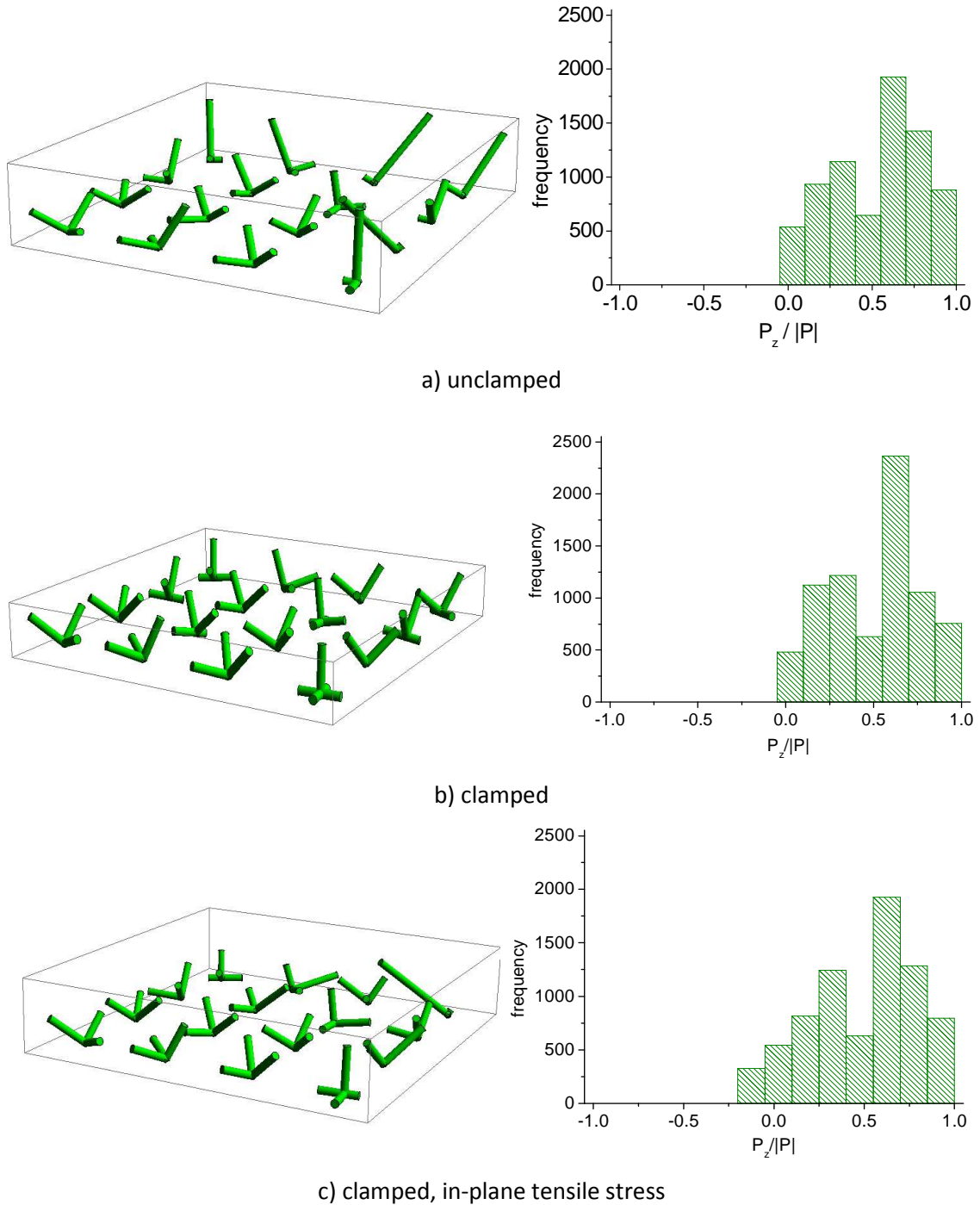
Figure 5.29: Comparison of typical polarization configurations for different PTO models.

Additionally to the calculations using experimental material constants, modeling with input parameters obtained theoretically within DFT, shell-model as well as phase-field method (see section 4.6.2) has been performed. Results for the effective dielectric constant are summarized in

Table 5.11. The effective piezoelectric constants are not included into the table since no experimental values could be found in the literature.

PTO clamped $T^{in\text{-}plane}$	Huber-Fleck Calculations			Experiment
Input data	$c^{Exp}, d^{Exp}, \varepsilon^{Exp}$	$c^{DFT}, d^{DFT}, \varepsilon^{SM}$	$c^{DFT}, d^{DFT}, \varepsilon^{PF*}$	
ε_{33}^{*} ()	80	34	113	90-200 [Matsui 1981] 110-120 [Bao 2002]

Table 5.11: Effective dielectric material constants of a polycrystalline PTO thin film calculated using input parameters obtained within different procedures.

The most convincing results on ε_{33}^{*} showing good agreement with experimental data have been obtained in simulations where the contributions of the domain wall motion were included via the input parameters ε^{PF*}. The computations performed with the dielectric constants ε^{SM} from the shell-model neglecting the domain wall contribution show large deviations from the experimental results.

5.3.3 (111)-textured thin film

In a similar manner to the previous calculations the effective dielectric and piezoelectric properties of a PTO (111) thin film have been calculated using different input data. The results are collected in Table 5.12.

PTO (111) thin film	Least angle			Huber-Fleck			Experiment
Input data	$c^{Exp}, d^{Exp}, \varepsilon^{Exp}$	$c^{DFT}, d^{DFT}, \varepsilon^{SM}$	$c^{DFT}, d^{DFT}, \varepsilon^{PF}$	$c^{Exp}, d^{Exp}, \varepsilon^{Exp}$	$c^{DFT}, d^{DFT}, \varepsilon^{SM}$	$c^{DFT}, d^{DFT}, \varepsilon^{PF*}$	-
ε_{33}^{*} ()	100	77	66	80	34 - 50	150	150 [Bruchhaus 1998]
d_{33}^{*} (pC/N)	29	31	32	48	44	32	20 [Bruchhaus 1998]

Table 5.12: Effective dielectric and piezoelectric constants for a PTO (111)-textured thin film.

In contrast to the texture-free polycrystalline materials the calculations for (111)-textured films performed with the least angle model and the Huber-Fleck procedure using equivalent single-crystal constants do not show any significant differences. The reason for this effect lies in the

very similar polarization configurations of both models, which arises from the symmetry constriction induced by the texture. In Figure 5.30 configuration of polarizations obtained from the Huber-Fleck model is depicted. All electric dipoles lie close to the possible least angle orientation. Calculations with c^{DFT}, d^{DFT} and ε^{PF*} as input parameters provided the best agreement with experimental data similar to the untextured PTO thin films.
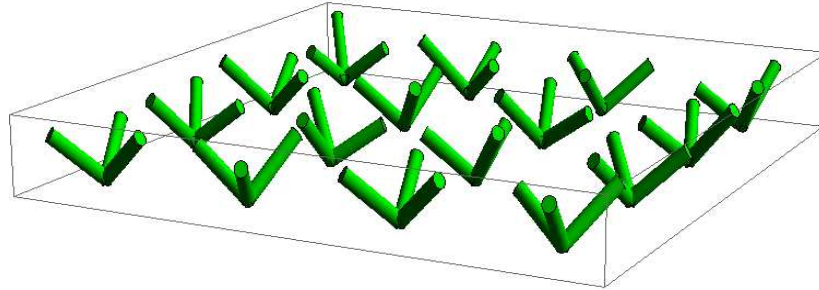

Figure 5.30: Polarization configuration of a (111) thin film at remanence calculated from the Huber-Fleck model. The deviation of [111] axis from its ideal orientation equals 10°.

5.4 Investigations of PbZr$_{0.5}$Ti$_{0.5}$O$_3$

5.4.1 Bulk

Typical polarization and strain hysteresis curves of a polycrystalline PZT bulk sample obtained in Huber-Fleck simulations are given in Figure 5.31, while the corresponding effective material characteristics are summarized in Table 5.13. The calculated piezoelectric constant is considerably smaller than the corresponding experimental value. Similar to other investigated materials the reason for the deviation lies in the missing contributions of the domain wall motion in the model parameter d^{DFT}. However, the contribution of the domain wall motion cannot be quantified because of some artifacts of the phase-field model (see section 4.6.2). The effective dielectric constants ε_{33}^* obtained in the calculations using ε^{PF*} as input parameter is considerably lower than the corresponding experimental value. The domain wall contribution to the effective dielectric constant estimated within the phase-field theory probably underestimates the realistic value (see section 4.6.2).

125
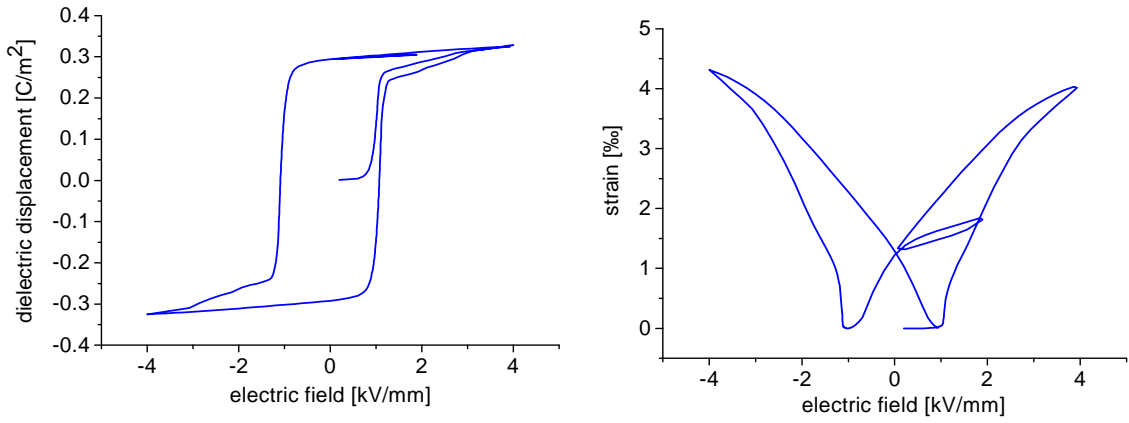
Figure 5.31: Polarization and strain hysteresis for an unclamped sample with input parameters ε^{PF*}, d^{DFT}, and c^{DFT}.

PZT bulk	Huber-Fleck calculations		Experimental results
	ε^{PF*}, d^{DFT}, c^{DFT}	ε^{exp*}, d^{DFT}, c^{DFT}	
ε_{33}^{*} ()	410	650	585 [Landolt 2001]
d_{33}^{*} (pC/N)	23	23	173 [Landolt 2001]
P^{rem} (C/m2)	29	29	-

Table 5.13: Comparison of the effective material constants calculated using different input parameters and corresponding experimental results.

5.4.2 (111)-textured thin film

5.4.2.1 Small- and large-signal properties

The polarization hysteresis curves of ceramic thin films are softer than those of corresponding bulk materials: a typical hysteresis loop is tilted to the right, shows a smaller remanent polarization than that of a bulk sample but partially a larger (up to 1000%) coercivity [Damjanovic 1998]. Experimental investigations show that the lower the film thickness the higher the tilting as well as reduction of remanent polarization (see Figure 5.32). In thinner films the in-plane stress due to the substrate is higher than in thicker films. In order to model different film thicknesses various in-plain tensile stress values have been applied. Our calculations for (111)-textured PZT thin film with Huber-Fleck model show similar behavior to Figure 5.32 (see Figure 5.33). The simulations of Figure 5.33 were based on the dielectric constant ε_{ij}^{exp*} (see section 4.6.1).
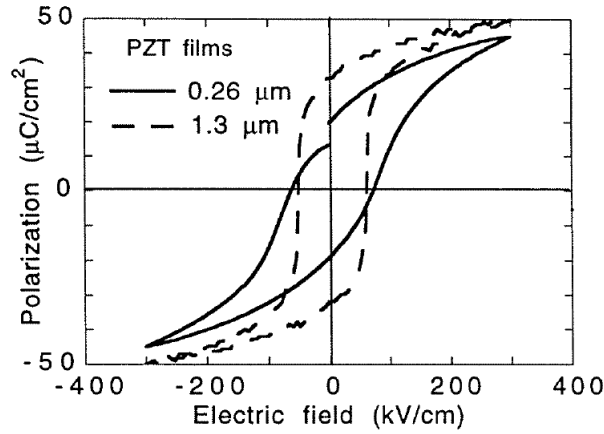
Figure 5.32: Thickness dependence of the hysteretic properties of a (111) PZT thin film: experimental data [Damjanovic 1998].
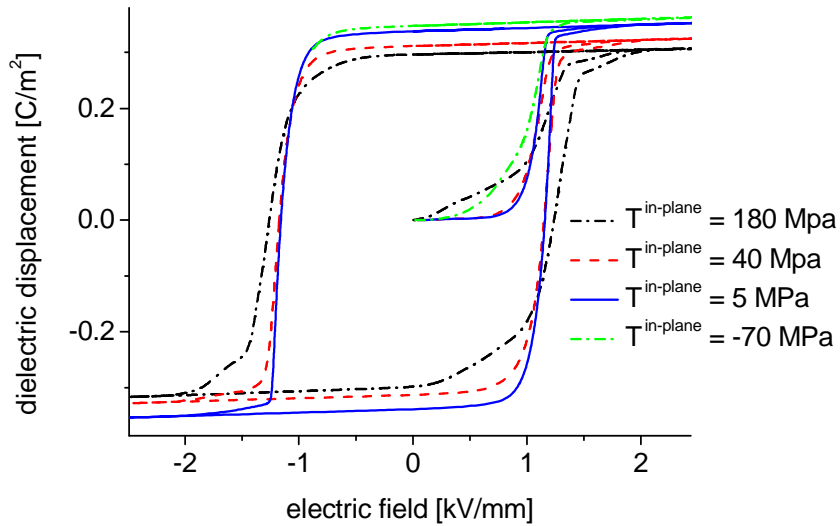
Figure 5.33: Tensile stress dependence of the polarization hysteresis for a (111)-textured PZT film.

It has been found that the strength of the coercive field of a sample under the tensile stress of 180 MPa is only 10% larger than that of the bulk polycrystal investigated in the last section. It means that the huge increase of the coercivity in thin films cannot be explained by the elastic effects induced by the substrate only. Two reasons for the enhanced coercivity should be taken into account: i) the so-called dead-layer effect, appearing at the interface between the sample and the electrodes, and ii) the reduced domain wall mobility due to the decrease of grain and domain size [Damjanovic 1998].

In order to evaluate different procedures of multi-scale modeling for (111)-textured PZT films the effective ε_{33}^*- and d_{33}^*-constants have been calculated for clamped but not additionally strained samples using different input data. The results are presented in Table 5.14. Similar to

the PTO (111)-textured film the piezoelectric constants show negligible variations between results of least angle and Huber-Fleck models for identical input parameters. The dielectric constants gained with ε^{Exp*} are, in contrast, considerably higher and closer to the experimental findings than those based on ε^{SM} single-crystal values from the atomistic shell model. An evident reason for the above described results is the large difference between ε^{SM} (18 and 77, see Table Table 4.5) and ε^{Exp*} having elements round 600. Effective dielectric constants obtained with ε^{PF*} are considerably smaller. The reasons are probably too small domain wall contributions

$$\left(\frac{\partial P_1}{\partial E_1}\right)^{PZT} = \left(\frac{\partial P_3}{\partial E_3}\right)^{PZT} = 372$$ obtained from the phase-field model. Comparing theoretical and

experimental results one has to keep in mind that not all experimental conditions like stress due to mismatch between the substrate and the thin film are known. Therefore, a certain deviation between theoretically and experimentally determined properties is unavoidable.

PZT (111) thin film	Least angle				Huber-Fleck		Experiment
Input single-crystal data	c^{DFT}, d^{DFT}, ε^{Exp*}	c^{DFT}, d^{DFT}, ε^{SM}	c^{DFT}, d^{DFT}, ε^{PF}	c^{DFT}, d^{DFT}, ε^{PF*}	c^{DFT}, d^{DFT}, ε^{Exp*}	c^{DFT}, d^{DFT}, ε^{SM}	-
ε_{33}^* ()	690	94	84	470	630	0	800 [Bruchhaus 1998]
d_{33}^* (pC/N)	36	33	35	35	29	32	60 [Bruchhaus 1998]

Table 5.14: Effective ε_{33}^*- and d_{33}^*-constants of a (111) PZT thin film gained via different calculation methods.

In addition to the already discussed peculiarities of the dielectric constants the analysis of the results given in Table 5.14 reveals another noticeable feature: the effective ε_{33}^*-constant calculated on the basis of ε^{PF} is small, similarly to that calculated with ε^{SM}, although the ε^{PF}-tensor has rather large elements (e. g. 407, see equation (4.77)). In the following we provide an explanation for this effect.

As shown in section 4.6.2 the dielectric tensor of a film consisting of two domains only may be represented in the following form (see equation (4.71)):

$$\varepsilon^{PF} = \begin{pmatrix} \frac{1}{2}\left(\varepsilon_{11}^{SM} + \varepsilon_{33}^{SM}\right) + \frac{\partial P}{\partial E} & 0 & -\frac{\partial P}{\partial E} \\ 0 & \varepsilon_{11}^{SM} & 0 \\ -\frac{\partial P}{\partial E} & 0 & \frac{1}{2}\left(\varepsilon_{11}^{SM} + \varepsilon_{33}^{SM}\right) + \frac{\partial P}{\partial E} \end{pmatrix} \tag{5.2}$$

Arising from phase-field calculations for PZT $\frac{\partial P}{\partial E} = 372$ is the domain wall contribution entering in several tensor elements. The transformation of the tensor (5.2) from the crystal coordinate system of the crystal to that of the substrate (for which the [111]-direction is oriented perpendicularly to the film surface) with the help of the transformation tensor

$$a^{CS \to SS} = \begin{pmatrix} -\frac{1}{\sqrt{2}} & \frac{1}{\sqrt{2}} & 0 \\ -\frac{1}{\sqrt{6}} & -\frac{1}{\sqrt{6}} & \frac{2}{\sqrt{6}} \\ \frac{1}{\sqrt{3}} & \frac{1}{\sqrt{3}} & \frac{1}{\sqrt{3}} \end{pmatrix}, \tag{5.3}$$

leads to

$$\varepsilon^{PF,SS} = a^{CS \to SS} \varepsilon^{PF,CS} \left(a^{CS \to SS}\right)^T =$$

$$= \begin{pmatrix} \frac{1}{4}\left(2\frac{\partial P}{\partial E} + 3\varepsilon_{11}^{SM} + \varepsilon_{33}^{SM}\right) & \frac{1}{4\sqrt{3}}\left(6\frac{\partial P}{\partial E} - \varepsilon_{11}^{SM} + \varepsilon_{33}^{SM}\right) & \frac{1}{2\sqrt{6}}\left(\varepsilon_{11}^{SM} - \varepsilon_{33}^{SM}\right) \\ \frac{1}{4\sqrt{3}}\left(6\frac{\partial P}{\partial E} - \varepsilon_{11}^{SM} + \varepsilon_{33}^{SM}\right) & \frac{1}{12}\left(18\frac{\partial P}{\partial E} + 7\varepsilon_{11}^{SM} + 5\varepsilon_{33}^{SM}\right) & \frac{1}{6\sqrt{2}}\left(-\varepsilon_{11}^{SM} + \varepsilon_{33}^{SM}\right) \\ \frac{1}{2\sqrt{6}}\left(\varepsilon_{11}^{SM} - \varepsilon_{33}^{SM}\right) & \frac{1}{6\sqrt{2}}\left(-\varepsilon_{11}^{SM} + \varepsilon_{33}^{SM}\right) & \frac{1}{3}\left(2\varepsilon_{11}^{SM} + \varepsilon_{33}^{SM}\right) \end{pmatrix}. \tag{5.4}$$

For a (111) texture there is only one degree of freedom – the rotation about the [001] direction of the substrate coordinate system, which corresponds to the [111] direction of the crystal coordinate system. This rotation, however, does not change the elements $\varepsilon_{33}^{PF,SS}$. This demonstrates that the effective coefficients ε_{33}^{*} do not depend on the domain wall contribution $\frac{\partial P}{\partial E}$, but rather are determined by contributions ε_{11}^{SM} and ε_{33}^{SM} derived from the atomistic simulations. That is why the effective ε_{33}^{*} constant, which has been obtained using ε^{PF}, is quite small, similar to that determined utilizing ε^{SM}.

Recent experiments show that the piezoelectric and dielectric constants of (111)-textured thin films with significant Zr fraction (PbZr$_x$Ti$_{1-x}$O$_3$ with $x \approx 0.5$) exceed the corresponding material parameters of Zr – poor samples ($x \leq 0.2$, e.g. PbTiO$_3$) by the factor of two (see Figure 5.34). Effective ε_{33}^{*}- und d_{33}^{*}-coefficients of PTO and PZT thin films calculated in this work are compared in Table 5.15. Analogous to the described trend of Figure 5.34 the PZT parameters are

larger than corresponding values of PTO-films. The difference is, however, less pronounced. The latter observation seems to have three reasons: (i) the single-crystal constants obtained within the atomistic simulations for PZT polycrystals only slightly exceed the corresponding coefficients of PTO; (ii) the piezoelectric input data do not possess any domain wall contributions; and (iii) the contributions due to domain wall motion in $\varepsilon^{PF*,PZT}$ are too small.
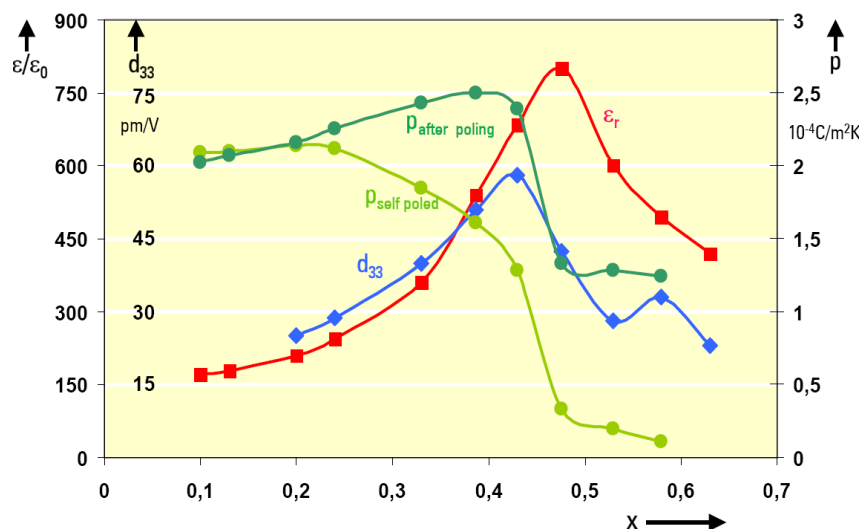

Figure 5.34: **Dielectric, piezoelectric, and pyroelectric constants of a (111)-textured PbZr$_x$Ti$_{1-x}$O$_3$ thin film [Bruchhaus 1998].**

	PTO			PZT		
Input data	$c^{DFT}, d^{DFT}, \varepsilon^{SM}$	$c^{DFT}, d^{DFT}, \varepsilon^{PF}$	$c^{DFT}, d^{DFT}, \varepsilon^{PF*}$	$c^{DFT}, d^{DFT}, \varepsilon^{SM}$	$c^{DFT}, d^{DFT}, \varepsilon^{PF}$	$c^{DFT}, d^{DFT}, \varepsilon^{PF*}$
ε_{33}^{*} ()	77	66	150	94	84	470
d_{33}^{*} (pC/N)	31	32	32	33	35	35

Table 5.15: **Comparison of the simulated effective material constants for (111)-textured PTO and PZT thin films.**

5.4.2.2 Self-polarization

The (111)-textured films manufactured by sputtering usually possess a finite effective polarization even without applying any electric field. This phenomenon is called self-polarization. Recent studies [PYROHL 2000] have demonstrated that even very thin dipolar film arising at the interface between the ceramics and the substrate might promote the spontaneous polarization of the ceramic layer. The spontaneous polarization of thin ceramic films, however, shows very puzzling properties. For example, until now it is not clear why the self-polarization of tetragonal thin films is very robust and remains stable in a very broad range of temperatures despite of the large stress coming from the substrate, while the spontaneous polarization of rhomboedric films

vanishes already at room temperatures. The present section is devoted to the clarification of this exiting question.

Because of the difference in coefficients of thermal expansion of Si substrate ($\alpha^{Si} = 2.8 \cdot 10^{-6} \frac{1}{K}$) and PZT ($\alpha^{PZT} = 7.5 \cdot 10^{-6} \frac{1}{K}$), the thin PZT film shrinks considerably stronger than the substrate during the cooling process after sputtering. Typical temperature changes amount to $\Delta T = -600K$. The magnitude of the in-plane tensile stress $T^{in-plane}$ arising from cooling in a PZT thin film can be estimated using the Young - modulus $Y^{PZT} = 80GPa$ as

$$T^{in-plane} = Y^{PZT}(\varepsilon^{Si} - \varepsilon^{PZT}) = Y^{PZT}\Delta T(\alpha^{Si} - \alpha^{PZT}) = 230MPa. \tag{5.5}$$

The critical stress T^{crit} leading to complete depolarization of the sample can be estimated on example of the 90° polarization switching from the [001] to the [100] direction as this process requires the lowest energy. The corresponding change of strain ΔS reads

$$\Delta S = S^{sp}\begin{pmatrix} 1 & 0 & 0 \\ 0 & -0.5 & 0 \\ 0 & 0 & -0.5 \end{pmatrix} - S^{sp}\begin{pmatrix} -0.5 & 0 & 0 \\ 0 & -0.5 & 0 \\ 0 & 0 & 1 \end{pmatrix} = S^{sp}\begin{pmatrix} 1.5 & 0 & 0 \\ 0 & 0 & 0 \\ 0 & 0 & -1.5 \end{pmatrix}. \tag{5.6}$$

Here, S^{sp} is spontaneous strain of PZT. The critical tensile stress coming from the substrate and leading to the depolarization of the sample can be described as

$$T = T^{crit}\begin{pmatrix} 1 & 0 & 0 \\ 0 & 1 & 0 \\ 0 & 0 & 0 \end{pmatrix}. \tag{5.7}$$

In absence of an electric field the energy of the 90°-switching equals

$$G^{90°} = T \cdot \Delta s = s^{sp} \cdot T^{crit} \cdot 1.5. \tag{5.8}$$

Using $G^{90°}$ and s^{sp} from Table 4.5 the critical stress can be estimated to

$$T^{crit} = \frac{G^{90°}}{1.5 s^{sp}} \approx 30MPa. \tag{5.9}$$

The depolarization of the texture-free poled polycrystalline structure due to the biaxial tensile stress has been simulated in the framework of the Huber-Fleck model. The results are shown in Figure 5.35 a. The first switching events appear at stress strengths of approximately 30-50 MPa. At the stresses about 240 MPa, a typical strain induced by substrate in a thin ceramic film (see equation (5.5), only few domains are oriented along the initial polarization direction. In the case of (111)-textured thin PZT films (see Figure 5.35 b), in contrast, the polarization remains even at high stresses about 240 MPa, which is consistent with experimental findings. The reasons for such a behavior of (111) films are discussed in the following.

T$_x$=0 MPa

T$_x$=80 MPa

T$_x$=240 MPa

a) polycrystalline bulk ceramics   b) (111)-textured thin film
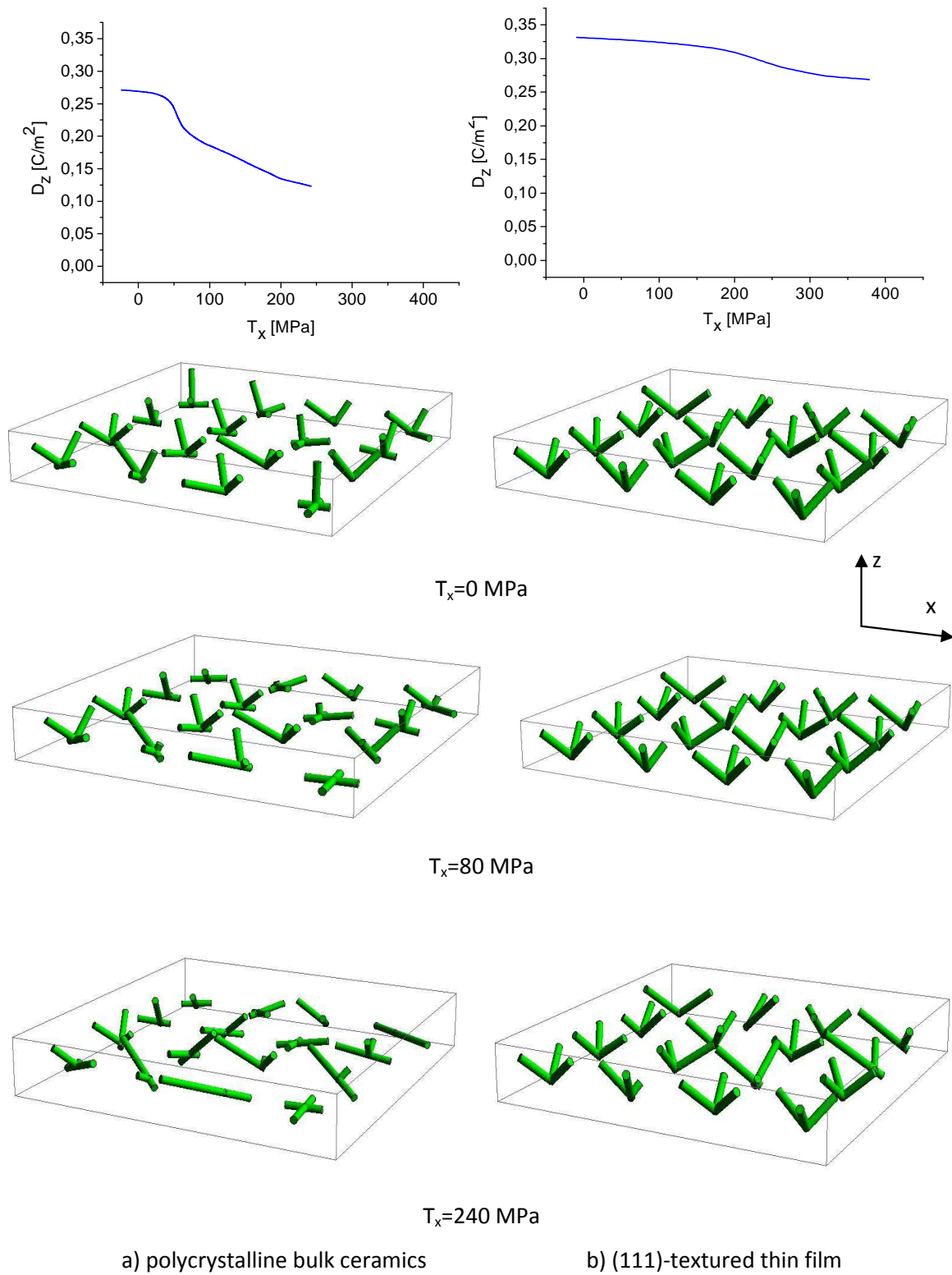
Figure 5.35: Depolarization of a bulk ceramic polycrystalline PZT sample as well as (111)-textured PZT thin film via biaxial tension stress induced by the substrate.

The strain change due to a 90° polarization switch for a (111)-textured sample (5.6) in the substrate coordinate system can be estimated using the transformation tensor (5.3) as

$$\Delta S^{SS} = a^{CS \rightarrow SS} \Delta S^{CS} \left(a^{CS \rightarrow SS} \right)^{T} = s^{sp} \begin{pmatrix} -0.75 & -0.433 & 0.612 \\ -0.433 & 0.75 & 1.06 \\ 0.612 & 1.06 & 0 \end{pmatrix}. \qquad (5.10)$$

The scalar product with an arbitrarily large tensile strain; i.e., the projection of ΔS^{SS} on the direction of loading (5.7)

$$G = T \cdot \Delta S^{SS} = 0. \qquad (5.11)$$

This means that the energy G involved into each 90° switching event equals zero for any (111) oriented grain. Analogously, it can be shown that the energy vanishes for every 180° switching event as well. Consequently, the rate of operation (see section 4.5)

$$\dot{f}^{\alpha} = B^{\alpha} \left| \frac{G^{\alpha}}{G_c^{\alpha}} \right|^{n-1} \left(\frac{G^{\alpha}}{G_c^{\alpha}} \right) = 0 \text{ and, therefore, the polarization remains unchanged.}$$

The (111)-texture of a realistic sample is not perfect. Typical deviations of the crystalline structure from an ideal orientation are of order of 5°-10°, which has been incorporated into simulation model. Therefore, small rates of operations $\dot{f}^{\alpha}$ can arise and lead to minimal changes in the polarization configuration as it can be seen in Figure 5.35 b.

The two above discussed examples underline the importance of the crystal symmetry and crystallographic orientation with respect to the loading direction. Crucial is thereby the projection of the strain change due to the switching process on the direction of loading rather than the magnitude of the strain change. In contrast to the tetragonal symmetry discussed above, for a thin ceramic film with rhombohedral crystal structure the projection of the strain change vector for a 71°-switching process reads (see Figure 5.36):

$$\Delta S \cdot T = S^{sp} \cdot \sin(71°) \cdot T^{crit} \cdot 1.3. \qquad (5.12)$$

The factor 1.3 describes the effect of the transversal contraction.

a)   b)
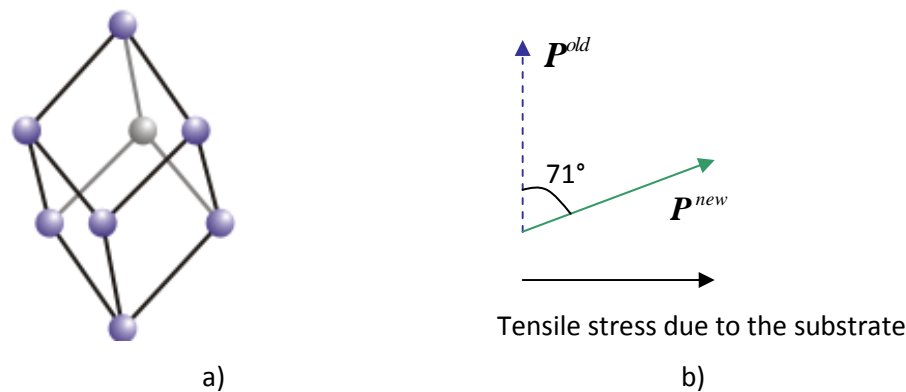
Figure 5.36: a) Rhombohedral cell, violet balls visualize eight possible polarization directions; b) a depolarizing 71°- switching process in a rhombohedral cell polarized perpendicular to the substrate.

The critical depolarizing stress leading to the vanishing of self-polarization in rhombohedral (111) thin films can be calculated using following assumption for the switching energy for the 71°-process $G^{71°} = 1 \dfrac{MJ}{m^3}$:

$$T^{crit} = \frac{G^{71°}}{\Delta s \cdot T} \approx 50 MPa. \tag{5.13}$$

According to (5.5), the thermal coefficient of expansion for the substrate has to be larger than

$$\alpha^{substrate} = \frac{T^{crit}}{Y^{PZT} \Delta T} + \alpha^{PZT} \approx 6.5 \cdot 10^{-6} \frac{1}{K} \tag{5.14}$$

in order to ensure the stability of the spontaneous polarization against the tensile stress. In the calculation the parameters $Y^{PZT} = 80 GPa$, $\Delta T = -600K$ and $\alpha^{PZT} = 7.5 \cdot 10^{-6} \dfrac{1}{K}$ have been utilized. According to this finding, in the project COMFEM rhombohedral PZT (111)-textured thin films were grown on a sapphire wafer as substrate with thermal coefficient of expansion $\alpha^{Sapphire} \approx 16 \cdot 10^{-6} \dfrac{1}{K}$. As predicted in equation (5.14) the self-polarization could be conserved.

6 Summary

In the present thesis, several multi-scale and single-scale approaches are introduced and evaluated for the purpose of accurate prediction of micro- and macroscopic properties of ferroelectric thin films and bulk ceramics. The main focus of the investigation was directed on the formulation of the multi-scale procedure, which is able to reliably describe the properties of novel materials without experimental input data. Another important requirement to the multi-scale chain was a realistic description of the polycrystalline geometry. Our investigations concerned BTO, PTO und PZT ceramics because these materials are widely explored experimentally and theoretically as well as utilized industrially.

For an accurate description of the micro- and macroscopic properties of polycrystalline ceramics single-crystal constants including contributions from the domain wall motion as well as domain structure resulting from polarization switching play the most important roles. In order to take into account the polarization switching the micromechanical Huber-Fleck model has been used. The model was formulated in 2001 [Huber 2001] and utilized for parametric studies with idealistic polycrystalline grains represented by one finite element only [Pathak 2005]. In contrast to previous publications, we studied real materials like BTO, PTO and PZT with non-idealized polycrystalline geometry and adopted the Huber-Fleck procedure for description of thin ceramic films.

In the first step, experimental single-crystal data have been used as input for micromechanical modeling. A good predictability of the Huber-Fleck model has been concluded by means of quantitative comparison with available experimental data. Further, several peculiar experimental findings could be explained on the basis of calculated polarization configurations. In order to exclude the experimental single-crystal constants as input data for the micromechanical model, in the second step single-crystal coefficients obtained from DFT simulations and shell-model have been utilized. In the third step, the contributions coming from the domain wall motion have been evaluated from the phase-field model and incorporated into the Huber-Fleck calculations.

Outcomes of all three steps have been systematically compared with results of analytical calculations using the method of effective piezoelectric medium, simulations within the scheme of

least angle (see section 4.4) and experimental results. We conclude that the Huber-Fleck formulation provided us with the most realistic small-signal constants for bulk as well as for thin film models using the experimental input data or using shell-model parameters combined with domain wall contributions from the phase-field theory. As in contrast to the effective dielectric parameters ε_{33}^* the domain wall contribution to the elastic and piezoelectric material coefficients could not been derived from the phase-filed model, considerable deviations between the theoretical (using DFT data as input parameters) and experimental values of the piezoelectric constant d_{33}^* have been found. An overview of the performed calculations and the degree of agreement with available experimental parameters are given in Table 6.1. Green fields symbolize a small deviation from experimental results (less than 10%), yellow fields – considerable deviation between 10% and 35%, while red fields correspond to rather large deviations (larger then 35%).

Investigated models	Agreement with experimental data		
	ε_{33}^*	d_{33}^*	P^{rem}
BTO bulk	with c^{Exp}, d^{Exp}, ε^{Exp}	With c^{Exp}, d^{Exp}, ε^{Exp}	With c^{Exp}, d^{Exp}, ε^{Exp}
BTO thin film	With c^{Exp}, d^{Exp}, ε^{Exp}	With c^{Exp}, d^{Exp}, ε^{Exp}	-
PTO bulk	With c^{Exp}, d^{Exp}, ε^{Exp}	With c^{Exp}, d^{Exp}, ε^{Exp}	With c^{Exp}, d^{Exp}, ε^{Exp}
PTO thin film	With ε^{PF*}, d^{DFT}, c^{DFT}	With ε^{PF*}, d^{DFT}, c^{DFT}	With c^{Exp}, d^{Exp}, ε^{Exp}
PTO (111) thin film	With ε^{PF*}, d^{DFT}, c^{DFT}	With ε^{PF*}, d^{DFT}, c^{DFT}	-
PZT bulk	With ε^{PF*}, d^{DFT}, c^{DFT}	With ε^{PF*}, d^{DFT}, c^{DFT}	-
PZT (111) thin film	With ε^{PF*}, d^{DFT}, c^{DFT}	With ε^{PF*}, d^{DFT}, c^{DFT}	-

Deviation from exp. results less than 10%	Deviation between 10% and 35%	Deviation from exp. results more than 35%

c^{Exp}, d^{Exp}, ε^{Exp}: *Experimentally determined elastic, piezoelectric, and dielectric single-crystal-tensors*

d^{DFT}, c^{DFT}: *Single crystal tensors of piezoelectric and elastic constants from the ab-initio calculations (Density Functional Theory)*

ε^{PF*}: *dielectric single crystal tensor obtained using results of the ab-initio- and phase-field simulations(see section 4.6.2)*

Table 6.1: Review of the performed calculations and comparison of their results with available experimental data.

There are several reasons for the partially large deviations. The difficulty to derive the domain wall contribution for the piezoelectric constants from the phase-field theory has been already mentioned (see also section 4.6.2). Further, the domain wall contribution, derived within the phase-field procedure for the dielectric single-crystal constants of PZT, with large probability underestimates the realistic value (see section 4.6.2). Because of the impurities, structural defects, resulting pinning of domain walls, small grain sizes and porosity, the constitution of polycrystalline grains does not exactly coincide with that of the model input data. Finally, exact values of mechanical strain induced by the substrate are rarely published in the papers reporting small-signal constants of the thin films.

Despite of the mentioned difficulties, the proposed simulation method allowed us to reproduce numerous experimental findings:

- d_{33}^* of the BTO and PTO thin films are considerably smaller than those of corresponding bulk polycrystals;

- ε_{33}^* of a pure PTO bulk polycrystal is smaller than that of a pure PTO thin film. In the case of BTO ceramics, in contrast, the dielectric constant of bulk material is larger than that of a corresponding thin film.

- ε_{33}^* and d_{33}^* of a PTO (111)-textured thin film are lower than ε_{33}^* and d_{33}^* of a PZT (111)-textured thin film;

- The polarization hysteresis loop of a ceramic thin film is tilted to the right side, possesses a stronger coercive electric field and lower remanent polarization than that of corresponding bulk ceramics.

Furthermore, with help of performed calculations new physical statements could been formulated, e.g. the magnitude of the critical switching energy and so the coercive electric field has only a minor effect on the effective small-signal constants of thin ceramic films. The above described effects as well as results of the Table 6.1 qualify the proposed multi-scale method as a theoretical tool, which can be used for the description and understanding of existing ceramics and for design of new materials.

Additionally to the multi-scale procedure, a new functional approach, which permits to reliably generate realistic structures and finite-element-networks with several thousand grains, has been elaborated in the present work. In order to obtain realistic models of polycrystalline mate-

rials versatile options of this procedure can be applied individually as well in any combinations. They are:

- Voronoi tiling ;
- Hard-core tiling;
- Constrained hard-core-Voronoi tiling;
- agglomerations;
- pores;
- lognormal grain size distribution;
- reliable meshing of grain structures with a small number of finite elements;
- periodic boundary conditions for the grain geometry;
- periodic boundary conditions for the finite-elements network;
- columnar grain structures.

The elaborated constrained hard-core-Voronoi space tiling as well as the developed merging algorithms considerably contribute to the geometric and numerical description of many classes of polycrystalline materials.

References

[Anteboth 2006]   S. Anteboth, „Simulation des elektromechanischen Verhaltens von PZT mit realer Domänenstruktur", Dissertation, University of Kassel, 2006

[Bao 2002]   D. Bao, X. Yao et al., "Structural, dielectric, and ferroelectric properties of $PbTiO_3$ thin films by a simple sol-gel technique", Mat.Science and Eng. **B94**, 269 (2002)

[Böhm 1998]   H. J. Böhm, "A Short Introduction to Basic Aspects of Continuum Micromechanics", Research Report, TU Wien, 1998

[Bruchhaus 1998]   R. Bruchhaus, D. Pitzer, M. Schreiter, W. Wersing, „Optimized PZT Thin Films für Pyroelectric IR Detector Arrays", L. Electroceramics 1998, **3**, 151 (1998)

[Cowan 2007]   R. Cowan, "Some Delaunay circumdisks and related lunes", School of Mathematics and Statistics, University of Sydney, 2007
http://www-personal.usyd.edu.au/~rcowan/professional/circum.pdf

[D'Agostino 1986]   R. B. D'Agostino and M. A. Stephens, "Goodness-of-Fit Techniques", New York: Marcel Dekker, 1986

[Damjanovic 1998]   D. Damjanovic, "Ferroelectric, dielectric and piezoelectric properties of ferroelectric thin films and ceramics, Rep. Prog. Phys. **61**, 1267 (1998)

[Dent 2007]   A. Dent et al., „Effective elastic properties for unpoled barium titanate", J. Europ. Ceram. Soc. **27**, 3739 (2007)

[Desu 1993]   S. B. Desu, "Influence of Stresses on the Properties of Ferroelectric $BaTiO_3$ Thin Films", J. Electrochem. Soc. **140**, 2981 (1993)

[Devonshire 1954]   A. F. Devonshire, "Theory of ferroelectrics", Adv. Phys. **3**(10), 85 (1954)

[Dick 1958]   B. G. Dick, Jr. And A. W. Overhauser, "Theory of the Dielectric Constants of Alkali Halide Crystals", Phys. Rev. **112**, 90 (1958)

[Dunn 1993]   M. L. Dunn and M. Taya, "An Analysis of Piezoelectric Composite Materials Containing Ellipsoidal Inhomogeneties", Proc. R. Society London Ser. A **443**, 265 (1993)

[Dunn 1995]   M. L. Dunn, "Effects of grain shape anisotropy, porosity, and microcracks on the elastic and dielectric constants of polycrystalline piezoelectric ceramics", J. Appl. Phys. **78**, 1533 (1995)

[Elsässer 1990]   C. Elsässer, "Untersuchung der Kohäsions-, Diffusions- und Schwingungseigenschaften von Wasserstoff in Übergangsmetallen mit einer ab-

	initio-Pseudopotentialmethode", Dissertation, University of Stuttgart, 1990
[Ghosez 1999]	P. Ghosez et al., "Lattice dynamics of $BaTiO_3$, $PbTiO_3$, and $PbZrO_3$: A comparative first-principles study", Phys. Rev. B **60**, 836 (1999)
[Ikegami 1971]	S. Ikegami, I. Ueda, T. Nagata, "Electromechanical Properties of $BaTiO_3$ Ceramics Containing La and Mn", J. Acoust. Soc. Am. **50**, 1060 (1971)
[Jaffe 1956]	B. Jaffe, W. R. C. Jr. Jaffe, H. Jaffe, "Piezoelectric Ceramics", London, 1956
[Jayachandran 2009]	K. P. Jayachandran et al., "Homogenization of textured as well as randomly oriented ferroelectric polycrystals", Comp. Mat. Science **45** (816), 2009
[Fan 2004]	Z. Fan et al., "Simulation of polycrystalline structure with Voronoi diagram in Laguerre geometry based on random closed packing of spheres", Comp. Mater. Science **29**, 301 (2004)
[Fröhlich 2001]	A. Fröhlich, „Mikromechanisches Modell zur Ermittlung effektiver Materialeigenschaften von piezoelektrischen Polykristallen", Dissertation, University of Karlsruhe, 2001
[Gavrilyachenko 1971]	V. G. Gavrilyachenko, E. G. Fesenko, Kristallografija **16**, 640 (1971)
[Hohenberg 1964]	P. Hohenberg and W. Kohn, „Inhomogeneous Electron Gas", Phys. Rev. **136(3B),** 864 (1964)
[Hoffmann 2003]	M. Hoffmann et al., IEEE Trans. Ultrason . Ferroel. and Freq. Control **50**, 1240 (2003)
[Huber 1999]	J. E. Huber et al., „A constitutive model for ferroelectric polycrystals", J. Mech. Phys. Sol. **47**, 1663 (1999)
[Huber 2001]	J. E. Huber and N. A. Fleck, "Multi-axial electrical switching of a ferro-electric: theory versus experiment", J. Mech. Phys. Sol. **49**, 785 (2001)
[Kamlah 2005]	M. Kamlah et al., "Finite element simulation of a polycrystalline ferro-electric based on multidomain single crystal switching model", Int. J. Solids Struct. **42**, 2949 (2005)
[Kamalasanan 1993]	M. N. Kamalasanan, N. D. Kumar and S. Chandra, „Dielectric and ferro-electric properties of $BaTiO_3$ thin films grown by the sol-gel process", J. Appl. Phys. **74**, 5679 (1993)
[Kumar 1992]	S. Kumar et al., „Properties of a Three-Dimensional Poisson-Voronoi Tessellation: A Monte Carlo Study", Stat. Phys. **67**, 523 (1992)

[Kunz]	L. Kunz, "Mikromechanische Modellierung von Ferroelektrika im Rahmen einer Multiskalensimulation", Dissertation, to be published at Karlsruhe Institute of Technology
[Landolt 2001]	Landolt-Börnstein, „Ferroelectrics and Related Substances", Volume III/36A1, Springer, 2001
[Lautensack 2007]	C. Lautensack, "Random Laguerre Tesselations", Dissertation, University of Karlsruhe, 2007
[Liu 2002]	D. Liu et al., "Dynamic hysteresis in ferroelectric systems: experiment and Monte Carlo simulation" Mater. Sci. Eng. **326A**, 276 (2002)
[Matsui 1981]	Y. Matsui, M. Okuyama et al., "Laser annealing to produce ferroelectric-phase PbTiO thin films", J. Appl. Phys. **52**, 5107 (1981)
[Miles 1970]	R. E. Miles, "On the Homogeneous Planar Poisson Point Process", Math. Biosciences **6**, 85 (1970)
[Møller 1996]	J. Møller, S. Zuyev, "Ganna-Type Results and Other Related Properties of Poisson Processes", Advances in Appl. Prob. **28**, 662 (1996)
[Muche 1992]	L. Muche, D. Stoyan, "Contact and Chord Length Distributions of the Poisson Voronoi Tesselation", J. Appl. Prob. **29,** 467 (1992)
[Müller 2010]	T. Müller et al., "Modeling of the Microstructure of Sintered Ceramics for Finite Element Simulations Electrical Properties", Fifth International Conference on Multiscale Materials Modeling MMM 2010, Freiburg, Germany
[Nan 1996]	C.-W. Nan, D. R. Clarke, "Piezoelectric Moduli of Piezoelectric Ceramics", J. Am. Ceram. Soc. **79** (10), 1996
[Nettleship 2002]	I. Nettleship et al., "Evolution of the Grain Size Distribution during the Sintering of Alumina at 1350°C", J. Am. Ceram. Soc. **85**, 1954 (2002)
[Ohser 2000]	J. Ohser, F. Mucklich, "Statistical analysis of microstructures in materials science", Wiley, 2000
[Okabe 1992]	A. Okabe et al., "Spatial Tesselations – Concepts and Applications of Voronoi Diagrams", Wiley, 1992
[Okazaki 1972]	K. Okazaki, K. Conrad, "Grain Size Distribution in Recrystallized Alpha-Titanium", Trans. Jpn. Inst. Met. **13**, 198 (1972)
[Panda 2006]	K. B. Panda, K. S. Ravo Chandran, "Determination of elastic constants of titanium diboride (TiB_2) from first principles using FLAPW implementation of the density functional theory", Comp. Mat. Sci. **35**, 134 (2006)

[Pathak 2008]   A. Pathak, R.M. McMeeking, "Three-dimensional finite element simulations of ferroelectric polycrystals under electrical and mechanical loading", J. Mech. Phys. Sol. **56**, 663 (2008)

[Pertsev 1998]   N. A. Pertsev, "Aggregate linear properties of ferroelectric ceramics and pollycrystalline thin filmns: Calculation by the method of effectice piezoelectric medium", J. Appl. Phys. **84**, 1524 (1998)

[Pineda 2004]   E. Pineda et al., "Cell size distribution in random tesselations of space", Phys. Rev. E **70**, 066119 (2004)

[PyXL]   http://cbsu.tc.cornell.edu/staff/myers/PyXL/index.html

[PYROHL 2000]   Final report on the funded BMBF-project „Werkstoffinnovationen für integrierte Pyroarray-Memransysteme", Institut für Werkstoffwissenschaft, TU Dresden, 2000

[Raether 2006]   F. Raether, M. Iuga, "Effect of particle shape and arrangement on ther-moelastic properties of porous ceramics", J. Europ. Ceram. Soc. **26,** 2653 (2006)

[Redenbach 2009]   C. Redenbach, "Microstructure models for cellular materials", Comp. Mat. Science **44**, 1397 (2009)

[Reis 2006]   N. Reis et al., „Geometry and Topology of 3D Voronoi Partitions", J. Mater. Science Forum **514-516**, 1488 (2006)

[Rhines 1982]   F. N. Rhines, B. R. Patterson, „Effect of the degree of prior cold work on the grain volume distribution and the rate of grain growth of recrystallized alluminum", Metall. Trans. **13A**, 985 (1982)

[Rödel 2003]   J. Rödel, W. S. Kreher, „Modelling linear and nonlinear behavior of polycrystalline ferroelectric ceramics", J. Europ. Ceram. Soc. **23**, 2297 (2003)

[Romanov 1999]   A. E. Romanov et al., "Domain Patterns in (111) Oriented Tetragonal Ferroelectric Films", Phys. Stat. Sol. (a) **172**, 25 (1999)

[Qiu 1991]   Y. P. Qiu, G. J. Wenig, „Elastic constants of a polycrystal with transversely isotropic grains, and the influence of precipitates", Mech. Mater. **12** , 1 (1991)

[Saghi 1999]   G. Saghi-Szabo et al., "First-principles study of piezoelectricity in tetragonal $PbTiO_3$ and $Pb_{1/2}Ti_{1/2}O_3$ Phys. Rev. B **59**, 12773 (1999)

[Schröter 2007]   C. Schröter, "A High Throughput Method fpr the Development of Piezoelectric Lead-Free Thin Films", Dissertation, TU Dresden, 2007

[Sepliarsky 2005]	M. Sepliarsky et al., "Atomic-level simulation of ferroelectricity on oxide materials", Curr. Opin. Solid State Mater. Sci., **9**, 107 (2005)
[Shimada 2008]	T. Shimada et al., "Shell model potention for $PbTiO_3$ and its applicability to surfaces and domain walls", J. Phys. : Condens Matter **20,** 325225 (2008)
[Shirane 1951]	G. Shirane, S. Hoshino, "On the Phase Transition in Lead Titanate", Jpn. J. Phys. Soc. **6,** 265 (1951)
[Sinterdict]	http://www2.itwm.fhg.de/bv/projects/MAVO/?language=de
[Soller 2010]	T. Soller et al., „Textured and Tungsten-bronze-niobate-doped (K, Na, Li)(Nb, Ta)O_3 Piezoceramic Materials", J. Kor. Phys. Soc. **57**, 942 (2010)
[Stephens 1974]	M. A. Stephens, "EDF Statistics for goodness of Fit and Some Comparisons", J. Am. Stat. Ass. **69**, 730 (1974)
[Su 2007]	Y. Su, C. M. Landis, "Continuum thermodynamics of ferroelectric domain evolution: Theory, finite element implementation, and application to domain wall pinning", J. Mech. Phys. Solid. **55**, 280 (2007)
[Tanaka 2004]	K. Tanaka, K. Suzuki et al., "Grain Size Effect on Dielectric and Piezoelectric Properties of Alkoxy-Derived $BaTiO_3$-Based Thin Films", Jap. J. Appl. Phys. **43**, 6525 (2004)
[Ueda 1972]	I. Ueda, „Effects of Additives on Piezoelectric and Related Properties of $PbTiO_3$ Ceramics", Jap. J. Appl. Cer. **11**, 450 (1972)
[Vaz 1988]	M. Fatima Vaz, M. A. Fortes, "Grain Size Distribution: The Lognormal and The Gamma Distribution Functions", Scripta Metallurgica **22**, 35 (1988)
[Vedmedenko 2007]	O. Vedmedenko, "Ab-initio study of structural phase transformattions in Laves phases", Master thesis, University of Stuttgart, 2007
[Vedmedenko 2008]	O. Vedmedenko, F. Rösch, and C. Elsässer, "Ab-initio study of phase transformations in $NbCr_2$ and $TaCr_2$", Acta Mater. **56**, 4984 (2008)
[Völker 2010]	B. Völker, "Phase-field modeling for ferroelectrics in a multi-scale approach", Karlsruhe Institute of Technology, 2010
[Völker 2011]	B. Völker et al., „Mustiscale Modeling for ferroelectric materials: a transition from the atomic level to phase-field modeling", Cont. Mech. Therm. **23**, 435 (2011)
[Xu 2009]	T. Xu, M. Li, „Topological and statistical properties of a constrained Voronoi tesselation", Phil. Mag. **89**, 349 (2009)
[Wallace 1972]	D. C. Wallace, "Thermidynamics of Crystals", Wiley, New York, 1972

[Zalachas 2009]   N. Zalachas et al., „Effective Piezoelectric Coefficients of Ferroelectric Thin Films on Elastic Substrates", J. Intell. Mat. Syst. Struc. **20**, 683 (2009)

Acknowledgements